

DIGITALLY-ASSISTED MIXED-SIGNAL WIDEBAND COMPRESSIVE SENSING

A Dissertation

by

ZHUIZHUAN YU

Submitted to the Office of Graduate Studies of
Texas A&M University
in partial fulfillment of the requirements for the degree of

DOCTOR OF PHILOSOPHY

May 2011

Major Subject: Electrical Engineering

DIGITALLY-ASSISTED MIXED-SIGNAL WIDEBAND COMPRESSIVE SENSING

A Dissertation

by

ZHUIZHUAN YU

Submitted to the Office of Graduate Studies of
Texas A&M University
in partial fulfillment of the requirements for the degree of

DOCTOR OF PHILOSOPHY

Approved by:

Chair of Committee,	Sebastian Hoyos
Committee Members,	Scott Miller
	Henry Pfister
	Alexander Parlos
	Brian M. Sadler
Head of Department,	Costas Georgiades

May 2011

Major Subject: Electrical Engineering

ABSTRACT

Digitally-Assisted Mixed-Signal Wideband Compressive Sensing. (May 2011)

Zhuizhuan Yu, B.S.; M.S., Beijing University of Posts and Telecommunications

Chair of Advisory Committee: Dr. Sebastian Hoyos

Digitizing wideband signals requires very demanding analog-to-digital conversion (ADC) speed and resolution specifications. In this dissertation, a mixed-signal parallel compressive sensing system is proposed to realize the sensing of wideband sparse signals at sub-Nyquist rate by exploiting the signal sparsity. The mixed-signal compressive sensing is realized with a parallel segmented compressive sensing (PSCS) front-end, which not only can filter out the harmonic spurs that leak from the local random generator, but also provides a tradeoff between the sampling rate and the system complexity such that a practical hardware implementation is possible. Moreover, the signal randomization in the system is able to spread the spurious energy due to ADC nonlinearity along the signal bandwidth rather than concentrate on a few frequencies as it is the case for a conventional ADC. This important new property relaxes the ADC SFDR requirement when sensing frequency-domain sparse signals.

The mixed-signal compressive sensing system performance is greatly impacted by the accuracy of analog circuit components, especially with the scaling of CMOS technology. In this dissertation, the effect of the circuit imperfection in the mixed-signal compressive sensing system based on the PSCS front-end is investigated in detail, such as the finite settling time, the timing uncertainty and so on. An iterative background calibration algorithm

based on LMS (Least Mean Square) is proposed, which is shown to be able to effectively calibrate the error due to the circuit nonideal factors.

A low-speed prototype built with off-the-shelf components is presented. The prototype is able to sense sparse analog signals with up to 4% sparsity at 32% of the Nyquist rate. Many practical constraints that arose during building the prototype such as circuit nonidealities are addressed in detail, which provides good insights for a future high-frequency integrated circuit implementation. Based on that, a high-frequency sub-Nyquist rate receiver exploiting the parallel compressive sensing is designed and fabricated with IBM90nm CMOS technology, and measurement results are presented to show the capability of wideband compressive sensing at sub-Nyquist rate. To the best of our knowledge, this prototype is the first reported integrated chip for wideband mixed-signal compressive sensing. The proposed prototype achieves 7 bits ENOB and 3 GS/s equivalent sampling rate in simulation assuming a 0.5 ps state-of-art jitter variance, whose FOM beats the FOM of the high speed state-of-the-art Nyquist ADCs by 2-3 times.

The proposed mixed-signal compressive sensing system can be applied in various fields. In particular, its applications for wideband spectrum sensing for cognitive radios and spectrum analysis in RF tests are discussed in this work.

To my father

ACKNOWLEDGMENTS

I would like to thank all people who have been part of my doctoral studying.

First and foremost, I would like to thank Dr. Sebastian Hoyos who is the best mentor I could have wished for. His ability to look beyond limits is a true gift, and he leads as a maverick thinker. His vision, knowledge, and meticulous scholarship have indelible influence on my thinking and life beyond the time has passed and the studies have been done. It is my great honor and fortune to have been his student.

I would like to thank Dr. Brian Sadler for serving as my committee member. He is an exceptional mentor who encourages me to pursue, to persist and to achieve. His knowledge, insightfulness, patience and deep kindness is what I can always count on over the years.

I would like to express my sincere acknowledgement to my committee members, Dr. Scott Miller, Dr. Henry Pfister and Dr. Alexander Parlos, for always willing to spending their time and effort to help me out and providing me invaluable advices and guidance.

I also want to thank Dr. Jose Silvar-Martinez and Dr. Edgar Sanchez-Sinencio for their continuous support all the way. Thanks to my partners: Xi, Jinguxan, Chengliang, Jun and Mario, for their inspiring discussion and great help. Thanks to all the past and present members in the Analog and Mixed Signal Center, for their collaboration and assistance. With them, my life here has been nothing short of warmness and happiness.

Last but not least, I would like to thank my husband Chaofeng Yang for his endless love, encouragement and support. His positive thinking is the secret ingredient that helps me through the journey. My thanks also go to my family, for their always being with me.

TABLE OF CONTENTS

CHAPTER		Page
I	INTRODUCTION	1
	A. Motivation	1
	B. Research Contribution	5
	C. Dissertation Organization	6
II	BACKGROUND OF COMPRESSIVE SENSING AND RELATED WORK	8
	A. Compressed Sensing	8
	1. Sparse and Compressible Signals	8
	2. Compressive Measurements and Signal Recovery	9
	a. Compressive Measurements and Restricted Isom- etry Property	10
	b. Signal Reconstruction	11
	c. Performance Bounds on Signal Reconstruction	12
	B. Compressed Sensing of Analog Signals	14
III	MIXED-SIGNAL PARALLEL SEGMENTED COMPRESSIVE SENSING AND RECONSTRUCTION OF WIDEBAND ANA- LOG SIGNALS	19
	A. Overview	19
	B. Signal Modeling	20
	C. Mixed-signal Parallel Segmented Compressive Sensing and Reconstruction	23
	1. Mixed-signal Parallel Segmented Compressive Sens- ing Architecture	23
	2. Signal Reconstruction from Compressive Samples	25
	D. Characteristics of the Mixed-signal Parallel Segmented Com- pressive Sensing System	27
	1. Sub-Nyquist Rate Sampling and Reconstruction	27
	2. Tradeoff between the System Complexity and the Sam- pling Rate Reduction	29
	3. Flexible Spurious Frequency Rejection	33
	E. Summary	41

CHAPTER		Page
IV	ROBUSTNESS OF MIXED-SIGNAL COMPRESSIVE SENSING SYSTEM AGAINST ADC NONLINEARITY	43
	A. Impact of Randomization	44
	B. Simulations	46
	1. Simulation Setup	46
	2. Simulation Results	48
	a. Noise-free Environment	48
	b. Noisy Environment	55
	3. Performance as a Function of Sparsity Variation	55
	C. Summary	59
V	EFFECT OF CIRCUIT NONIDEALITIES AND BACKGROUND CALIBRATION	61
	A. Effect of Circuit Nonidealities	61
	B. Background Calibration of Circuit Nonidealities	66
VI	LOW-SPEED OFF-THE-SHELF COMPONENT PROTOTYPE	69
	A. System Specification	69
	B. Overall Configuration	69
	C. Multi-carrier Signal Generator	70
	D. Mixers and Integrators	71
	E. Data Collection and Signal Reconstruction	77
	F. Dealing with Circuit Nonidealities	77
	G. Testing Results	79
VII	HIGH-FREQUENCY INTEGRATED PROTOTYPE	83
	A. Overview	83
	B. Circuit Level Implementation Approach	84
	1. PSCS Front-end Circuit Architecture	84
	2. Parallel Path ADCs	86
	C. Design Specification	88
	D. Power Consumption and Area	89
	E. Figure of Merit	89
	F. Reconfigurability	92
	G. Test Results	92
VIII	APPLICATIONS ON SPECTRUM SENSING	103
	A. Cognitive Radio	103

CHAPTER	Page
B. Spectrum Analysis and Circuit Testing	108
IX CONCLUSIONS	112
REFERENCES	114
VITA	128

LIST OF TABLES

TABLE		Page
I	Relationship of the SFDR and the frequency span of two-tone test signals, where the signal has a sparsity of 2%, the third order distortion coefficient $c_3 = 0.2$	50
II	Changing of SFDR as a function of sparsity variation, where the third order distortion coefficient $c_3 = 0.01$	59
III	Testing results of the prototype	69
IV	Testing results of the prototype.	82
V	Design specifications of the CS front-end.	89
VI	Summary of the power consumption.	91
VII	Performance overview of comparable stand alone ADCs.	91
VIII	System parameters for the test.	98
IX	Summary of the test results.	98

LIST OF FIGURES

FIGURE		Page
1	Bandwidth growth trend of wireless systems.	2
2	Energy consumption of state-of-the-art ADCs.	3
3	(a) CS of digital signals (b) CS of analog signals.	15
4	Compressive sensing of analog signals based on nonuniform sampling. . .	15
5	Compressive sensing of analog signals based on random demodulation. . .	15
6	Overview of the mixed-signal PSCS (Parallel Segmented Compressive Sensing) system.	19
7	Illustration of the multi-band analog signal to the sensing radio.	21
8	Block diagram of the PSCS architecture.	24
9	Illustration of overlapping windows.	24
10	Measurement “matrix” of the PSCS architecture.	26
11	MSE of the reconstructed signal versus the normalized sampling rate for signal with different sparsity under a noise-free environment, where the input signal is a K-sparse multi-carrier signal with 128 possible subcarriers and linear programming is used for reconstruction.	30
12	The minimum normalized sampling rate for signals with different sparsity under a noise-free environment, where the input signal is a K-sparse multi-carrier signal with 128 possible subcarriers and LP is used for reconstruction.	31
13	Perfect reconstruction rate with different number of segments.	34
14	Symbol error rate with different number of segments.	35

FIGURE		Page
15	Impact of number of segments on the number of measurements required per segment.	36
16	Clock leakage into the integrators from the clock of the PN generators. . .	37
17	The location of the spurious leakage frequency relative to the filter nulls with different overlapping ratio. With $OV R = 0$, the strongest clock leakage is close to the peak of the filter's 3rd sidelobe; with $OV R = 0.1125$, the strongest clock leakage is on the 4th null of the filter.	39
18	MSE of the reconstructed signal with different overlapping ratio when there is clock leakage, where the input signal is a 18-sparse multi-carrier signal with 128 possible subcarriers and sampled by the 2-path PSCS working at 56.25% of the Nyquist rate.	40
19	Sketch of the signal spectrum at different stages of a receiver front-end in the two-tone test. (a) conventional receiver front-end. (b) compressive sensing receiver front-end.	45
20	Snapshot of the signal spectrum under noise-free environment, where the signal has a sparsity of 2%, the third order distortion coefficient $c_3 = 0.2$. From top to bottom: input two-tone test signal, the reconstructed signal using the conventional receiver where the time-domain samples undergoes the ADC nonlinear distortion, the reconstructed signal using the compressive sensing receiver where the samples of the randomized signal undergoes the ADC nonlinear distortion.	49
21	SFDR comparison between the conventional receiver and the CS receiver in the two-tone test under noise-free environment, where the signal has a sparsity of 2%, the third order distortion coefficient $c_3 = 0.2$	51
22	SFDR comparison between the conventional receiver and the CS receiver in the two-tone test versus different nonlinear distortion under noise-free environment, where the signal has a sparsity of 2%.	52
23	SDR comparison between the conventional receiver and the CS receiver in the two-tone test versus different nonlinear distortion, where the signal has a sparsity of 2%.	54

FIGURE		Page
24	Snapshot of the signal spectrum under noisy environment, where the signal has a sparsity of 2%, the third order distortion coefficient $c_3 = 0.2$. From top to bottom: input two-tone test signal, the reconstructed signal using the conventional receiver where the time-domain samples undergoes the ADC nonlinear distortion, the reconstructed signal using the compressive sensing receiver where the samples of the randomized signal undergoes the ADC nonlinear distortion.	56
25	SFDR comparison between the conventional receiver and the CS receiver in the two-tone test under noisy environment, where the signal has a sparsity of 2%, the third order distortion coefficient $c_3 = 0.2$	57
26	SFDR comparison between the conventional receiver and the CS receiver in the two-tone test versus different nonlinear distortion under noisy environment, where the signal has a sparsity of 2%.	58
27	MSE of the reconstructed signal versus the normalized sampling rate when there are no imperfections.	63
28	MSE of the reconstructed signal versus the normalized sampling rate when the random PN sequences have finite settling time.	64
29	MSE of the reconstructed signal versus the normalized sampling rate when there exists timing uncertainty on the edges of the sliding window.	65
30	Illustration of the LMS based background forward calibration.	67
31	MSE of the reconstructed signal versus the normalized sampling rate when the random PN sequences have finite settling time and the background calibration is active.	68
32	Overall configuration of the prototype using off-the-shelf components.	70
33	Macro model of one parallel path.	72
34	Circuit implementation of one parallel path.	72
35	Pin connection of the integrator in one parallel path.	73
36	Example of clock signals.	74

FIGURE		Page
37	Schematic of the integrator with overlapping.	75
38	Operation of the interleaved overlapping windowed integration and the related clocks.	76
39	Illustration of the overlapping windowing in the prototype.	76
40	Illustration of the direct training approach to deal with the circuit imperfections.	78
41	Testing setup of the prototype.	80
42	Photo of the analog and the control part of the prototype.	81
43	Example of the integrator output waveform.	81
44	Circuit implementation of the PSCS front-end.	84
45	Detailed circuitry of one complex (I-Q) path.	85
46	An example of PN sequences.	86
47	Simplified schematic of the integrator.	87
48	Frequency response of the windowed integration.	87
49	Layout of a single path of the PSCS front-end in IBM 90 nm CMOS. . . .	90
50	Evaluation board of the high-frequency PSCS front-end prototype test. . .	93
51	Diagram of the test bench.	95
52	Photo of the test bench.	96
53	Example output of the tested chip.	97
54	Illustration of the reading and resetting phase.	97
55	Spectrum of the reconstructed signal ([+50, +150, +250, +490]MHz). . .	99
56	Spectrum of the reconstructed signal ([+20, +70, +450]MHz).	99
57	Spectrum of the reconstructed signal ([+20, +70, +250, +450]MHz). . . .	100

FIGURE		Page
58	Spectrum of the reconstructed signal ([+50, +250, -490]MHz).	100
59	Spectrum of the reconstructed signal ([-20, -70, +250, +450]MHz).	101
60	Spectrum of the reconstructed signal ([+50, -150, +250, -490]MHz).	101
61	Transfer function of the pre-distortion filter in the arbitrary waveform generator the N8241A.	102
62	Time-domain signals of a simulated multi-band signal. From top to bottom, the four plots represent the transmitted signal by primary users, the received primary users' signal at the sensing radio, the reconstructed signal from the time-domain samples via the Nyquist rate ADC and the reconstructed signal from the transform-domain samples via mixed-CS at a NSR of 0.32.	106
63	Frequency-domain signals of a simulated multi-band signal. From top to bottom, the four plots represent the transmitted signal by primary users, the received primary users' signal at the sensing radio, the reconstructed signal from the time-domain samples via the Nyquist rate ADC and the reconstructed signal from the transform-domain samples via mixed-CS at a NSR of 0.32.	107
64	Normalized sampling rate (NSR) vs Δf when using the CS spectrum analyzer to do the harmonic testing.	111

CHAPTER I

INTRODUCTION

A. Motivation

In order to accommodate consumers' increasing demand on high speed wireless services, the bandwidth of wireless systems continues growing from KHz to hundreds of MHz and beyond (see Fig. 1). For example, IEEE 802.11n standard, an amendment to the IEEE 802.11-2007 release, aims to provide a maximum data rate of 540Mbps for Wireless Local Access Network (WLAN) by adding MIMO (Multiple Input Multiple Output) and 40MHz Channel Bonding to the physical layer [1]. The UWB systems under the IEEE 802.15.3a task group propose to have a data rate up to 1.32Gbps with a bandwidth of 528MHz for short-range Wireless Personal Access Network (WPAN) [2]. Although the miniaturization of CMOS technology allows increasing circuit speeds and provides excellent timing accuracy for high frequency digital circuits, the limited signal swing due to the low-voltage supply makes it difficult to obtain the required resolution in analog circuits [3]. This motivates early digitization of the analog signal, and carrying out complicated filtering and signal processing in the digital domain. Digital processing flexibility has naturally led to programmable software-defined radio (SDR) [4], as well as dynamic spectrum access and cognitive radio (CR) ideas [5]. The receiver side of these radios typically relies on digital signal processing to provide the desired sensing and processing flexibility over a wide

The journal model is *IEEE Transactions on Automatic Control*.

bandwidth, for which the ideal architecture places the analog to digital converter (ADC) right after the antenna.

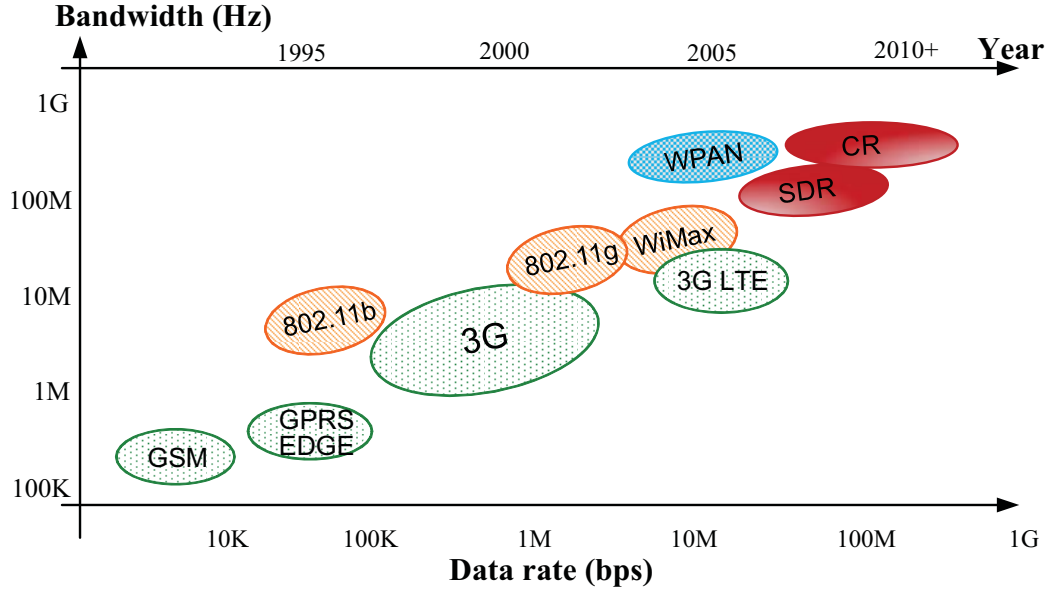


Fig. 1. Bandwidth growth trend of wireless systems.

Traditionally, the analog signal is sampled in the time-domain at Nyquist rate [6], [7]. The increasing demand for systems with both higher bandwidth and lower power consumption motivates the search of innovative ADCs, for example, the time-interleaving structure [8–12] and the multi-channel filter-bank approach [13–20]. However, with sensing and communication bandwidths expanding from hundreds of MHz to several GHz, the ADC power consumption can become very large, especially given the sensing goal to detect signals over a large dynamic range. Fig. 2 summarizes the energy consumption of state-of-the-art ADCs working at Nyquist rate [21], from which we can see that the energy consumption per conversion of most state-of-the-art ADCs is above 100 fJ. Based on that,

we can do a quick calculation. Suppose a receiver should detect a weak signal of $1\mu V$ in the presence of a $100mV$ interferer. These observed signal levels are not uncommon in a typical fading wireless environment, and result in the need for 16-bit ADC resolution. Achieving this over a large bandwidth of 5GHz say, the required power consumption of this ADC would be 100W with the rather optimistic assumption on the energy consumption at 100 fJ per conversion [21], [22], [23].

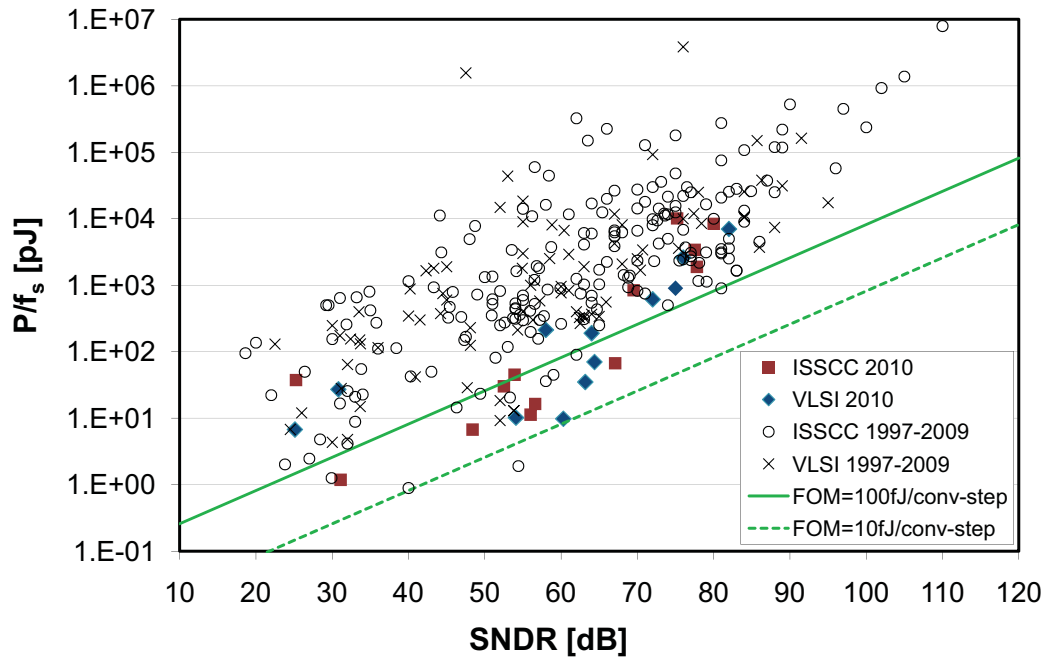


Fig. 2. Energy consumption of state-of-the-art ADCs.

Fortunately, in some practical cases, there may be unoccupied regions in some transform-domain of the signal (i.e., the signal is sparse in some domain and therefore compressible at the receiver front-end). For example, if we take several snapshots of the impulse radio UWB signal using an oscilloscope, we may find that active UWB pulses exist only

for a small piece of time in each snapshot. In other words, the UWB signal shows some sparsity in the time domain [24], [25], [26]. Studies done by the FCC's Spectrum Policy Task Force [27] reported that the temporal and geographic utilization of allocated spectrum varies from 15% – 85% in most major US metropolitan areas [27]. In other words, the current frequency usage shows some sparsity in both frequency domain and space domain. (In fact, it is just this sparsity in frequency usage that leads to the concept of dynamic spectrum sharing, which is one of the main functions of CRs.) In addition, images are sparse in the wavelet-domain [28]. The sparsity means that the inherent information rate of those signals is actually less than the rate defined by the signal bandwidth, and makes them compressible.

For *sparse* signals, the definition of which is given in Chapter II, recent work in Compressed Sensing (CS) [29–31] provides a new framework to process them efficiently. According to CS theories, the characteristics of *sparse* signals can be completely captured by a number of projections over a random basis and reconstructed perfectly from these random projections. The number of random projections is on the order of the signal's information rate rather than the Nyquist rate. When this research was first started in 2007, most work in the field of CS was in the digital domain, where full-rate sampling is generally required and the issue is then to reduce the complexity of subsequent signal processing. Several questions naturally came to the author's mind and they are: (i) The random projections (measurements) in CS are done over a discrete-time signal that is obtained by sampling the continuous-time signal at Nyquist rate, which is paradoxical because sub-Nyquist sensing is achieved by first discretizing the analog signal at Nyquist rate. Can we avoid the dis-

cretization at Nyquist rate by applying CS to the analog signal directly? (ii) How are the random measurements implemented in practice? Are they practically affordable? (iii) How will the practical imperfections impact the performance and how do we analyze and address those imperfections? (iv) What might be interesting applications of this idea? Trying to answer these questions finally brings the work presented in this dissertation.

B. Research Contribution

The objective of this research is to propose a scheme to realize the mixed-signal compressive sensing of wideband sparse signals at sub-Nyquist rate and build prototypes for it, and the principle guiding this research conducted in this paper is the feasibility of implementation. The highlights of this research are summarized as follows:

1. A mixed-signal compressive sensing architecture based on Parallel Segmented Compressive Sensing (PSCS) is proposed, where the CS is applied to analog signals directly and the input sparse signal is sensed at sub-Nyquist rate.
2. The tradeoff between the hardware complexity and the sampling rate of the proposed PSCS architecture is exploited.
3. A flexible spurious frequency rejection scheme is proposed.
4. The robustness against ADC nonlinearity of mixed-signal compressive sensing architectures is analyzed and compared with conventional Nyquist rate sampling architectures.

5. The effect of circuit imperfections in the PSCS architecture is addressed and background calibration schemes are proposed to compensate for the circuit nonidealities.
6. A low-frequency off-the-shelf component prototype of the PSCS architecture is built.
7. A high-frequency integrated prototype of the PSCS architecture using IBM 90nm technology is built.¹

C. Dissertation Organization

The remainder of this dissertation is organized as follows:

Chapter II provides the background of compressive sensing and summarizes the related work.

Chapter III introduces the proposed PSCS architecture, including the signal modeling, random projection and signal reconstruction, and discusses the characteristics of the proposed PSCS architecture.

Chapter IV investigates the robustness of mixed-signal compressive sensing architecture against ADC nonlinearity in comparison with conventional Nyquist rate sampling architectures when sampling frequency-domain sparse signals.

Chapter V addresses the effect of circuit nonidealities in the PSCS architecture and shows how the background calibration compensates for the circuit imperfections.

Chapter VI introduces the low-frequency prototype of the PSCS architecture built using off-the-shelf components.

¹Joint work with Xi Chen.

Chapter VII introduces the high-frequency integrated prototype of the PSCS architecture implemented with the IBM 90nm CMOS technology, with a system level view.

Chapter VIII gives application examples of the proposed PSCS architecture on the spectrum sensing for cognitive radios and the usage on spectrum analyzer.

Chapter IX summarizes this research.

CHAPTER II

BACKGROUND OF COMPRESSIVE SENSING AND RELATED WORK

A. Compressed Sensing

In 1949, Shannon published his famous paper "Communication in the presence of noise" [6], which set the foundation of information theory. At the beginning of his paper, he presented the sampling theory which has been guiding the signal sampling and reconstruction for over 50 years. According to Shannon's sampling theory, the sampling rate for perfect signal reconstruction needs to be at least twice the signal's highest frequency. Compressive Sensing (CS), starting with the work of [29], [30], provides a novel approach for signal sampling and reconstruction, which states that perfect signal reconstruction from incomplete measurements is possible for certain types of signals, called *sparse* signals or *compressive* signals.

1. Sparse and Compressible Signals

Sparse signals or *compressive* signals can be well-approximated by a sparse expansion over some basis, that is, by only a small number of non-zero coefficients. Mathematically speaking, a vector $\mathbf{x} \in \mathbb{C}^S$ is K -sparse over some basis Ψ , if it can be written as $\mathbf{x} = \Psi \mathbf{a}$ and the support size of $\mathbf{a} = [a_1, a_2, \dots, a_S]^T$ is equal to K with $K \ll S$. Where, the support of \mathbf{a} is denoted as

$$\text{supp}(\mathbf{a}) = \{j : a_j \neq 0\}, \quad (2.1)$$

and the support size of \mathbf{a} is defined as

$$\|\mathbf{a}\|_0 = |\text{supp}(\mathbf{a})|, \quad (2.2)$$

where, $\|\cdot\|_0$ is the l_0 -norm which counts the non-zero items. Furthermore, a vector \mathbf{a} is called *compressible* if the l_p approximation error $\sigma_k(\mathbf{a})_p$ by its best K -term approximation \mathbf{a}_K decays exponentially as K increases, where

$$\sigma_k(\mathbf{a})_p = \arg \min_{\bar{\mathbf{a}} \in \Sigma_k} \|\mathbf{a} - \bar{\mathbf{a}}\|_p = \|\mathbf{a} - \mathbf{a}_K\|_p, \quad (2.3)$$

and the l_p norm of the vector \mathbf{a} is defined as $\|\mathbf{a}\|_p = \left(\sum_{i=1}^S |a_i|^p \right)^{1/p}$ for $0 < p < \infty$.

2. Compressive Measurements and Signal Recovery

With traditional sampling techniques, *sparse* signals are acquired at full Nyquist rate at first, and afterwards only the useful information is kept at the compression stage. Instead, compressive sensing aims at obtaining those non-zero coefficients (large coefficients for *compressible* signals) more directly by taking only a small number of *linear* and *nonadaptive* measurements of the signal. Without having a prior knowledge of the location of those non-zero (large) coefficients, how can the original signal be isolated from the infinitely many solutions of the undetermined linear system? Under the framework of compressive sensing, perfect signal reconstruction from incomplete measurements is achieved by using specially designed measurements and locating the sparsest solution out of the multiple solutions which satisfy the constraints.

a. Compressive Measurements and Restricted Isometry Property

The *measurement* is done by projecting \mathbf{x} over another random basis Φ that is incoherent with Ψ , i.e.,

$$\mathbf{y} = \Phi\Psi\mathbf{a}, \quad (2.4)$$

where, Φ is called the *measurement matrix* and $\mathbf{V} = \Phi\Psi$ is called the *reconstruction matrix* in this dissertation. For robust signal recovery, it is essential that the *measurement matrix* satisfies the Restricted Isometry Property (RIP) [29], [30], [32].

Definition The restricted isometry constant δ_k of a matrix $\Phi \in \mathbb{C}^{L \times S}$ is the smallest number such that

$$(1 - \delta_k)\|\mathbf{z}\|_2^2 \leq \|\Phi\mathbf{z}\|_2^2 \leq (1 + \delta_k)\|\mathbf{z}\|_2^2 \quad (2.5)$$

for all $\mathbf{z} \in \Sigma_k$, where $\Sigma_k := \{\mathbf{a} \in \mathbb{C}^S : \|\mathbf{a}\|_0 \leq k\}$.

The matrix Φ is said to satisfy the *restricted isometry property* of order k (alternatively speaking, k -RIP) with constant δ_k if $\delta_k \in (0, 1)$, which means *all* column submatrix of Φ with at most k columns are required to be well-conditioned. While the design of a measurement matrix Φ satisfy the k -RIP is an NP-Complete problem in general [31], a large number of random matrices have the k -RIP with high probability. For example, the random matrices whose entries are i.i.d. Gaussian, Bernoulli (± 1), or more generally subGaussian² satisfy the k -RIP with high probability provided $L = O(K \log(S/K))$. These random

²A random variable X is called subGaussian if there exists $c > 0$ such that $\mathbb{E}^{Xt} \leq e^{c^2 t^2 / 2}$ for all $t \in \mathbb{R}$. Examples include the Gaussian and Bernoulli random variables, as well as any bounded random variable [33].

matrices also have a so-called universality property in that, for any choice of orthonormal basis matrix Ψ , $\mathbf{V} = \Phi\Psi$ also has the k-RIP with high probability.

b. Signal Reconstruction

To recover the original K -sparse signal from L incomplete measurements, a natural approach is to find the sparsest solution from the infinitely many solutions that satisfy the constraints $\mathbf{y} = \mathbf{V}\mathbf{a}$. Mathematically, this is to resolve the following l_0 optimization problem,

$$\hat{\mathbf{a}} = \arg \min \|\mathbf{a}\|_0 \quad s.t. \mathbf{y} = \Phi\Psi\mathbf{a} \quad (2.6)$$

Although this optimization can recover a K -sparse signal from just $L = 2K$ compressive measurements, unfortunately, it is a combinatorial, NP-Complete problem and computationally intractable [34], [35]. Moreover, the recovery is not stable in the presence of noise [36].

In practice, there are two categories of computationally tractable approaches to reconstruct the K -sparse signal from L incomplete measurements. The first approach is to resolve the following l_1 optimization through convex relaxation.

- noiseless case

$$\hat{\mathbf{a}} = \arg \min \|\mathbf{a}\|_1 \quad s.t. \mathbf{y} = \mathbf{V}\mathbf{a}, \quad (2.7)$$

- noisy case

$$\hat{\mathbf{a}} = \arg \min \|\mathbf{a}\|_1 \quad s.t. \|\mathbf{y} - \mathbf{V}\mathbf{a}\|_2 \leq \epsilon_n, \quad (2.8)$$

where ϵ_n is the error due to the noise.

There are many mature algorithms to resolve the above convex optimization problems in polynomial time [37]. Variations include basis pursuit with denoising [38], complexity based regularization [39], the Dantzig Selector [40] and so on.

The second approach is to find the solution iteratively using greedy algorithms, examples of which include the matching pursuit, orthogonal matching pursuit [41], StOMP [42], iterative hard thresholding (IHT) [43], CoSaMP [44], normalized IHT [45], Subspace Pursuit (SP) [46] and among others.

c. Performance Bounds on Signal Reconstruction

The performance bounds for the reconstructed signals are closely related to the following two theorems [47]. Variations of the theorems are presented in many other publications, including [29].

Theorem II.1 [47] *Assume $\mathbf{V} \in \mathbb{C}^{L \times S}$ satisfies the RIP of order $3k$ with $\delta_{3k} < 1/3$. For $\mathbf{a} \in \mathbb{C}^S$, let $\mathbf{y} = \mathbf{V}\mathbf{a}$ and \mathbf{a}^* be the solution of the l_1 optimization problem (2.7). Then,*

$$\|\mathbf{x} - \mathbf{x}^*\|_2 \leq C \frac{\sigma_k(\mathbf{a})_1}{\sqrt{k}}$$

$$\text{with } C = \frac{2}{1-\gamma} \left(\frac{\gamma+1}{\sqrt{2}} + \gamma \right), \gamma = \sqrt{\frac{1+\delta_{3k}}{2(1-\delta_{3k})}}$$

Theorem II.2 [47] *Assume that the restricted isometry constant δ_{2k} of the matrix $\mathbf{V} \in \mathbb{C}^{L \times S}$ satisfies*

$$\delta_{2k} \leq \frac{2}{3 + \sqrt{7/4}} \approx 0.4627$$

For $\mathbf{a} \in \mathbb{C}^S$, let $\mathbf{y} = \mathbf{V}\mathbf{a} + \epsilon_n$ and \mathbf{a}^ be the solution of the l_1 optimization problem (2.8).*

Then,

$$\|\mathbf{x} - \mathbf{x}^*\|_2 \leq C_1 \epsilon_n + C_2 \frac{\sigma_k(\mathbf{a})_1}{\sqrt{(k)}}$$

for some constants C_1, C_2 that depends on δ_{2k} .

Based on the above theorems, we have the following performance bounds on the reconstructed signals [36].

- For a noise-free K -sparse signals \mathbf{a} , the signal can be exactly recovered from the compressive measurements $\mathbf{y} = \mathbf{V}\mathbf{a}$.
- For a K -sparse signal that is corrupted by noise \mathbf{n} with a bounded norm of ϵ_n , that is, $\mathbf{y} = \mathbf{V}\mathbf{a} + \mathbf{n}$, the Mean Square Error (MSE) of the reconstructed signal is bounded by

$$\|\mathbf{a} - \hat{\mathbf{a}}\|_2 \leq C\epsilon_n \quad (2.9)$$

with C a small constant [29], [43], [44], [48].

- For a *compressible* signal that is corrupted by noise \mathbf{n} with a bounded norm of ϵ_n , that is, $\mathbf{y} = \mathbf{V}\mathbf{a} + \mathbf{n}$, the Mean Square Error (MSE) of the reconstructed signal is bounded by

$$\|\mathbf{a} - \hat{\mathbf{a}}\|_2 \leq C_1 \|\mathbf{a} - \mathbf{a}_K\|_2 + C_2 \frac{1}{\sqrt{K}} \|\mathbf{a} - \mathbf{a}_K\|_1 + C_3 \epsilon_n \quad (2.10)$$

with C_1, C_2 and C_3 some constants.

B. Compressed Sensing of Analog Signals

CS provides a novel framework to process *sparse* and *compressible* signals. However, the majority of the CS literature focus on the compressive measurement in the digital domain. Alternatively speaking, they studied the problem of sparse signal recovery in an undetermined linear system, where the sparse signals are sampled at Nyquist rate at first, and then CS is applied to obtain the large coefficients of the signal expansion over some basis, see Fig. 3 (a). Compared with conventional Nyquist sampling systems where all coefficients are acquired after the signals are sampled at Nyquist rate and only large coefficients are kept at the compression stage, the utilization of CS in digital domain is able to save the effort spent on acquiring those small coefficients that will be thrown away during the compression stage. However, it still necessitates the Nyquist rate Analog-to-Digital Conversion (ADC) which is in fact the bottleneck for the sensing of (ultra-)wideband signals today, as mentioned in Chapter I. This is somewhat paradoxical because the sub-Nyquist sensing is achieved by first discretizing the analog signal at Nyquist rate and then applying CS. Naturally, researchers look for approaches to avoid the high-speed ADCs by applying CS to the analog signal directly, as shown in Fig. 3 (b).

In [49], [50], an approach of compressive sensing of analog signals through nonuniform sampling was proposed. Basically, the input wideband *sparse* signal is sampled at a nonuniform rate, and the average sampling rate is below the Nyquist rate, as shown in Fig. 4. However, this approach has two main drawbacks. First, it is difficult to maintain the accuracy of the random timing shift while sampling in high-speed systems [51]. Second, the sampling clock still needs to run at Nyquist rate, since the minimum spacing between

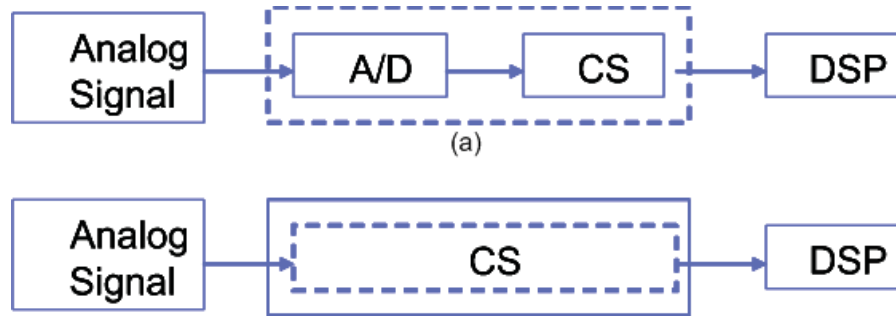


Fig. 3. (a) CS of digital signals (b) CS of analog signals.



Fig. 4. Compressive sensing of analog signals based on nonuniform sampling.

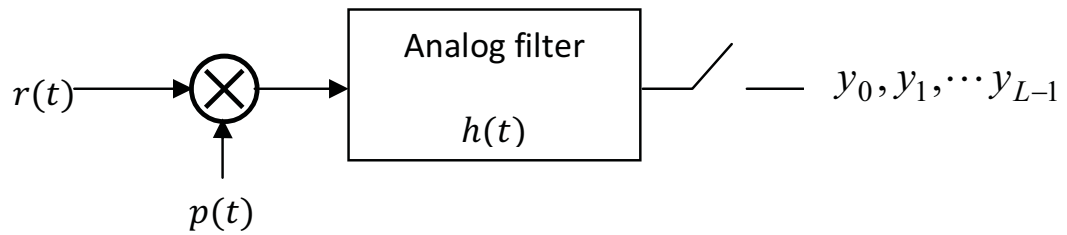


Fig. 5. Compressive sensing of analog signals based on random demodulation.

two consecutive samples needs to be the Nyquist period, as required for the CS signal reconstruction. Although using time-interleaved ADCs can relax the conversion rate of the ADCs, all ADCs still share the same analog front-end which must tolerate the whole input signal bandwidth. Multicoset sampling is a special case of interleaved ADCs, so that the same limitations apply [52], [53]. The algorithm proposed in [54] can be used to recover the signal from spectrum-blind nonuniform sampling, however, it requires interpolating the samples to full Nyquist rate before reconstruction, which is also difficult in high-speed systems. Other related work on the nonuniform sampling include [55] and [56]. Considering the difficulty in implementing the accurate time shifts and the ideal samplers in wideband systems, the nonuniform sampling approach is more appropriate for intermediate frequency regime.

Another approach of compressive sensing for analog signals is based on random demodulation, which was first described in [57] and [58]. In this approach, the analog signal is first demodulated with a pseudo-random chipping sequence $p(t)$, then passed through an analog filter $h(t)$, and the measurements are obtained in *serial* by sampling the filtered signal at sub-Nyquist rate, which is shown in Fig. 5. The serial sampling structure is appropriate for real-time processing. However, the sampling rate may still be high for wideband applications. In addition, the architecture lacks the flexibility in addressing some practical constraints, such as spurious frequency rejection. In [59], we proposed a *Parallel Segmented Compressed Sensing (PSCS)* structure to sense the analog signal at sub-Nyquist rate. This architecture provides a design tradeoff between the system complexity and the sampling rate, and also a flexible scheme for spurious frequency rejection. This architec-

ture is one of the main contributions of this research and will be explained in more details in the rest of this dissection.

The modulated wideband converter (MWC) proposed in [60] and [61] is also a method of compressive sensing of analog signals. The MWC consists of an analog front-end with multiple parallel channels. At each channel, the input signal is multiplied by a periodic waveform $p_i(t)$, lowpass filtered and then sampled. In the MWC, the key is the periodicity of the waveforms $p_i(t)$, because the periodicity in the time domain implies the existence of harmonic frequencies in the frequency domain, which can be deliberately utilized to shift various frequency regions to baseband simultaneously. After being filtered, the resulting baseband signal can be sampled at sub-Nyquist rate. The most challenge for the MWC is that the number of parallel channels is usually too many to be affordable in terms of practical implementation. In the example in [61], the number of channels is 35 which is barely possible in practice. Moreover, the generation of those periodic waveforms is also a big challenge in the MWC. In [60], an MWC system with $p_i(t)$ consisting of different sign alternations was analyzed and simulated. In [61], a theoretical framework for the required properties of the sensing matrix in sub-Nyquist systems was proposed. An interesting observation is the connection of the MWC to the idea of ultra-wideband analog to digital conversion via signal expansion presented in the work of [62] and [63], where the wideband signal is also sent to an analog front-end with multiple parallel channels, and at each channel the signal is mixed with some basis functions, for example, the sinusoidal functions which are square waveforms in practice, so that the whole signal bandwidth is channelized and shifted to baseband. Since the signal considered in [62] and [63] is not

limited to *sparse* signals, general Least Square or Minimum Mean Square Error (MMSE) rules were used for signal reconstruction.

Besides the above approaches for compressive sampling of analog signals, there are some other approaches to achieve sub-Nyquist sampling of analog signals, for example, the Nyquist-folding system in [64] and the early work on the nonuniform sampling with known carrier frequencies in [65], [66]. Since they do not incorporate CS ideas such as sparse representations, they will not be discussed here.

CHAPTER III

MIXED-SIGNAL PARALLEL SEGMENTED COMPRESSIVE SENSING AND RECONSTRUCTION OF WIDEBAND ANALOG SIGNALS

A. Overview



Fig. 6. Overview of the mixed-signal PSCS (Parallel Segmented Compressive Sensing) system.

Fig. 6 gives an overview of the system where the mixed-signal parallel segmented compressive sensing (PSCS) is applied to sense wideband analog signals at sub-Nyquist rate. Since the sub-Nyquist rate sampling and signal reconstruction is under the framework of CS, the input signal of interest in this dissertation must be *sparse* or *compressible*. For simplicity, *sparse* signals are used in general to refer to both *sparse* signals and *compressible* signals in this dissertation unless stated explicitly. In the system shown in Fig. 6, the input *sparse* signal is sampled at sub-Nyquist rate by the PSCS architecture, and then converted to digital samples by low-rate ADCs, from which the original signal can be recovered. Depending on the specific application needs, further baseband digital signal processing may be necessary, which may occur after or during the procedure of signal reconstruction.

B. Signal Modeling

When extending the CS formulation in digital domain to analog signals, the first difficulty encountered is in the signal model, because the sparsity defined in CS is the number of nonzero elements in the vector \mathbf{x} , while the sparsity of analog signal involves an uncountable number of zeros and nonzeros. In this dissertation, a signal model based on *finite dimensional* approximation is used.

For example, assume that the input sparse signal $r(t)$ to the mixed-signal PSCS system is a multi-band analog signal with a frequency span from f_l to f_h , whose spectrum is illustrated in Fig. 7. Specifically, the frequency spectrum of $r(t)$ consists of W disjoint subbands, each of which has a bandwidth of B_i ($i = 1, 2, \dots, W$); there exist $W - 1$ frequency gaps associated with these W subbands and these frequency gaps are always unoccupied; each subband consists of a certain number of channels, and only some of these channels are occupied at any time. In Fig. 7, each line with an upward arrow represents a channel, the lines in red are always inactive, since they are in the range of unoccupied frequency gaps; the solid lines in black stand for the currently active channels, the dashed lines in black stand for the currently inactive channels, and the active status of those lines in black varies with time.

Without loss of generality, we assume that $r(t)$ is bandlimited to $[0, f_h]$, so $r(t)$ can be written as

$$r(t) = \int_{-\infty}^{\infty} R(f) e^{j2\pi ft} df = \int_0^{f_h} R(f) e^{j2\pi ft} df, \quad (3.1)$$

where, $R(f)$ is the Fourier transform of $r(t)$. Note that $r(t)$ is a continuous-time analog

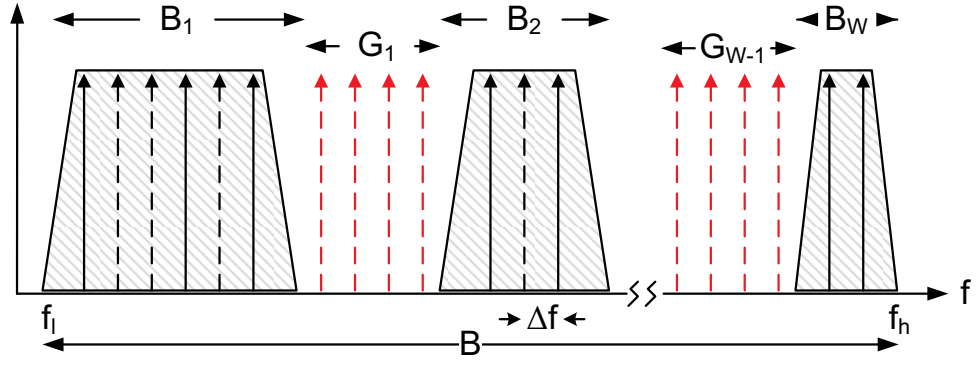


Fig. 7. Illustration of the multi-band analog signal to the sensing radio.

signal, which is essentially infinite-dimensional according to traditional sampling theory. In [67], [68] the authors show that with a set of operations grouped under a block named continuous-to-finite (CTF), the continuous nature of the problem can be transformed to a finite dimensional equivalent, and the resulting problem fits the framework of compressive sensing which has focused on sensing of finite-dimensional vectors. Moreover, in many application scenarios, it is not necessary to capture the continuous spectrum of the signal. For example, in the application of spectrum sensing for cognitive radios [69], [70], [71], [72], [73], the multi-band model shown in Fig. 7 can be used to model the frequency usage status, where the W subbands may represent W disjoint frequency bands complying with different wireless standards and each subband consists of multiple channels that can be allocated to users. Since the purpose in this application is to *detect* those *spectrum holes* that are unoccupied by primary users, the resolution grid of spectrum estimation can be not that fine. Therefore, it is possible and sufficient, at least for some applications, for us to approximate the continuous-time analog signal $r(t)$ with a model of finite dimension as

follows.

$$r(t) \approx \sum_{s=0}^{S-1} R(s\Delta f) e^{j2\pi s\Delta f t} \Delta f, \quad t \in [0, T_s] \quad (3.2)$$

where $\Delta f = 1/T_s$ is the resolution on the frequency axis and $(S-1)\Delta f = f_h$. In other words, $r(t)$ is approximated as a finite dimensional multi-carrier signal bandlimited to $[0, f_h]$ and with a carrier spacing of Δf . The frequency resolution grid Δf can always be tuned according to specific application requirements. The sparse frequency occupancy means that statistically speaking, only K out of the S carriers are active at any time, where $K \ll S$. The multi-carrier model is convenient for representing user occupancy with spectral sparsity. Comparing equation (3.1) and equation (3.2), we notice that this model is based on a finite dimensional approximation of the signal spectrum. Since there are S unknowns where $R(s\Delta f)$ in equation (3.2) and $R(s\Delta f)$ change every T_s seconds, the model in equation (3.2) is a case of a Finite Rate of Innovation (FRI) model in which the innovation locations lie on the Nyquist grid [74]. For clarity, we rewrite equation (3.2) as:

$$r(t) = \sum_{s=0}^{S-1} a_s \Psi_s(t) + n(t), \quad (3.3)$$

where $n(t)$ is additive white Gaussian noise (AWGN), $\Psi = [\Psi_0(t), \Psi_1(t), \dots, \Psi_{S-1}(t)]$, $\Psi_s(t) = e^{j2\pi s\Delta f t}$, $\mathbf{a} = [a_0(t), a_1(t), \dots, a_{S-1}(t)] \in \mathbb{C}^S$, $a_s = \Delta f R(s\Delta f)$ and \mathbf{a} has only $K \ll S$ non-zero elements. Since Δf is a scalar, for simplicity, we discard it in the rest of the dissertation. The spectrum sensing and reconstruction of wideband analog signals are usually based on the observed signal spectrum $R(s\Delta f)$, or equivalently, the estimation of the coefficients a_s .

C. Mixed-signal Parallel Segmented Compressive Sensing and Reconstruction

In the system shown in Fig. 6, the input *sparse* signal is sampled at sub-Nyquist rate by the PSCS architecture, and then converted to digital samples by low-rate ADCs, from which the original signal can be recovered and sent for further processing.

1. Mixed-signal Parallel Segmented Compressive Sensing Architecture

The Parallel Segmented Compressive Sensing (PSCS) architecture is shown in Fig. 8, which we first proposed in [59]. In the PSCS architecture, the input signal $r(t)$ for $t \in (0, T_s]$, which is the K -sparse signal as given in equation (3.3), is sent to N parallel paths. Measurements of $r(t)$ are obtained in *parallel* by calculating the inner product of the segments of the received signal $r(t)$ and the random basis functions during a period of T . Specifically, at the n_{th} path, $r(t)$ is mixed with a random basis function $\Phi_n(t)$. The output of the mixer is then sent to a sliding window with a width of T_c and integrated. Two adjacent windows have an overlapping time $T_c - T_m$, which defines an overlapping percentage $OV R = \frac{T_c - T_m}{T_c}$, as shown in Fig. 9. The output of the integrators are sampled and M samples are collected at each path. The m^{th} sample of the n^{th} branch is given by

$$y_{mN+n} = \int_{mT_m}^{mT_m+T_c} r(t) \Phi_n^*(t) dt. \quad (3.4)$$

where, $\Phi_{mN+n}(t)$ is chosen randomly for all m and n . At the end of each integration time T_c , the outputs of the integrators are fed to a set of ADCs and the quantized digital words are sent to the DSP blocks for further processing. There are a total of $L = MN$ samples

collected every T_s seconds and these samples are organized into a vector as follows.

$$\mathbf{y} = [\tilde{\mathbf{y}}_0^T, \tilde{\mathbf{y}}_1^T, \dots, \tilde{\mathbf{y}}_{M-1}^T]^T, \quad (3.5)$$

where, $\tilde{\mathbf{y}}_{\mathbf{m}} = [y_{mN}, y_{mN+1}, \dots, y_{mN+N-1}]^T$ is the vector consisting of the m^{th} samples from all N branches.

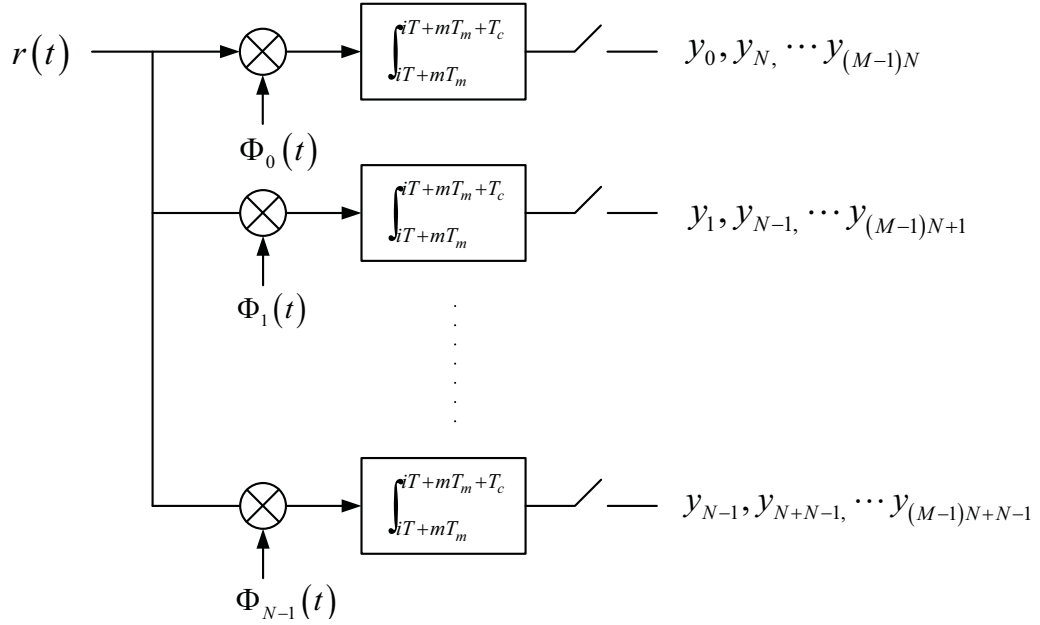


Fig. 8. Block diagram of the PSCS architecture.

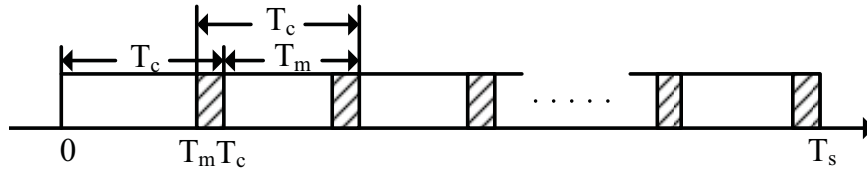


Fig. 9. Illustration of overlapping windows.

The windowed integrator with overlapping acts as a spurious frequency rejection

mechanism in the PSCS architecture, which will be discussed in Section D.3. For the random basis $\Phi_l(t)$ there are several choices, such as Gaussian, Bernoulli and so on, as mentioned in Chapter II. Here, the Bernoulli random basis has particular merit because the desired binary waveforms can be generated with digital sequential circuits.

Recall that in the formulation of CS in digital domain, the random measurements $\mathbf{y}_{L \times 1}$ is obtained by multiplying the input signal vector $\mathbf{x}_{S \times 1}$ with the random projection matrix Φ , i.e., $\mathbf{y} = \Phi \mathbf{x}$, where Φ has a size of $L \times S$. Here, we can introduce a similar random projection “matrix” to help understand the PSCS architecture, which is shown in Fig. 10, where each shadowed box corresponds to one piece of the random basis functions. The reason why “matrix” is quoted is because this “matrix” has a size of $L \times \infty$ and the infinity dimension is due to the fact that the input signal to the mixer is the analog signal and there are ∞ samples during the processing period T . This is also the reason why the architecture is called mixed-signal since the CS block has analog input and digital output. Note that the “matrix” is a stack of N block-diagonal sub-matrices with a size of $M \times \infty$, each of which corresponds to the output M samples of one path. The diagonal structure is due to the segmentation. The overlapping of the shadowed pieces of two adjacent rows reflects the overlapping of the sliding window.

2. Signal Reconstruction from Compressive Samples

Recall that the CS signal reconstruction from the compressive samples is to resolve the optimization problem given in equation (2.8). For convenience, it is repeated below,

$$\hat{\mathbf{a}} = \arg \min \|\mathbf{a}\|_1 \quad s.t. \quad \|\mathbf{y} - \Phi \Psi \mathbf{a}\|_2 \leq \epsilon_n,$$

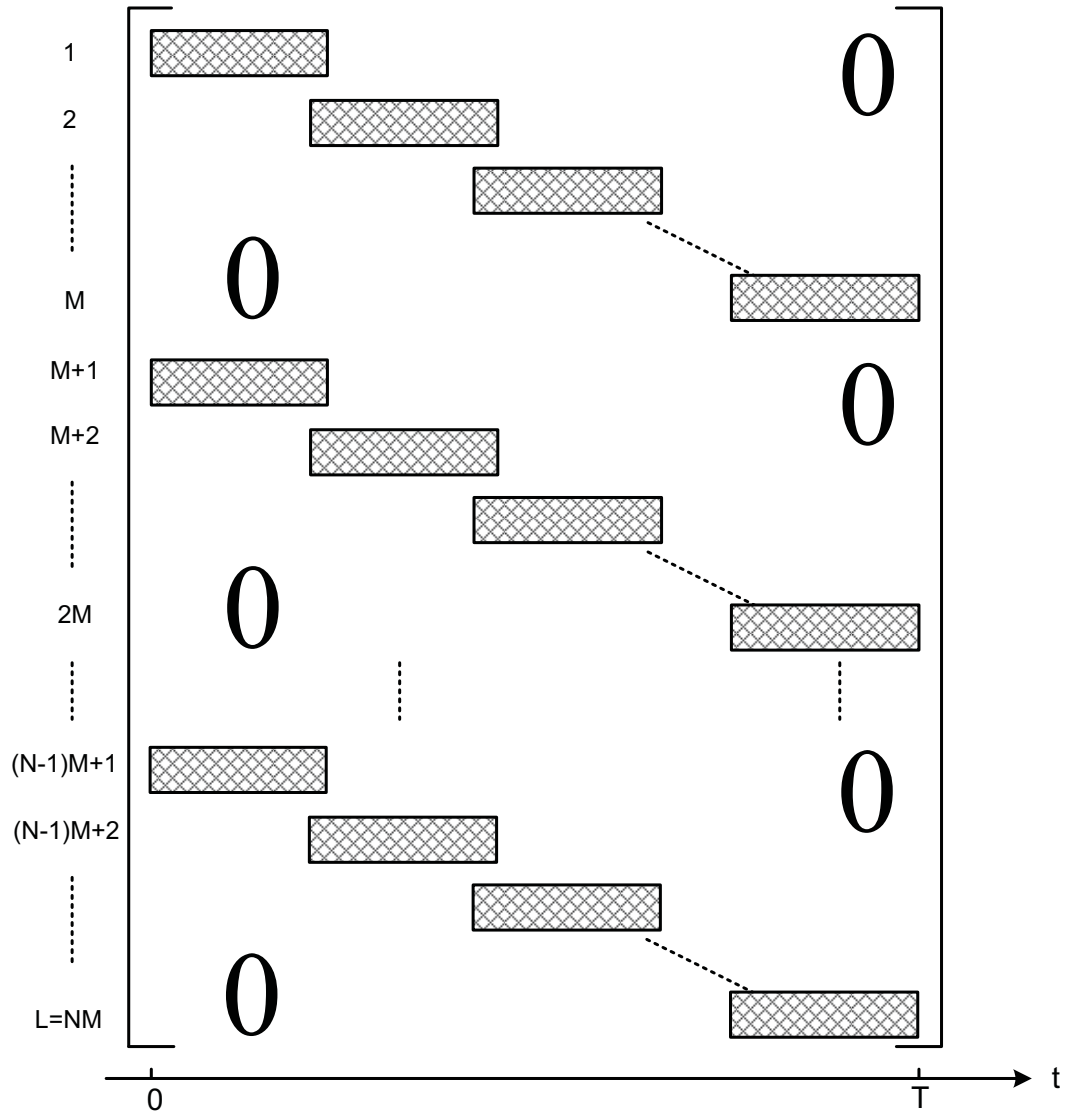


Fig. 10. Measurement "matrix" of the PSCS architecture.

where ϵ_n is the error due to the noise.

The first step for signal recovery is to calculate the *reconstruction matrix* $\mathbf{V} = \Phi\Psi = \{v_{i,j}\}_{L \times S}$, which can be done in a similar way as obtaining the measurements. Specifically, the element at the $mN + n$ row and the s column is given by:

$$V_{mN+n,s} = \int_{mT_m}^{mT_m+T_c} \Psi_s(t) \Phi_n^*(t) dt. \quad (3.6)$$

Once we get \mathbf{V} , we can estimate \mathbf{a} by solving the problem in (2.8) and reconstruct the original signal using $\mathbf{r} = \Psi\hat{\mathbf{a}}$.

As mentioned in Chapter II, there are abundant algorithms available to resolve the above convex optimization problems. These algorithms vary in terms of the computational complexity, the minimum number of measurements required for signal recovery and robustness to noise. Below is a pseudo code of the Orthogonal Matching Pursuit (OMP) algorithm, which is one type of greedy algorithm.

D. Characteristics of the Mixed-signal Parallel Segmented Compressive Sensing System

1. Sub-Nyquist Rate Sampling and Reconstruction

A series of simulations are done to show the PSCS architecture's capability of sensing and reconstructing analog sparse signals at sub-Nyquist rate. In the simulations, the input signal is a frequency-domain K -sparse multi-carrier signal with a finite dimension of $S = 128$, as modeled in Equation (3.3), and the signal sparsity is denoted as K/S . The subcarrier spacing $\Delta f = 1\text{GHz}/128 = 7.8125\text{MHz}$ and the symbol duration time $T_s = 1/\Delta f = 128\text{ns}$. The locations of the K active subcarriers are chosen randomly and

Algorithm 1 Orthogonal Matching Pursuit (OMP)

- 1: initialization: $\mathbf{z}_0 = \mathbf{y}$;
 - 2: **for** $k = 1 : K$ **do**
 - 3: Calculate the projection of the residue \mathbf{z}_{k-1} over the direction of \mathbf{V}_j for all j

$$b_{k,j} = \langle \mathbf{z}_{k-1}, \mathbf{V}_j \rangle,$$

where, \mathbf{V}_j is the j_{th} column of \mathbf{V} ;
 - 4: Find the column \mathbf{V}_{i_k} such that
$$i_k = \arg \max_{j \in 1, 2, \dots, S} b_{k,j};$$
 - 5: Compute the new residue \mathbf{z}_k

$$\hat{a}_k = \frac{\langle \mathbf{y}, \mathbf{V}_{i_k} \rangle}{\langle \mathbf{V}_{i_k}, \mathbf{V}_{i_k} \rangle}$$

$$\mathbf{z}_k = \mathbf{z}_{k-1} - \hat{a}_k \mathbf{V}_{i_k};$$
 - 6: **end for**
 - 7: Output the reconstructed signal: $\hat{x}(t) = \sum_{k=1}^K \hat{a}_k \Psi_{i_k}(t)$;
-

changed every T_s seconds. For simplicity, the channel is assumed to be noise-free.

Fig. 11 gives the normalized MSE (Mean Square Error) of the reconstructed signal versus the NSR (Normalized Sampling Rate) for signals with different sparsity, where the signal sparsity is measured by K/S , MSE is equal to $\frac{\|\mathbf{a} - \hat{\mathbf{a}}\|_2}{\|\mathbf{a}\|_2}$ and used to evaluate the signal reconstruction quality, and $NSR = \frac{MN}{S}$. As shown in the figure, with compressive sensing, the signal can not be sampled and reconstructed correctly when the sampling rate is below a threshold. However, when the sampling rate goes beyond the threshold, the signal reconstruction quality improves significantly. These thresholds are the minimal sampling rates required for ideal sensing and reconstruction of sparse signals. Taking into account the numerical resolution limit of the simulation tool, we consider that the signal is reconstructed perfectly when the MSE approaches -200dB. Therefore, for signals with a sparsity

of [4%, 10%, 15%, 20%, 25%, 30%], the corresponding sampling rate is [0.26, 0.44, 0.56, 0.62, 0.72, 0.81] of the Nyquist rate respectively. The signal sparsity actually implies the information rate the signal carries and the sampling rate with compressive sensing is determined by the signal's information rate rather than its bandwidth. For signals that are very sparse, the sampling rate reduction can be huge, which implies a great potential saving on the power consumption for signal digitization. Note that since $NSR = \frac{MN}{S}$, the sampling rate reduction at each parallel path which is equal to $\frac{M}{S}$ is more significant.

Based on the results in Fig. 11, we get the relationship between the minimum required NSR for perfect signal reconstruction with different sparsity under a noise-free environment, which is plotted in Fig. 12. Also plotted is a theoretical prediction curve (the red curve with triangle marks) on the minimum NSR, which is based on the results that the minimum number of measurements needed for perfect signal reconstruction of a K -sparse vector with a dimensionality of S with convex optimization is on the order of $K \log(1+S/K)$ [29], [30], [75]. Comparing both curves, we can see a good match between the simulation results and the theoretical prediction.

2. Tradeoff between the System Complexity and the Sampling Rate Reduction

Recall that for robust signal reconstruction, the *measurement matrix* must satisfy the RIP [30]. Also recall the measurement “matrix” of the PSCS front-end shown in Fig. 10, with which we can roughly inspect how good the architecture is in terms of “RIP”. For example, when $M = 1$, that is, no segmentation, it is usually out of the question that the “matrix” has good “RIP” with Gaussian or Bernoulli as the basis functions. When $N = 1$,

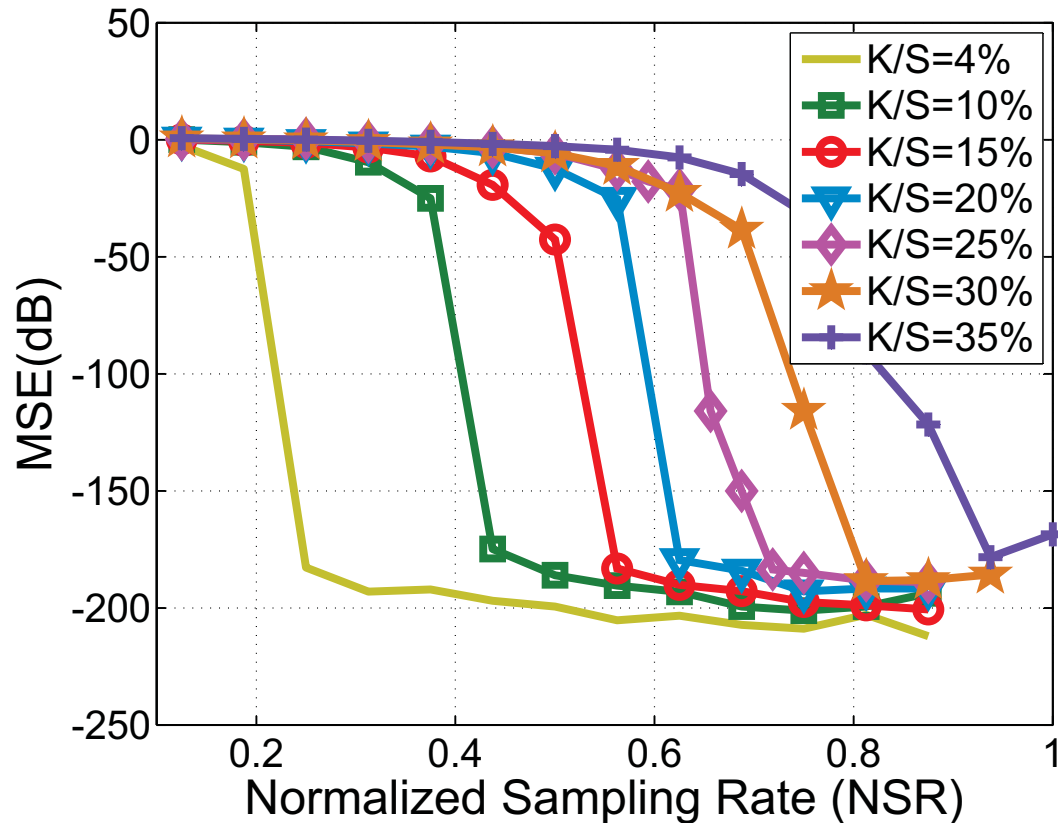


Fig. 11. MSE of the reconstructed signal versus the normalized sampling rate for signal with different sparsity under a noise-free environment, where the input signal is a K -sparse multi-carrier signal with 128 possible subcarriers and linear programming is used for reconstruction.

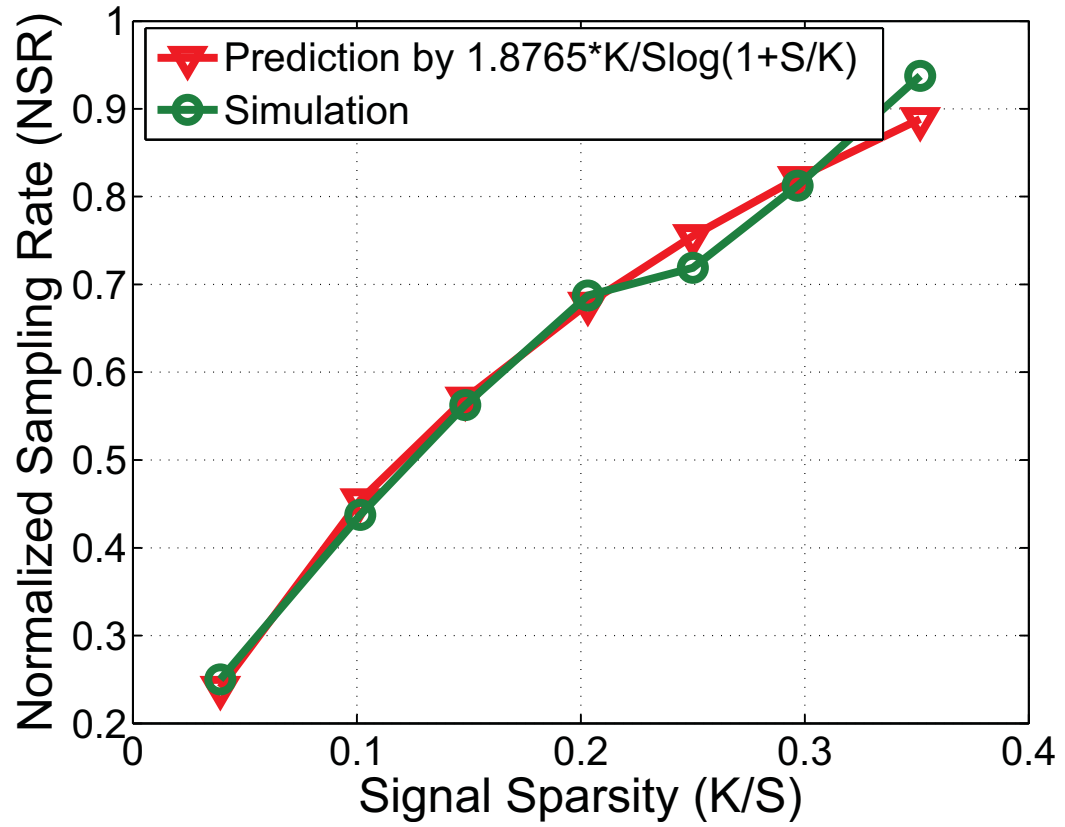


Fig. 12. The minimum normalized sampling rate for signals with different sparsity under a noise-free environment, where the input signal is a K -sparse multi-carrier signal with 128 possible subcarriers and LP is used for reconstruction.

those zeros introduced by segmentation may disturb the “RIP” of the “matrix”. In this section, we investigate through simulations how the system performance changes as the parameters N, M change.

In our simulations, the input signal is a frequency-domain 10-sparse OFDM signal with a finite dimension of $S = 256$, as modeled in Equation (3.3). The coefficients \mathbf{a} are QPSK modulated, the window has an overlapping ratio of 10%, second order Butterworth filter is used to filter the out of band noise, and the joint OMP described in section C.2 is used to reconstruct the signal. We also assume perfect CSI and SNR=10dB, and define the *Success Reconstruction Rate* as one minus the *Block Error Rate* of OFDM symbols and the *Symbol Error Rate* as the error rate of QPSK-modulated coefficients.

Fig. 13 and Fig. 14 show the *Success Reconstruction Rate* and *Symbol Error Rate* under different M respectively, with $S = 256$ and $K = 10$. As shown, given the same number of samples per branch, the signal reconstruction quality improves with more parallel branches. On the other hand, given the same reconstruction quality, the number of parallel branches can be reduced by decreasing T_c and thereby increasing the sample rate for each branch.

In Fig. 15, the number of parallel branches N is plotted against the number of samples per branch M with $S = 256$ and $K = 10$, given the target *Success Reconstruction Rate* of 95% which approximately corresponds to a *Symbol Error Rate* of 10^{-4} . For comparison, we also plot the curve of $N = \frac{140}{M}$ in the same figure. Comparing the simulation curve with the curve of $N = \frac{140}{M}$, we can make two important observations. First, the system works at sub-Nyquist rate. If sampled according to the Nyquist rate, there will be $S = 256$ samples

needed for one OFDM symbol period T ; whereas in our PSCS structure, each ADC needs to generate no more than 20 samples during each T and even the total number of samples $L = MN$ is approximately equal to 140 which is still less than 256. This significant reduction on the sensing rate is the benefit of parallelization and compressed sensing. Second, the number of parallel branches N is approximately inversely proportional to the number of samples per branch M , which presents a tradeoff between the system complexity and the sensing rate. For example, without segmentation, the sensing rate per branch is only $1/256$ of the Nyquist rate, but more than 100 parallel branches are required to have a satisfactory reconstruction quality; with 20 segments, only 8-10 parallel branches are needed, which is affordable for practical implementation, but the sensing rate is increased by 20 times. This design flexibility between the system complexity and the sampling rate makes it possible to tune the system parameters according to the specific application environment and needs.

3. Flexible Spurious Frequency Rejection

The overlapping windowed integration of the PSCS front-end provides a flexible scheme to reject the spurious frequency components.. Since one critical type of spur in the PSCS architecture is the leakage of the clocks for the PN generators to the integrator, as illustrated in Fig. 16, we will focus on this particular type of spur in this section, although the rejection scheme applies more generally.

Recall that in Fig. 8, the output after the mixer is sent to a sliding window with a width of T_c and integrated over T_c seconds, and there is an overlap time of $T_c \times OVR$ between two adjacent windows as illustrated in 9. The integrator, with a reset every T_c seconds, provides

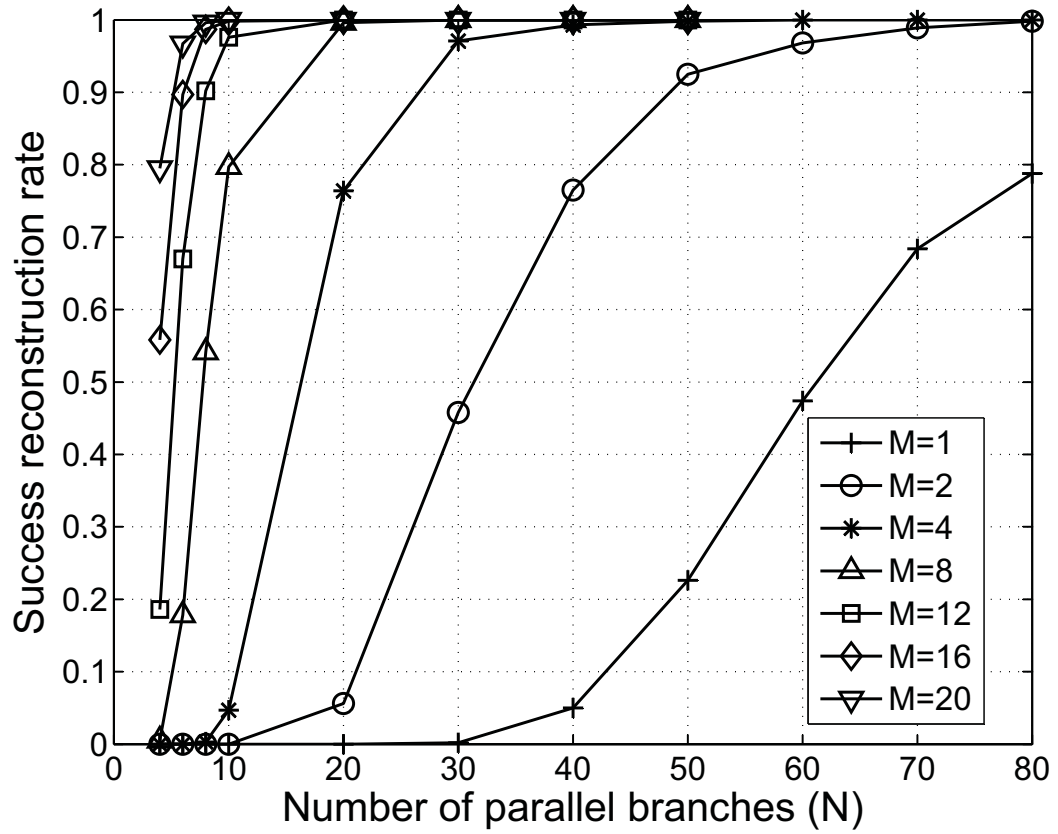


Fig. 13. Perfect reconstruction rate with different number of segments.

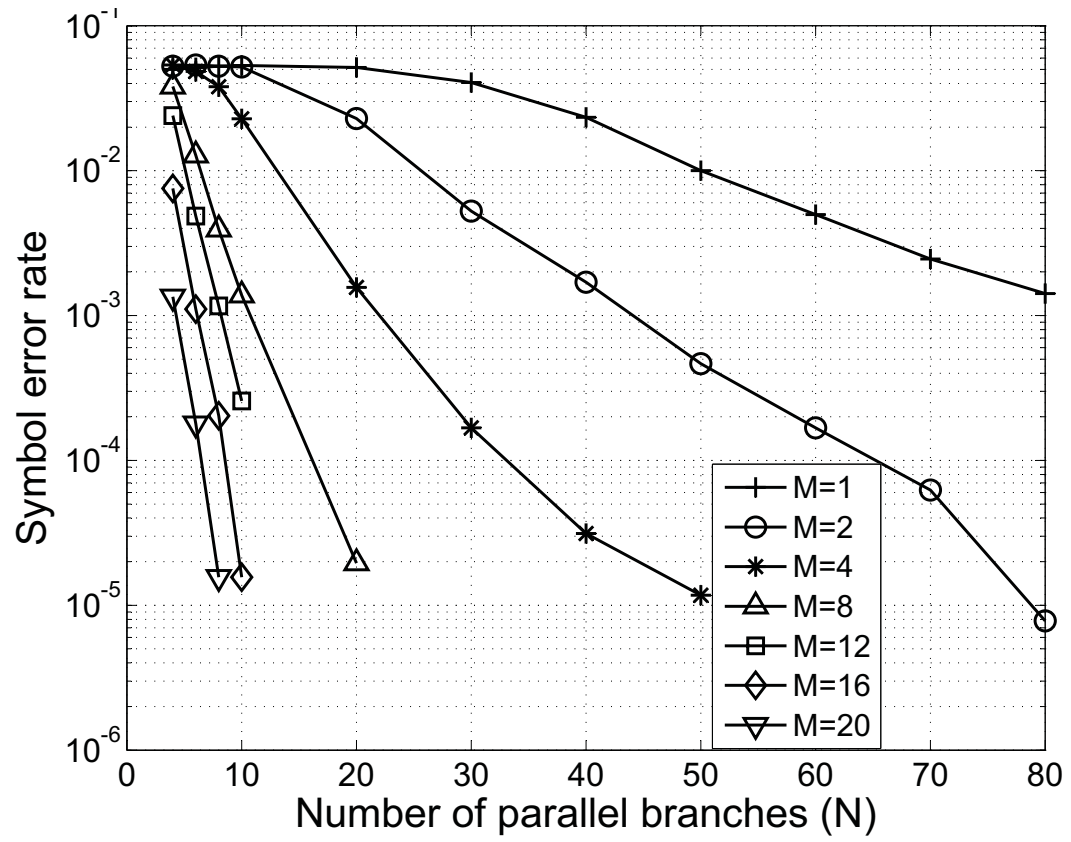


Fig. 14. Symbol error rate with different number of segments.

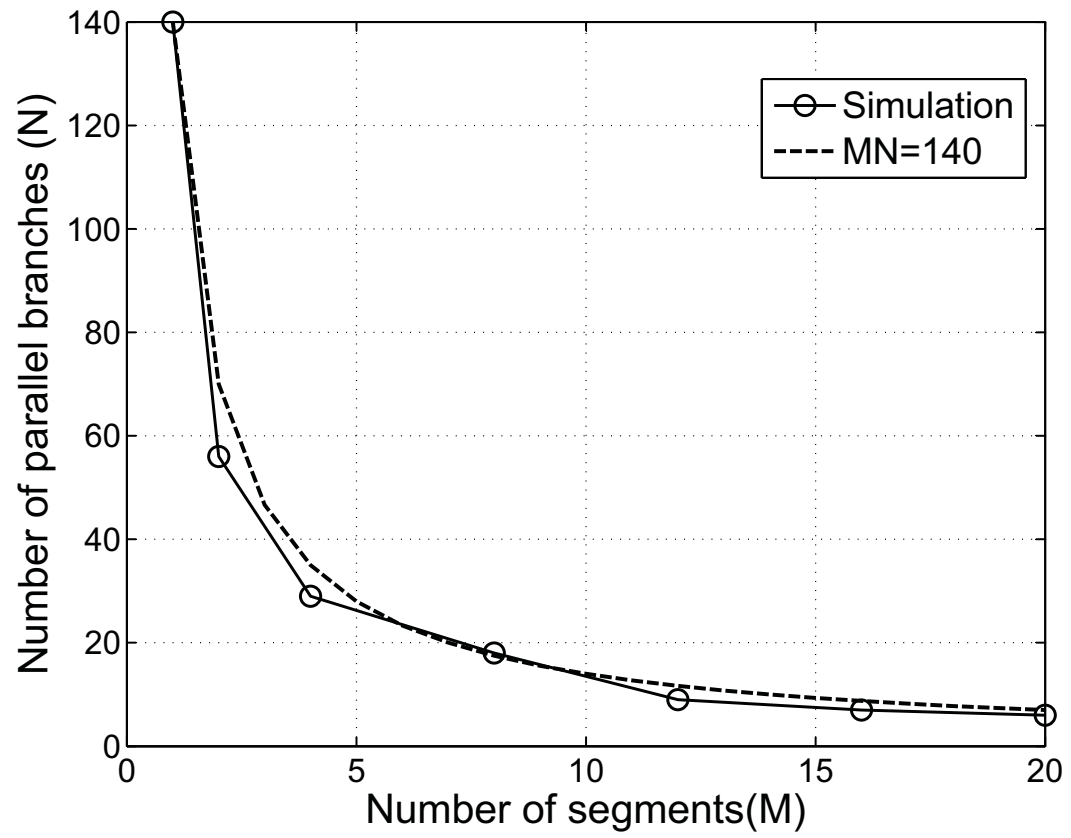


Fig. 15. Impact of number of segments on the number of measurements required per segment.

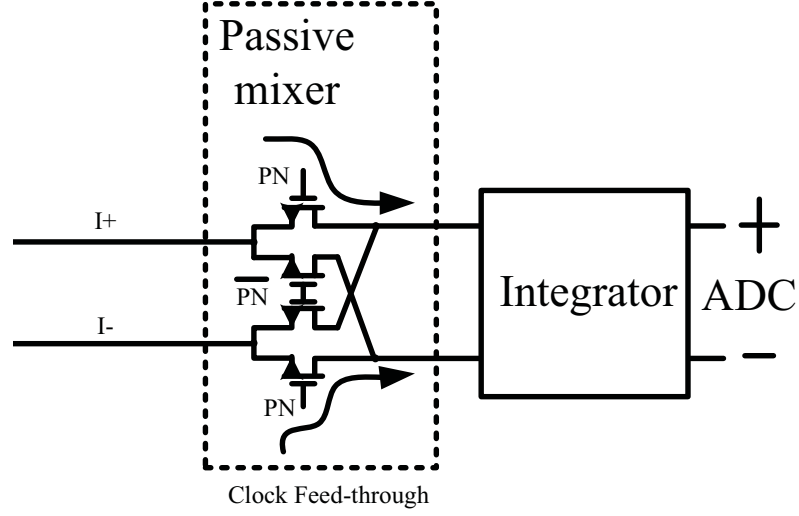


Fig. 16. Clock leakage into the integrators from the clock of the PN generators.

a simple realization of a sinc type low-pass filter with nulls at frequencies of $f_0 \times k$, where $f_0 = 1/T_c$. By setting the random generator clock frequency equal to a harmonic of the reset frequency, the sinc nulls coincide with spur frequencies from the random generator clock and so filters them, where the overlapping scheme provides the flexibility on setting the locations of the nulls. In some cases, without the overlapping scheme, the objective of setting the clock frequency on the nulls of the sinc type lowpass filter may conflict with the sampling rate requirement which is determined by the signal's sparsity. In order to show this, consider the following example.

Let the input signal to the PSCS architecture be a *19-sparse* frequency-domain multi-carrier signal with 128 subcarriers, i.e., $S = 128$ and $K = 19$, which corresponds to a sparsity of 15%. The subcarrier spacing $\Delta f = 1\text{GHz}/128 = 7.8125\text{MHz}$ and the symbol duration time $T_s = 1/\Delta f = 128\text{ns}$. The locations of the K active subcarriers are chosen

randomly and changed every T_s seconds. According to simulation results, the minimum NSR is $0.5625 = 72/128$ for this parameter setup. Equivalently speaking, 72 samples are needed per 128ns to reconstruct the signal perfectly. Using two parallel paths, 36 samples are collected every 128ns at each path, i.e., $M = 36$ and $N = 2$. With this parameter setup and without the overlapping scheme, $T_c = T/M = 128/36 = 3.56ns$, $f_0 = 1/T_c = 281.25MHz$ and the nulls of the sinc type lowpass filter occur at $k \times 281.25MHz$.

There may exist some leakage into the integrators from the clock signal, as illustrated in Fig. 16. According to the CS theory, the clock frequency is usually at the Nyquist frequency f_{Nq} where $f_{Nq} = 1GHz$ in this example. Because $f_{Nq}/f_0 \approx 3.56$, the spurs due to the clock leakages will fall near the 3rd sidelobe's peak of the sinc type lowpass filter and bring distortion to the reconstructed signal. With the overlapping scheme, we can choose $T_c = 4ns$ and $f_0 = 250MHz$ by introducing an overlapping ratio of 11.43%³, then $f_{Nq}/f_0 = 4$ and the spurs due to the clock leakage can be filtered. Based on Fig. 9, this can be mathematically expressed as:

$$T = T_c(M - (M - 1)OVR), \quad (3.7)$$

$$f_{Nq} = S/T, \quad (3.8)$$

$$f_0 = 1/T_c, \quad (3.9)$$

$$\Rightarrow \frac{f_{Nq}}{f_0} = \frac{S}{M - (M - 1)OVR}. \quad (3.10)$$

According to equation (3.10), given a desired sampling rate, or equivalently speaking, a

³Considering the clock resolution requirement, an overlapping ratio of 11.25% is suggested in practice.

specific M , varying OVR will change the relative location of the leakage frequency to the filter nulls, as illustrated in Fig. 17.

Note that if we do not want to introduce any overlapping but still wish to null out the clock leakage, the only option in the above example is to increase the sampling rate and make f_{Nq}/f_0 an integer no less than $\lceil 3.56 \rceil$. By introducing a nonzero OVR , we can conveniently make f_{Nq}/f_0 an integer without increasing the sampling rate.

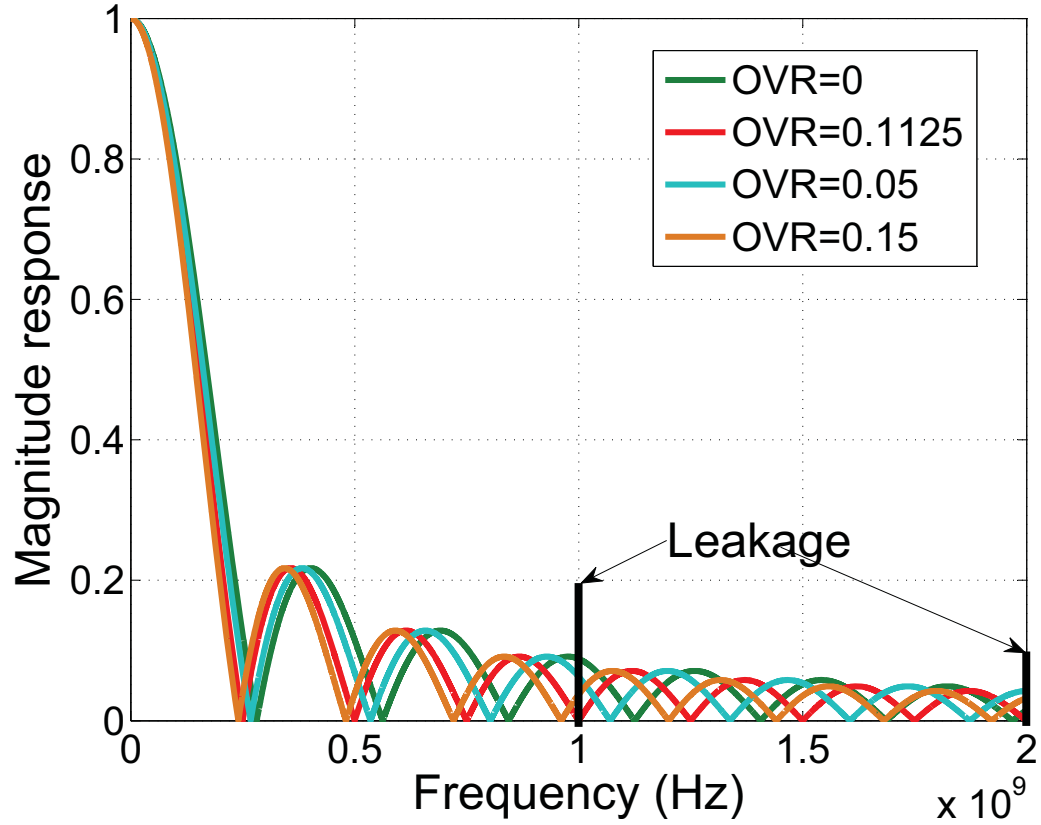


Fig. 17. The location of the spurious leakage frequency relative to the filter nulls with different overlapping ratio. With $OVR = 0$, the strongest clock leakage is close to the peak of the filter's 3rd sidelobe; with $OVR = 0.1125$, the strongest clock leakage is on the 4th null of the filter.

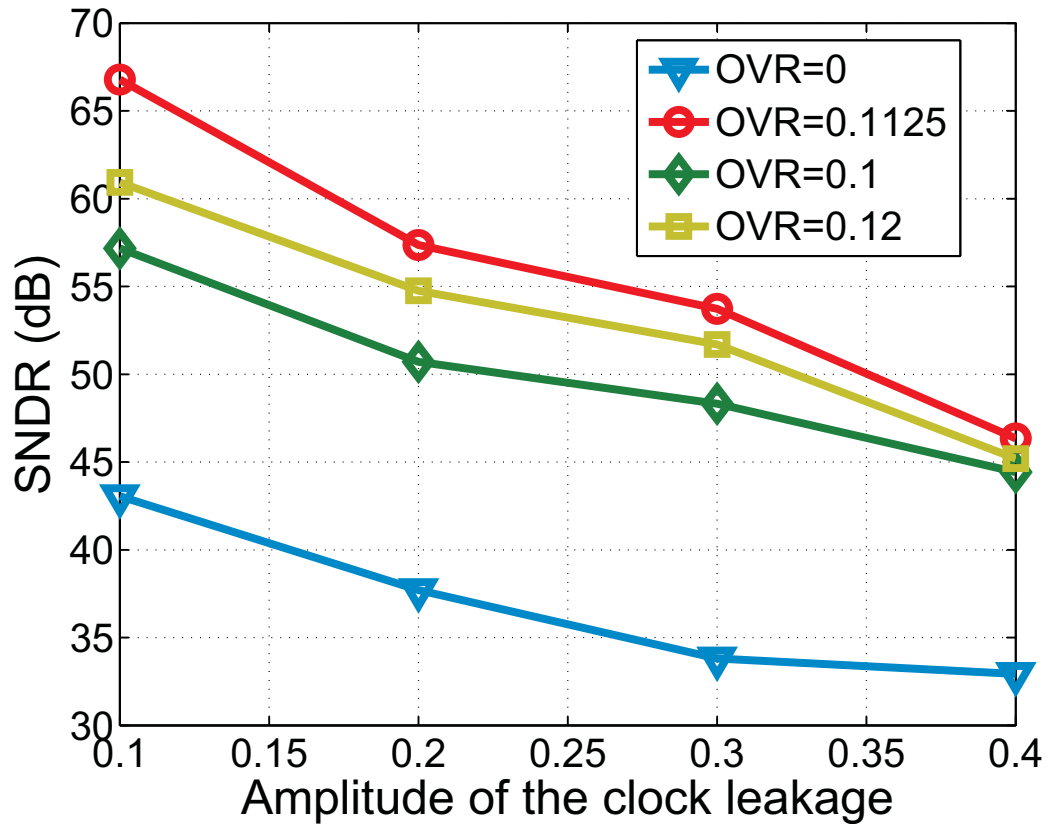


Fig. 18. MSE of the reconstructed signal with different overlapping ratio when there is clock leakage, where the input signal is a 18-sparse multi-carrier signal with 128 possible subcarriers and sampled by the 2-path PSCS working at 56.25% of the Nyquist rate.

Fig. 18 shows the MSE of the reconstructed signal versus the overlapping ratio when there is some clock leakage into the integrators. Note that in the simulation the amplitude of each subcarrier is set to 1. Since $K = 19$, the signal's peak amplitude is 19. Allowing a 10dB margin to account for the multi-carrier signal's large peak-to-average ratio, the clock leakage with an amplitude of 0.1 (0.4) is roughly 35dB (23dB) below the signal's average power. As shown in Fig. 18, the flexibility of setting the null frequencies by the overlapping scheme can bring about 20dB gain after filtering the spurs due to the clock leakage.

Note also that the overlap in the integration windows provides wider filter nulls than the sinc filter. Because of the existence of the phase noise on the clock signal in practice, even if we can set the clock on the null frequency, it is inevitable there remains some leakage due to the widening of the spurs spectrum. The wider nulls provides the possibility of further improving the harmonic rejection when the phase noise is significant.

E. Summary

In this chapter, the proposed mixed-signal compressive sensing system based on the PSCS front-end is introduced, from the signal modeling, to the PSCS front-end architecture, to the signal reconstruction. This system is shown to possess attractive features that are critical for the implementation. First, applying the CS framework to the analog signal directly avoids the ADC bottleneck while sensing wideband signals and relaxes the requirements in wideband RF receiver front-ends, and the parallelization further reduces the sampling rate at each parallel path. Second, the parallel structure provides a design flexibility and scalability on the sensing rate and system complexity so that we can tune

the system parameters according to different application environment and needs. Third, the overlapping windowed integration of the PSCS front-end provides a flexible scheme to reject the spurious frequency components, for example, the clock leakage from the PN generators to the integrators.

CHAPTER IV

ROBUSTNESS OF MIXED-SIGNAL COMPRESSIVE SENSING SYSTEM AGAINST ADC NONLINEARITY

Mixed-signal compressive sensing holds new promise for the digitization of wideband frequency-domain sparse signals at sub-Nyquist rate sampling without compromising the reconstruction quality and therefore avoids the ADC bottleneck while digitizing wideband signals. Different from the conventional time-domain Nyquist-rate sampling, in compressive sensing systems the sparse signal is projected into a transform-domain over which the sampling occurs and this procedure is referred as *random projection* or *random measurement*, as introduced in Chapter II. The ideal signal reconstruction from the sub-Nyquist rate samples is to resolve the optimization problem as given in (2.7) and (2.8) rather than the traditional interpolation for Nyquist rate sampling reconstruction [76]. There are many mature algorithms to resolve the optimization problem, as summarized in Chapter II.

Recall that in the PSCS system given in Fig. 6, the samples obtained at sub-Nyquist rate needs to be digitized by low-rate ADCs. Generally speaking, in a multi-stage RF front-end, the linearity of the last stage is very critical to the overall linearity of the whole front-end, [77], [78]). It is important to study how the mixed-signal CS front-end reacts to the ADC nonlinearity. In a conventional receiver (direct conversion or superheterodyne architecture [77], [78]), the signal is sampled at Nyquist rate and the time-domain samples are sent to ADCs directly; however, in a CS receiver architecture, since the signal is randomized before sampling and the samples sent to ADCs are no longer the original time-domain

samples, the random projection in a CS receiver implies that the ADCs nonlinearity has a different impact on the reconstructed signal quality. In this chapter, we investigate how the ADC nonlinearity influences the signal reconstruction quality during the mixed-signal compressive sensing of frequency-domain sparse signals and show the potential benefit brought by the random projection quantified in terms of the ADC SFDR (Spurious Free Dynamic Range).

A. Impact of Randomization

As mentioned before, the main difference between the CS receiver front-end and a conventional receiver front-end is that the signal sent to the ADC in the former is not the original input signal but the input signal after some randomization. Therefore, the ADC nonlinearity impacts the reconstructed signal quality in a different way. To the best of the authors' knowledge, this important phenomenon has not been reported in the literature. As an illustration, Fig. 19 shows the signal spectrum at various building blocks in the sampling architectures during a two-tone nonlinearity test. Note that an ADC with nonlinear distortion is represented by a nonlinear block followed by an ideal ADC. For simplicity, only the third order distortion is considered. In the conventional receiver, the input two-tone test signal directly undergoes the effect of the ADC nonlinear distortion resulting in the third order harmonics and inter-modulation components in the spectrum of the reconstructed signal. The spurious energy is concentrated on the harmonics and inter-modulation components. On the other hand, in the CS receiver, the input signal is mixed with the PN sequence whose spectrum looks like white noise spectrum shaped by the *sinc* function with the first

null frequency at f_{clk} (the clocking frequency for the PN generator, which is the Nyquist rate). The randomized signal is sent to a low-pass filter with a cutoff frequency of f_{cutoff} . Usually f_{cutoff} is much lower than f_{clk} because of the sub-Nyquist sampling capability of CS receivers. For example, in the testbed in [79], $f_{clk} = 1MHz$ and f_{cutoff} is about $30KHz$. Consequently, the spectrum of the signal sent to the ADC is relatively flat within the filter passband. As a result, the harmonics and inter-modulation components caused by the ADC nonlinear distortion occur everywhere. In other words, the spurious energy due to the ADC nonlinearity is spread along the signal bandwidth rather than concentrated on a few tones, which can lead to a better SFDR after reconstruction.

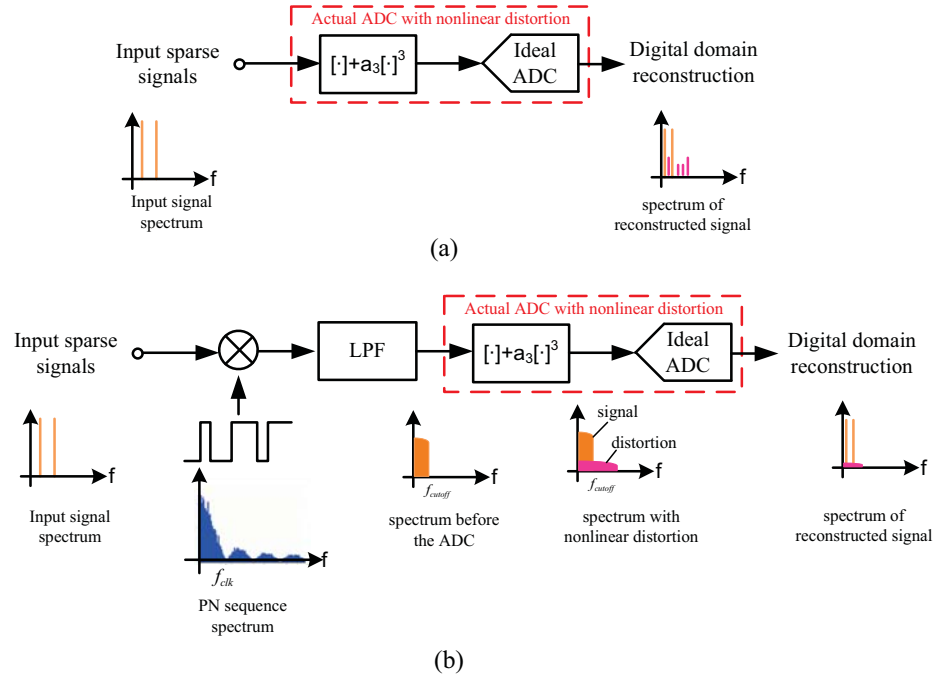


Fig. 19. Sketch of the signal spectrum at different stages of a receiver front-end in the two-tone test. (a) conventional receiver front-end. (b) compressive sensing receiver front-end.

B. Simulations

1. Simulation Setup

A series of Monte Carlo simulations were performed to validate the above conjecture. Specifically, we did a two-tone test for both the conventional Nyquist sampling architecture and the CS receiver and compare the SFDR of both architectures, the main setup of which is summarized as follows:

- The input test signal is a 2-sparse frequency domain sparse signal, where the signal basis is the frequency set $\{i \times 10MHz\} (i = 1, 2, \dots, 128)$, and the signal sparsity is 2%. Mathematically, the input test signal $r(t) = a_1 e^{j2\pi f_1 t} + a_2 e^{j2\pi f_2 t}$, where $a_1 = a_2 = 1$ without the loss of generality, $f_1, f_2 \in \{i \times 10MHz\}$, a_1, a_2 and f_1, f_2 are unknown.
- Because the maximum frequency span of the two test tones can be as large as 1.28 GHz, the sampling rate in the conventional receiver is 2.56 GHz, that is, the $f_{Nyquist} = 2.56GHz$. The sampling rate in the CS receiver is denoted by its Normalized Sampling Rate (NSR), which is defined as the ratio of the CS receiver sampling rate over the Nyquist sampling rate.
- Since the third order nonlinear distortion is usually the most critical distortion, the ADC nonlinearity is modeled as $z = y + c_3 y^3$, where y is the input, z is the corresponding output and c_3 is the coefficient of the third-order nonlinear distortion. For a fair comparison, the input signals to the ADC in both receivers were scaled appropriately to be full-scale.

- In the conventional Nyquist sampling architecture, the input test signal $r(t)$ is sampled in the time-domain at $f_{Nyquist}$, the resulting samples $\mathbf{y}_{Nyquist} = r(n\Delta t)$ ($n = 1, 2, \dots$), where $\Delta t = 1/f_{Nyquist}$. $\mathbf{y}_{Nyquist}$ are first normalized to the ADC full-scale through $\bar{\mathbf{y}}_{Nyquist} = \mathbf{y}_{Nyquist} / \max(\text{abs}(\mathbf{y}_{Nyquist}))$, where $\bar{\mathbf{y}}_{Nyquist}$ is the normalized samples sent to the ADC. The ADC introduces some nonlinearity to those time-domain samples through $\mathbf{z}_{Nyquist} = \bar{\mathbf{y}}_{Nyquist} + c_3 \bar{\mathbf{y}}_{Nyquist}^3$. The input signal spectrum is estimated from these time-domain samples with nonlinear distortion via DFT.
- In the CS receiver, the input testing signal $r(t)$ goes through random projection, filtering and sampling, the resulting transform-domain samples $\mathbf{y}_{cs} = \Phi\Psi\mathbf{a}$. Similarly, \mathbf{y}_{cs} is first normalized to ADC full-scale through $\bar{\mathbf{y}}_{cs} = \mathbf{y}_{cs} / \max(\text{abs}(\mathbf{y}_{cs}))$, where $\bar{\mathbf{y}}_{cs}$ is the normalized samples sent to the ADC. The ADC introduces some nonlinearity to those time-domain samples through $\mathbf{z}_{cs} = \bar{\mathbf{y}}_{cs} + c_3 \bar{\mathbf{y}}_{cs}^3$. The input signal spectrum is estimated from these time-domain samples with nonlinear distortion via solving the following optimization problem.

$$\hat{\mathbf{a}} = \arg \min \|\mathbf{a}\|_1 \quad s.t. \quad \|\mathbf{y} - \Phi\Psi\mathbf{a}\|_2 \leq \epsilon_n + \epsilon_d, \quad (4.1)$$

where ϵ_n is the error due to the noise, ϵ_d is the error due to the nonlinear distortion.

2. Simulation Results

a. Noise-free Environment

First, we compare the SFDR of the Nyquist sampling architecture and the CS front-end in a noise-free environment.

Fig. 20 gives snapshots of the two-tone test reconstructed signal spectrum for both sampling architectures. The sampling rate of the CS receiver is $240MHz$ and the third-order distortion coefficient is $c_3 = 0.2$. As we can see, in the conventional receiver, the spurious energy due to the ADC nonlinearity concentrates on the two third-order harmonics and two third-order inter-modulation components, leading to a SFDR of 16.5 dB, whereas in the CS receiver, the spurious energy is spread along the whole signal bandwidth leading to a SFDR of 29.7 dB. This is more than a 13 dB improvement. The observation from this simulation was intuitively illustrated in Fig. 19.

Fig. 21 compares the SFDR distribution of the reconstructed signal during 10000 times two-tone test realizations, where the sampling rate of the CS receiver is $240MHz$, $c_3 = 0.2$ and the frequencies of the two tones are randomly selected from the frequency set $\{i \times 10MHz\} (i = 1, 2, \dots, 128)$. The result given in Fig. 20 is one of these 10000 realizations. In Fig. 21, the scatter of the SFDR results is shown at left and the corresponding histograms at right. As shown, the randomization in CS receivers leads to a better SFDR.

Another interesting observation is that the distribution of SFDR using CS receiver forms two clusters, one cluster is close to the SFDR distribution of a conventional Nyquist receiver, the other cluster is about 300dB. Taking into account the numeric accuracy of the simulation tool, we can consider achieving a SFDR of 300dB as perfect reconstruction,

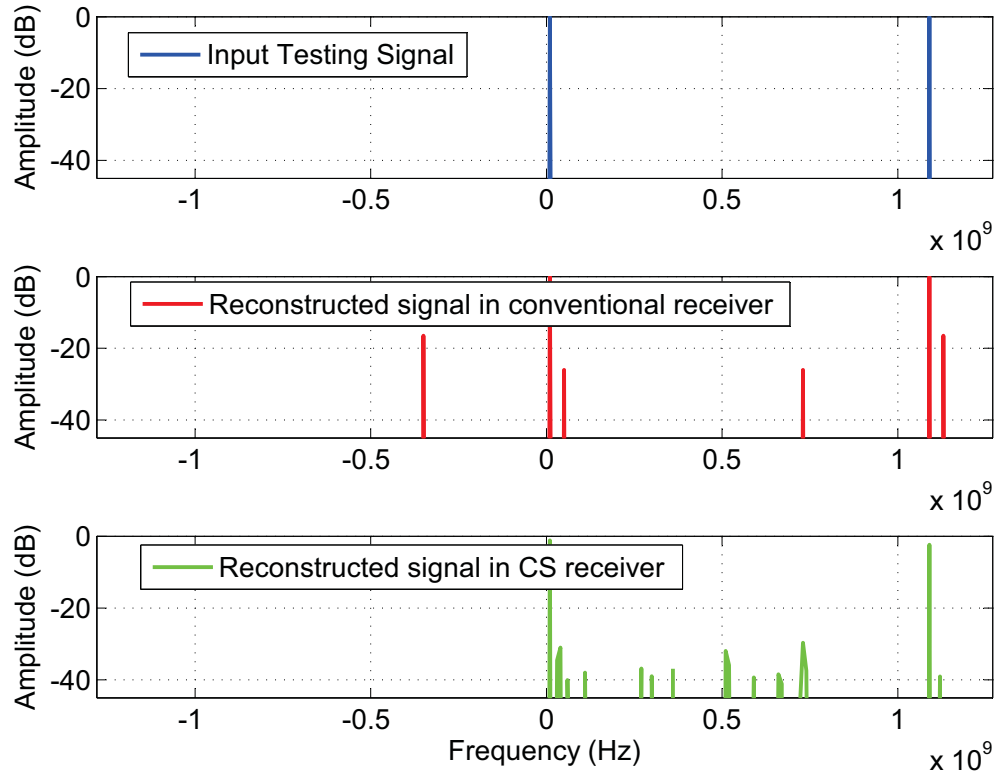


Fig. 20. Snapshot of the signal spectrum under noise-free environment, where the signal has a sparsity of 2%, the third order distortion coefficient $c_3 = 0.2$. From top to bottom: input two-tone test signal, the reconstructed signal using the conventional receiver where the time-domain samples undergoes the ADC nonlinear distortion, the reconstructed signal using the compressive sensing receiver where the samples of the randomized signal undergoes the ADC nonlinear distortion.

Table I. Relationship of the SFDR and the frequency span of two-tone test signals, where the signal has a sparsity of 2%, the third order distortion coefficient $c_3 = 0.2$.

Frequencies (f_1, f_2) (MHz)	(10,1200)	(10,400)	(10,60)
Median $SFDR_{Nyquist}$ (dB)	16.48	16.48	16.48
Median $SFDR_{cs}$ (dB)	31.57	40.1	309

which is possible for CS receivers in a noise-free environment. This is because the minimum sampling rate needed for perfect signal reconstruction with CS depends on the signal information rate, which is related to the frequency span of the two test tones in our simulations. Given the fixed CS sampling rate, as the two test tones get closer, the reconstructed signal quality improves. Therefore, the SFDR varies with the frequency span of the test tones when using the CS receiver. In some cases when the two test tones get really close, the CS reconstruction algorithm can perfectly recover the original signal (SFDR of near 300 dB in Fig. 21) despite the existence of nonlinear distortion. Table I gives an example of this phenomenon, where the CS sampling rate is fixed to be 240MHz and the frequency span of the input two-tone test signal varies. As shown, when the two test tones get closer, the SFDR of the CS receiver improves, the SFDR of the conventional Nyquist sampling architecture remains the same.

Fig. 22 shows the SFDR of both receivers versus the ADC nonlinear distortion coefficient in the two-tone test. As we can see, the SFDR improvement from the randomization in CS receivers is relatively constant given different ADC nonlinear distortion. For a sparse signal with a sparsity of 2%, the SFDR improvement is about 14dB.

Although the randomization in CS receivers changes the distribution of the error power

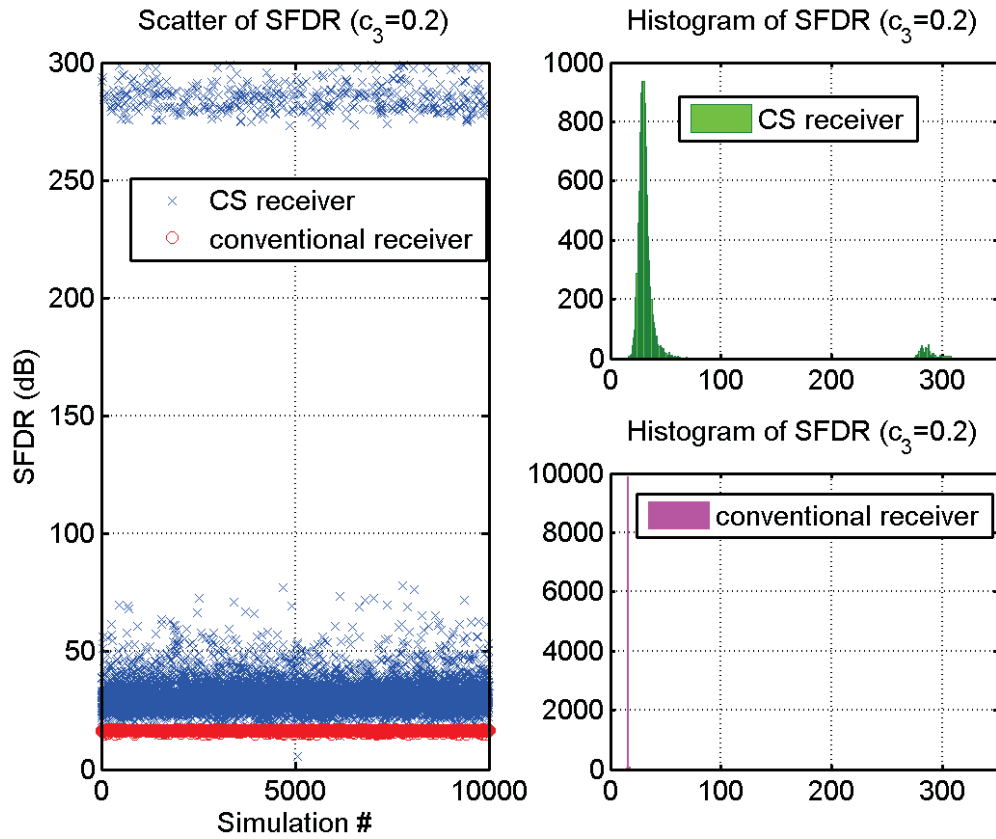


Fig. 21. SFDR comparison between the conventional receiver and the CS receiver in the two-tone test under noise-free environment, where the signal has a sparsity of 2%, the third order distortion coefficient $c_3 = 0.2$.

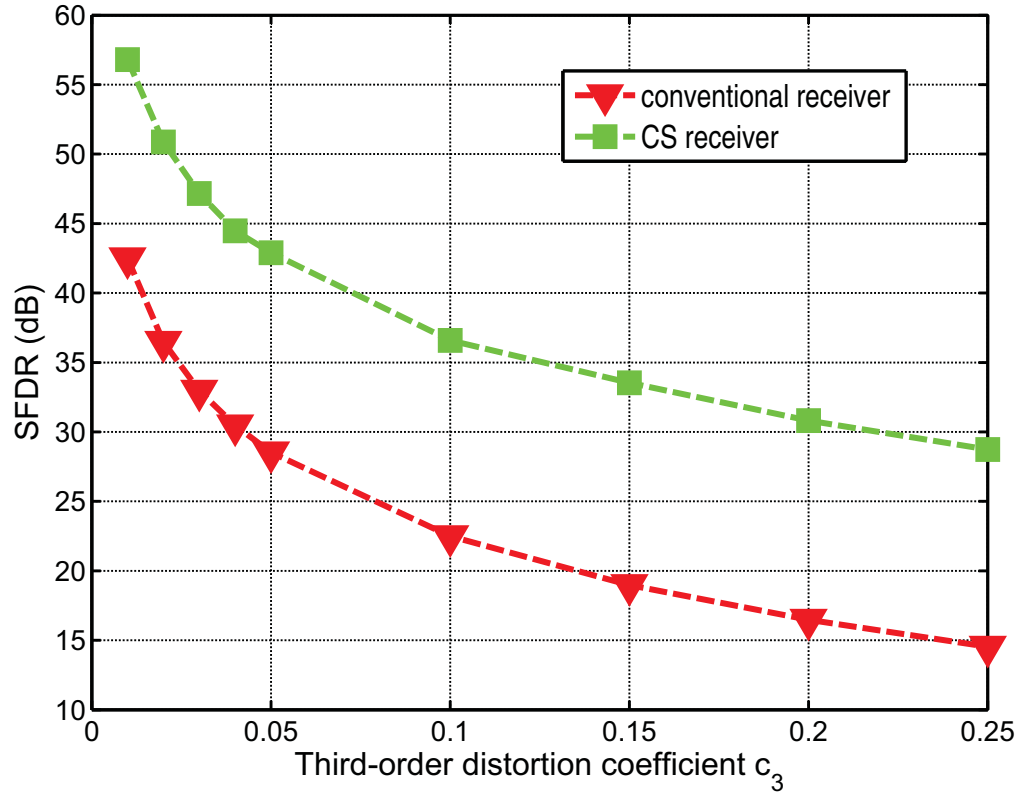


Fig. 22. SFDR comparison between the conventional receiver and the CS receiver in the two-tone test versus different nonlinear distortion under noise-free environment, where the signal has a sparsity of 2%.

from ADC nonlinear distortion, our simulation shows that it does not change the overall SDR (Signal-to-Distortion Ratio). Fig. 23 compares the median SDR (Signal-to-Distortion Ratio) of both receivers in the two-tone test. Note that in our simulations the signals sent to ADCs in both systems are normalized so that their peak amplitude is set to be the full-scale of the ADCs, which means both signals sent to ADCs have the same peak power P_{peak} . However, the signals sent to ADCs in both receivers obviously have different frequency structure, specifically, the signals sent to ADCs in the conventional Nyquist sampling architecture are two-tone signals, whereas those in the CS system have richer spectrum as shown in Fig. 19. With the same peak amplitude, the amplitude of individual frequency component in the conventional sampling architecture is higher than that in the CS architecture and the average power P_{in} in the former is also higher than in the latter. In our simulations, the P_{in} to the CS ADC is about 2.5 dB lower than the P_{in} to the Nyquist ADC, which means a 5 dB inherent gain in terms of the SDR at the ADC output according to the relationship $SDR = 2(IIP3_{ADC} - P_{in})$ [77], [78]. While comparing the SNRs at the output of ADCs of both systems, we need to take this inherent gain in the CS system into account and deduct this extra 5dB gain from the output SDR in the CS system. With this power adjustment, we can see that both receivers have similar SDRs, as shown in Fig. 23. In other words, by spreading the spurious energy along the signal bandwidth, the CS randomization relaxes the requirement on the ADC SFDR specification without sacrificing the overall SDR performance of the receiver.

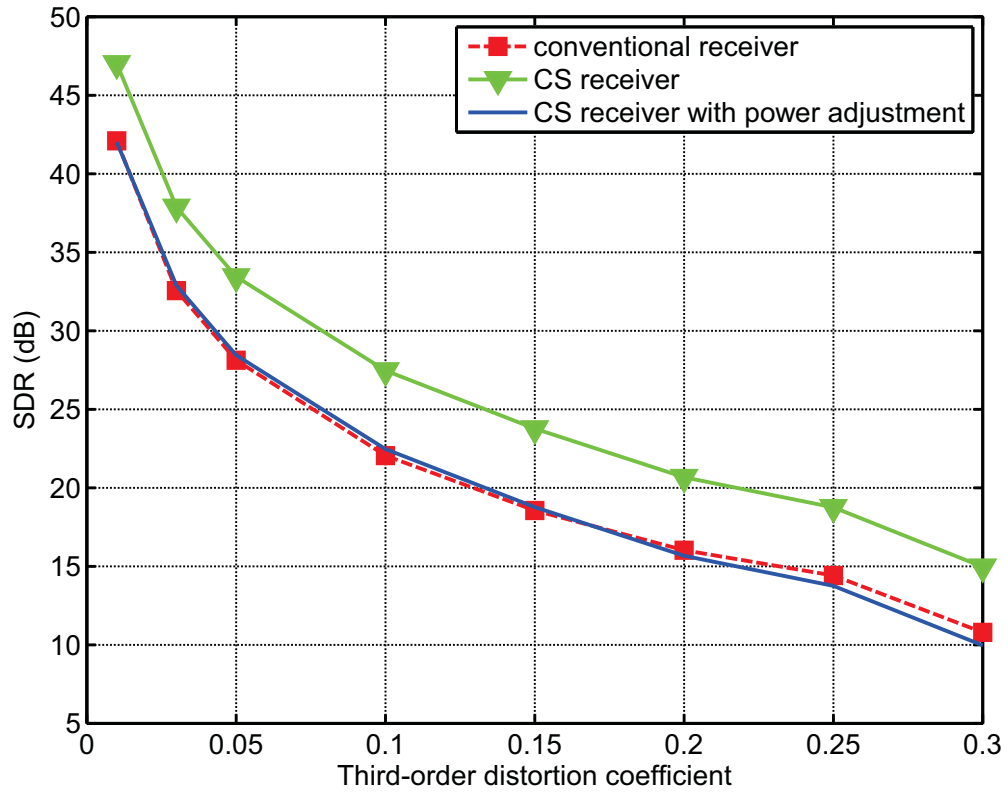


Fig. 23. SDR comparison between the conventional receiver and the CS receiver in the two-tone test versus different nonlinear distortion, where the signal has a sparsity of 2%.

b. Noisy Environment

Next, we compare the SFDR of the Nyquist sampling architecture and the CS front-end in noisy environment (SNR=25dB). Similarly, Fig. 24 gives the snapshots of the reconstructed signal spectrum in both sampling architectures. Fig. 25 compares the SFDR distribution of both sampling architectures. Again, we can see that effect of the nonlinear distortion in the CS receiver is spread out because of the randomization, and the SFDR of the ADC is improved. Fig. 26 shows the SFDR performance of both CS and conventional Nyquist sampling architecture with different nonlinear distortion. Different from the noise-free environment, the SFDR improvement brought by the CS front-end decreases as the nonlinear distortion becomes small. This is because with small nonlinear distortion, the SFDR is limited by the noise rather than the nonlinear distortion.

3. Performance as a Function of Sparsity Variation

So far, our simulation is based on two-tone tests, where the signal has a sparsity of 2%. For such a low-sparsity signal, the signal energy concentrates only on two tones, the change on the energy distribution over the bandwidth after the randomization is very significant, therefore, the SFDR improvement from the spurious energy spreading is also significant. As the signal get less sparse, it is expected that the SFDR improvement from randomization also becomes less significant. Table II lists the SFDR performance as a function of sparsity variation. Note that, for signals with different sparsity, different CS sampling rate is used. As shown in the table, as the signal sparsity changes from 2% to 4% to 10%, for the conventional receiver, given the same power, with more tones, the power of a single tone

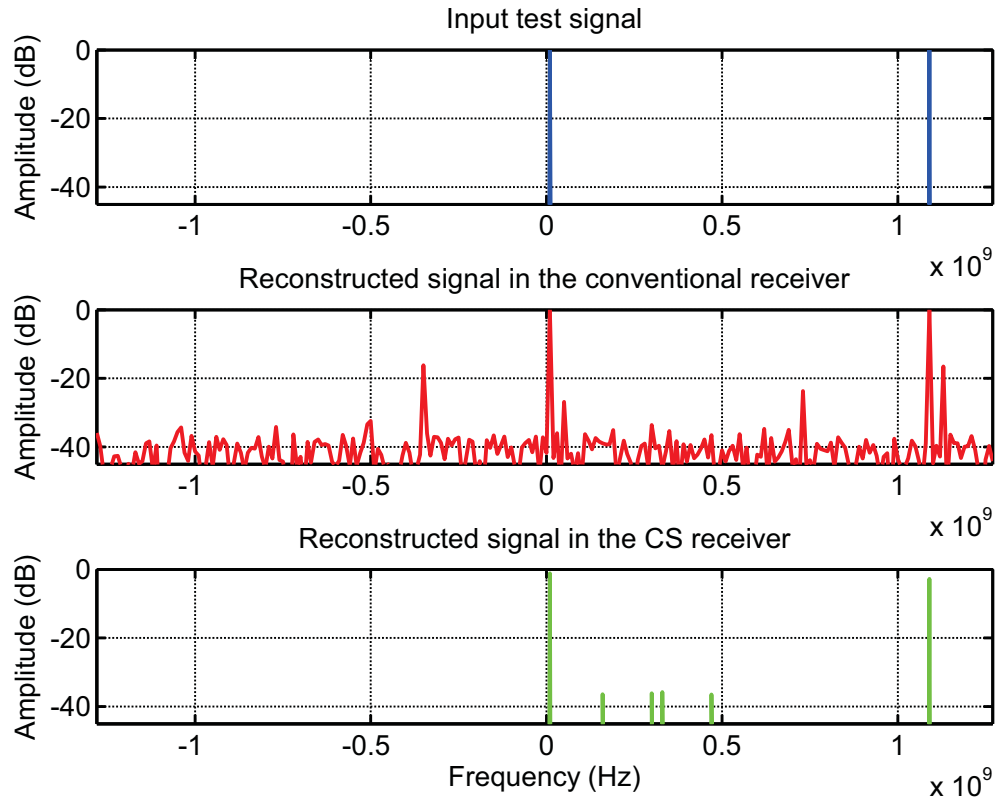


Fig. 24. Snapshot of the signal spectrum under noisy environment, where the signal has a sparsity of 2%, the third order distortion coefficient $c_3 = 0.2$. From top to bottom: input two-tone test signal, the reconstructed signal using the conventional receiver where the time-domain samples undergoes the ADC nonlinear distortion, the reconstructed signal using the compressive sensing receiver where the samples of the randomized signal undergoes the ADC nonlinear distortion.

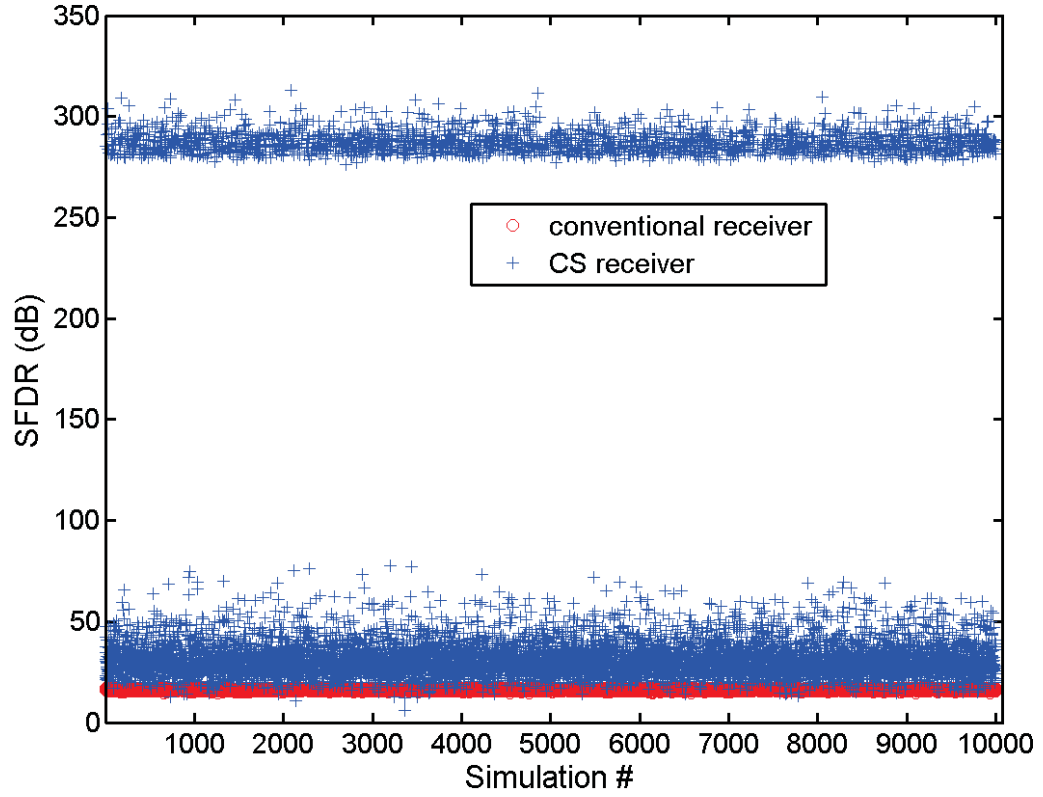


Fig. 25. SFDR comparison between the conventional receiver and the CS receiver in the two-tone test under noisy environment, where the signal has a sparsity of 2%, the third order distortion coefficient $c_3 = 0.2$.

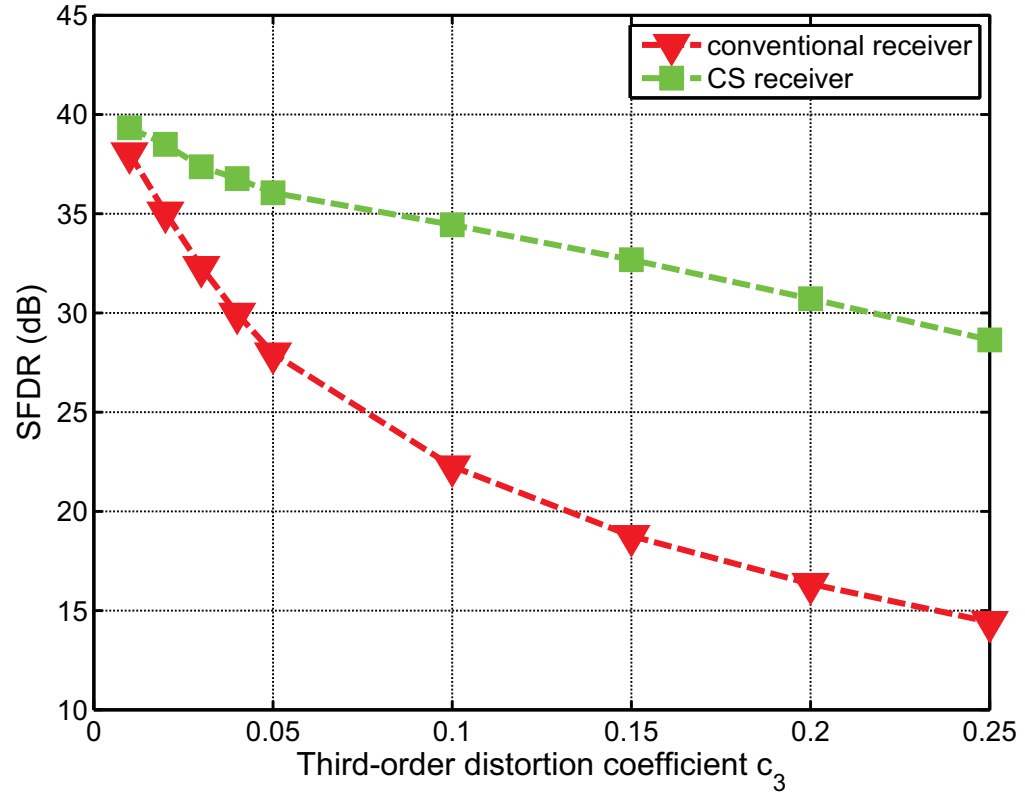


Fig. 26. SFDR comparison between the conventional receiver and the CS receiver in the two-tone test versus different nonlinear distortion under noisy environment, where the signal has a sparsity of 2%.

Table II. Changing of SFDR as a function of sparsity variation, where the third order distortion coefficient $c_3 = 0.01$.

Sparsity level	2%	4%	10%
CS sampling rate (MHz)	240	480	1200
Median $SFDR_{Nyquist}$ (dB)	42.50	48.13	51.47
Median $SFDR_{cs}$ (dB)	56.80	55.58	53.60
SFDR improvement(dB)	14.30	7.45	2.13

is less, which results higher SFDR values; however, for the CS receiver, with more tones, the benefit from the energy spreading becomes less. Therefore, the SFDR improvement of the CS receiver over the conventional Nyquist sampling architecture reduces from 14dB to 7dB to 2dB. At the same time, because the signal gets less sparse, the required sampling rate in the CS receiver increases from 240MHz to 480MHz to 1200MHz and the benefit of sampling rate reduction in the CS receiver becomes less significant. Considering all these changes, we can see that in the regime where the benefit of sampling rate reduction from compressive sensing is significant, the SFDR improvement from randomization of the CS receivers is also attractive.

C. Summary

In this chapter, the impact of ADC nonlinearity in a mixed-signal compressive sensing system for frequency-domain sparse signals is investigated. The signal spectrum at each building block in the CS receiver is analyzed and compared with conventional Nyquist sampling architecture. In the mixed-signal compressive sensing system, the input signal

is randomized before going through sampling and reconstruction. Therefore, the ADC nonlinearity does not affect directly the original signal but the randomized signal. As a result, when processing frequency-domain sparse signals, the spurious energy due to the ADC nonlinearity spreads along the signal bandwidth rather than get concentrated on a few frequencies, which provides improvement on the ADC SFDR. Simulation results show that for sparsity signals with a sparsity of 2%, the CS receiver ADC SFDR improvement compared to a conventional Nyquist sampling architecture can be up to 14 dB.

CHAPTER V

EFFECT OF CIRCUIT NONIDEALITIES AND BACKGROUND CALIBRATION

A. Effect of Circuit Nonidealities

The PSCS front-end is based on the mixed-signal processing where the accuracy of the analog circuit components becomes critical to the overall performance, especially when the technology scaling makes it more challenging to design analog circuit components with high accuracy. There are many factors that contribute to the imperfection of the system and some of them are listed below:

- the thermal noise and flicker noise
- the finite settling time
- the timing uncertainty
- the frequency offsets
- the gain and phase mismatches among paths
- the quantization noise

Considering all the nonideal factors, the actual relationship between the collected samples \mathbf{y} and the coefficients \mathbf{a} becomes

$$\mathbf{y} = \tilde{\mathbf{V}}\mathbf{a} = (\mathbf{V} + \delta\mathbf{V})\mathbf{a}, \quad (5.1)$$

where the $\tilde{\mathbf{V}}$'s element at the $mN + n$ row and the s column is given by

$$\tilde{V}_{mN+n,s} = \int_{mT_m+\delta t_1}^{mT_m+T_c+\delta t_2} \alpha e^{j2\pi(s\Delta f+\delta f)t+\theta} (\Phi_n(t) + \delta\Phi_n(t))^* dt, \quad (5.2)$$

where, the δt_1 and δt_2 reflects the timing error on the slicing window, δf reflects the frequency offset, α and θ reflects the gain and phase mismatches, and the $\delta\Phi_n(t)$ reflects the error of the random basis which could be attributed to the jitter and non-zero response time.

Because the actual relationship between \mathbf{y} and \mathbf{a} is given by (5.1), we need to replace \mathbf{V} with $\tilde{\mathbf{V}}$ in (2.7) when estimating \mathbf{a} , otherwise, some extra error will be introduced. In the left part of this section, we will show the effect of different kinds of nonideal factors through a series of simulations. In the simulation, the input signal to the PSCS architecture is a *16-sparse* frequency-domain multi-carrier signal with 128 subcarriers, i.e., $S = 128$ and $K = 16$. The subcarrier-spacing $\Delta f = 1GHz/128 = 7.8125MHz$ and the symbol duration time $T = 1/\Delta f = 128ns$. The location of the 16 active subcarriers are chosen randomly and changed every T seconds. The effect of thermal noise is not considered here since its effect can be addressed as in the optimization problem in (2.8) accordingly [29,30].

Fig. 27 gives the MSE (Mean Square Error) of the reconstructed signal versus the NSR (Normalized Sampling Rate) when there is no circuit imperfections, where $MSE = \frac{\|\mathbf{a}-\hat{\mathbf{a}}\|_2}{\|\mathbf{a}\|_2}$ and $NSR = \frac{MN}{S}$. As shown, the MSE is around -200dB when the NSR is increased up to around 0.5, which means that the signal can be viewed as reconstructed perfectly when the sampling rate goes beyond half of the Nyquist rate. Note that since $NSR = \frac{MN}{S}$, the sampling rate reduction at each parallel path which is equal to $\frac{M}{S}$ is more significant.

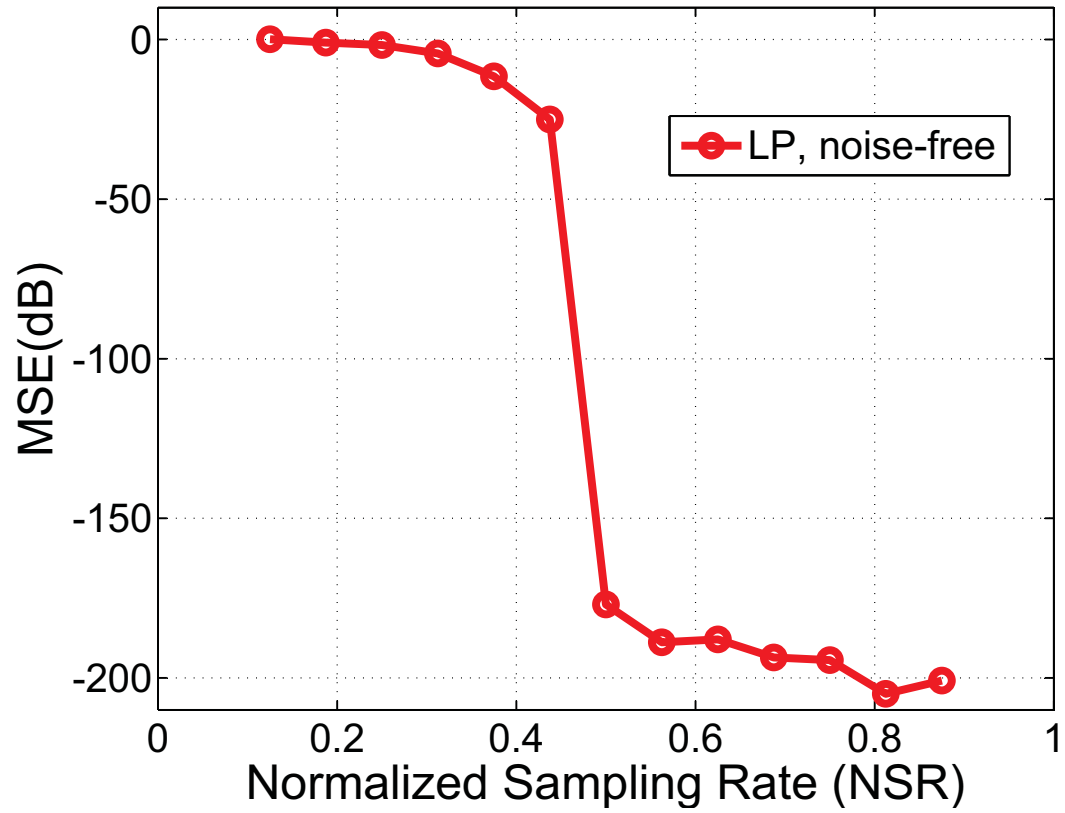


Fig. 27. MSE of the reconstructed signal versus the normalized sampling rate when there are no imperfections.

Fig. 28 shows the MSE of the reconstructed signal when the PN sequences have finite settling time. Fig. 29 shows the MSE of the reconstructed signal when the sliding window has a timing uncertainty on its edges and the amount of uncertainty is denoted by the standard deviation of the introduced jitter. From these figures, we can see the system performance degrades if the circuit nonideal factors are not treated properly. For example, with a finite settling time of 30ps, the best achieved MSE is only -20dB and with a windowing timing uncertainty of 5ps, the best achieved MSE is about -40dB.

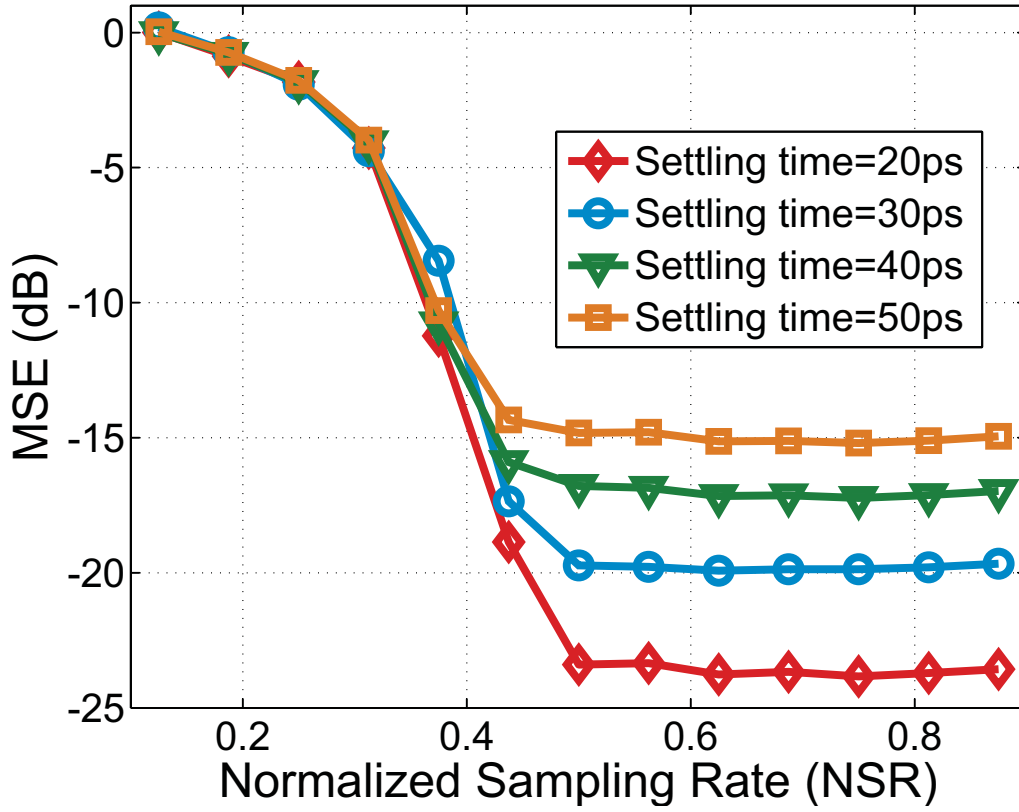


Fig. 28. MSE of the reconstructed signal versus the normalized sampling rate when the random PN sequences have finite settling time.

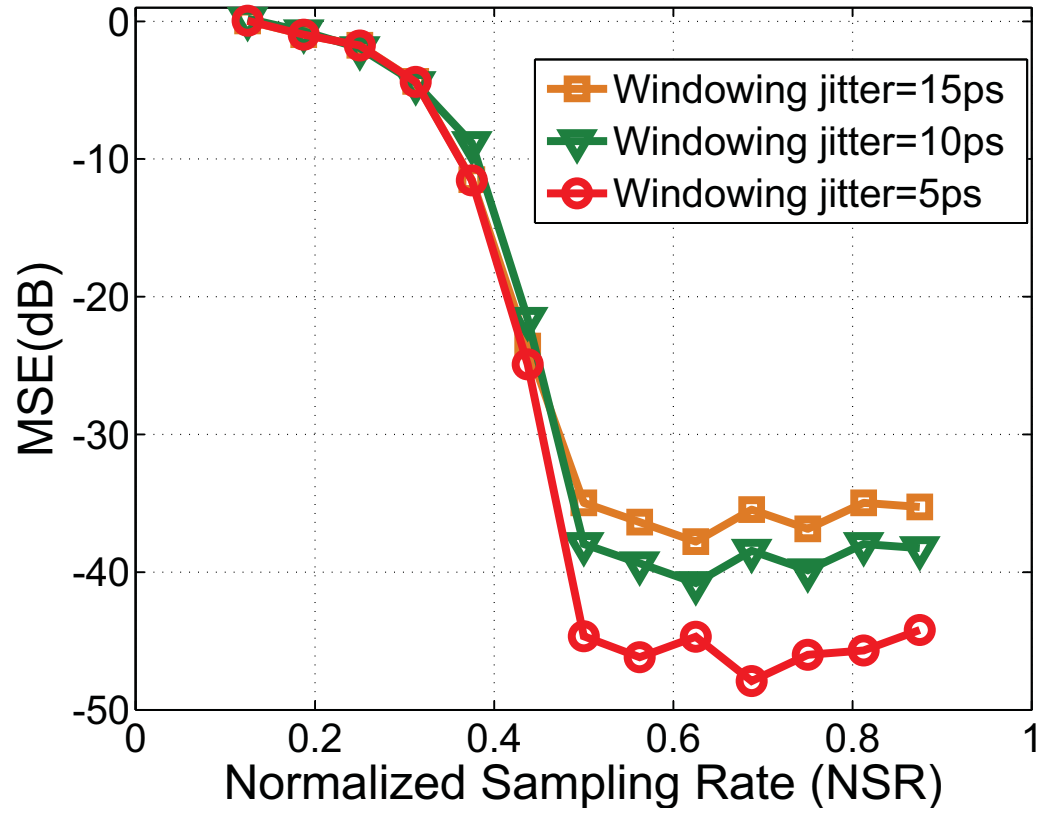


Fig. 29. MSE of the reconstructed signal versus the normalized sampling rate when there exists timing uncertainty on the edges of the sliding window.

B. Background Calibration of Circuit Nonidealities

As shown in section A, the quality of the reconstructed signal during the compressive AIC procedure is greatly impacted by the accuracy of analog circuit components, because the circuit imperfections causes an offset on the reconstruction matrix as in equation (5.1). Among those nonideal factors, some can not be calibrated because of the random nature, such as the jitter and thermal noise. Fortunately, many other nonideal factors including the finite settling time, the gain and phase mismatches and so on can be calibrated. In this section, we propose an iterative background calibration algorithm based on LMS to compensate the offset of the reconstruction matrix, that is, to adjust \mathbf{V} such that it approximates $\tilde{\mathbf{V}}$.

The block diagram of the proposed calibration scheme is illustrated in Fig. 30. Specifically, the multi-carrier signal is modulated by a known training data \mathbf{a} , i.e., $\mathbf{r} = \Psi\mathbf{a}$, then \mathbf{r} is sent to the PSCS AIC system where the samples at the transform domain $\mathbf{y} = \tilde{\mathbf{V}}\mathbf{a}$ are collected. At the same time, \mathbf{y}_{est} , an estimation of \mathbf{y} is calculated based on the current reconstruction matrix. The error between the estimated sampling values and the actual sampling values is determined and fed back to update the reconstruction matrix. For convenience and clarity, this calibration scheme is called *Forward Calibration*. The pseudo code for the proposed calibration algorithm is given below, where μ is the step size for the updating [80].

Fig. 31 plots the MSE of the reconstructed signal with a NSR of 0.625 and a finite settling time of 30ps when the background calibration is active. The rest of the simulation setup is the same as Fig. 28. As shown in the figure, the MSE starts from -20dB and

Algorithm 2 Background Calibration

```

1: initialization:  $\mathbf{V}_0 = \mathbf{V}$ ;
2: for  $q = 0 : Q - 1$  do
3:    $\mathbf{y}_{est} = \mathbf{V}_q \mathbf{a}$ ;
4:    $\mathbf{e} = \mathbf{y} - \mathbf{y}_{est}$ ;
5:    $\mathbf{V}_{q+1} = \mathbf{V}_q + \mu \cdot \mathbf{e} \cdot \mathbf{a}^H$ ;
6: end for
7: Output:  $\mathbf{V} = \mathbf{V}_Q$ ;

```

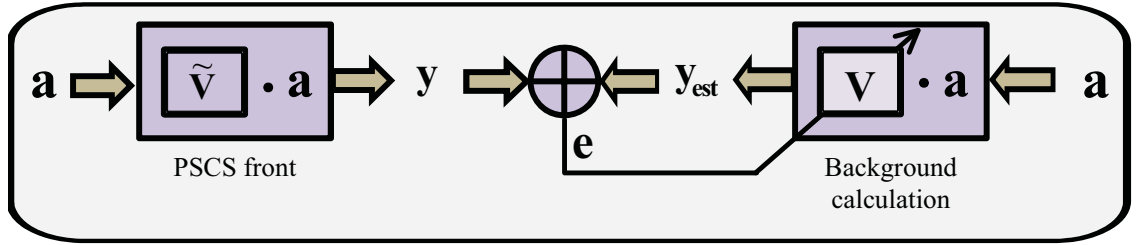


Fig. 30. Illustration of the LMS based background forward calibration.

gradually decrease until below -200dB and then remain stable, which means that the signal can be reconstructed perfectly even with some circuit imperfection once the calibration algorithm converges. Therefore, the proposed background calibration algorithm successfully compensates for the offset of the reconstruction matrix. Note that when the training signal is *K-sparse*, the algorithm converges relatively slowly. This is because only K out of S columns of the reconstruction matrix are effectively updated at each iteration. Instead, if we intentionally make the input signal less sparse during the training stage, the convergence procedure can be accelerated. However, in practice, using a particular training signal

is not only determined by the type of the available training signals, but also constrained by the input dynamic range of the practical AIC systems.

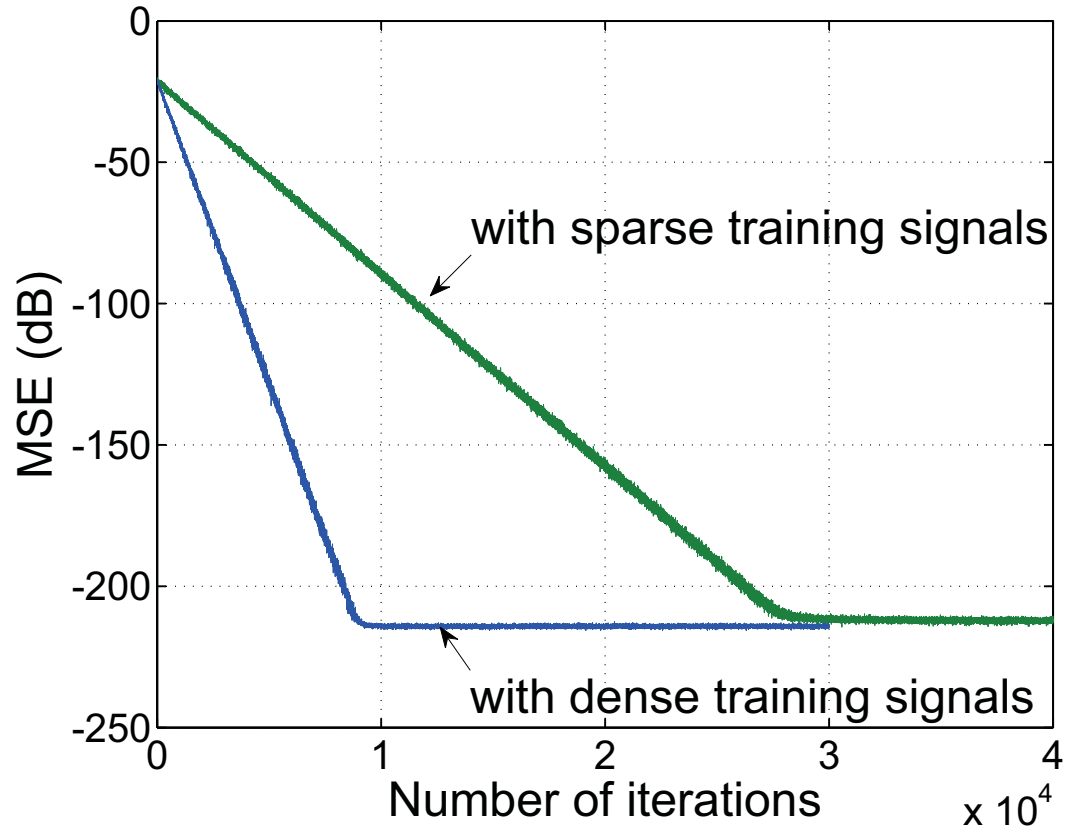


Fig. 31. MSE of the reconstructed signal versus the normalized sampling rate when the random PN sequences have finite settling time and the background calibration is active.

CHAPTER VI

LOW-SPEED OFF-THE-SHELF COMPONENT PROTOTYPE*

A. System Specification

As a proof of concept, we built a low-speed prototype using off-the-shelf components, where the input signal is a real BPSK modulated multi-carrier signal with 4 active subcarriers and the active subcarriers hop over the frequencies $(i * 2 - 1)\text{KHz}$ ($i = 1, 2, \dots, 100$) every $500\mu\text{s}$. Considering the system complexity, we employed 4 parallel paths for the prototype. Simulation shows that the signal can be reconstructed perfectly when each parallel path produces 16 samples every $500\mu\text{s}$, which corresponds to 32% of the Nyquist sampling rate. The main system parameters are summarized in Table III.

Table III. Testing results of the prototype

BW	Δf	$T = \frac{1}{\Delta f}$	M	N	$\Delta t = \frac{T}{M}$	$f_s = \frac{1}{\Delta t}$	T_c	T_{OVR}	OVR
200kHz	2kHz	$500\mu\text{s}$	16	4	$31.25\mu\text{s}$	32kHz	$36.5\mu\text{s}$	$5.6\mu\text{s}$	15.43%

B. Overall Configuration

The overall configuration of the prototype is shown in Fig. 32, where the digital part is responsible for generating the input sparse signal, the triggering signal, the pseudo-random

*Part of this chapter is reprinted with permission from "Mixed-signal parallel compressive spectrum sensing for cognitive radios" by Z. Yu, X. Chen, S. Hoyos, B. M. Sadler, J. Gong and C. Qian, International Journal of Digital Multimedia Broadcasting, vol. 2010, article ID 730509, 10 pages, Mar. 2010. doi:10.1155/2010/730509. ©Zhuizhuan Yu.

basis and the clock. The analog part is used to realize the random basis projection that is essential for the signal reconstruction. The built-in ADC in the oscilloscope is used to collect the sampled data. Then, the collected data is sent to a PC and processed via Matlab code to reconstruct the signal. In the following sections, each building block will be introduced in detail.

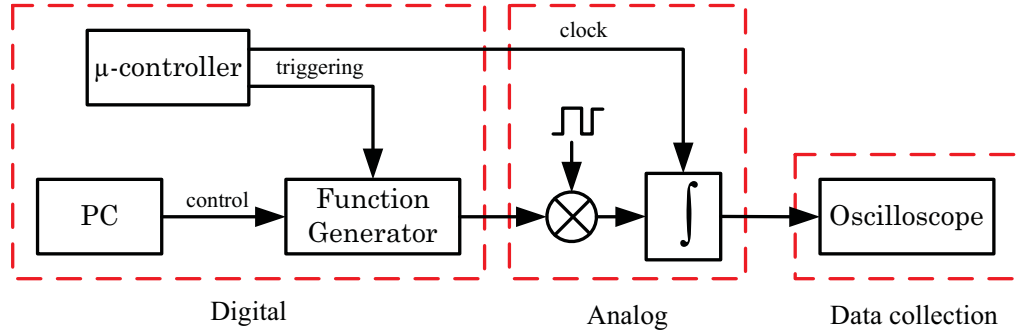


Fig. 32. Overall configuration of the prototype using off-the-shelf components.

C. Multi-carrier Signal Generator

An Agilent 33120A arbitrary waveform generator is used to generate the input multi-tone sparse signal. Specifically, the multi-tone signal is programmed in the PC first and then downloaded into the wave generator. The output port of the generator is triggered by the micro-controller in order to synchronize with the integrator clock that is also generated by the micro controller.

D. Mixers and Integrators

Fig. 33 depicts the macro model of one path in the prototype. As shown, the input signal is first translated into current by the OTA and then mixed with the pseudo random signal. After mixing, the signal is integrated in the sampling capacitor with a timing window. In the sampling circuit the interleaving capacitor is employed. Finally the ADC yields digital output data. The OTA we employed is a TIOPA861 with G_m of 116mS and all the switches are implemented with transmission gate CD4066BCN.

The pseudo random number (PN) is -1 or 1, whose spectrum is a sinc function. The main lobe is from 0 to $1/T_{clk}$, where T_{clk} is the clock period of the PN generator. In our test bed T_{clk} is $1\mu s$. After the mixing, the signal is shaped by the embedded low pass filter provided by the integration window. The frequency response of the LPF is a sinc function. The main lobe spans 0 to $1/T_c$, where T_c is the integration time. In our test bed $1/T_c$ is roughly 30 KHz.

The random projection of the input analog signals is realized with mixers and integrators. Fig. 34 gives the circuit implementation of one parallel path and Fig. 35 gives the corresponding pin connection relationship for the integrator. The transconductance amplifier (G_m stage) translates the signal voltage into current, which can be easily mixed with the pseudo-random numbers (1/-1) by the following passive switch mixer. After mixing, the signal is integrated with an overlapping window and then sampled by the ADC in each path. The circuit is built up differentially so that the system is more robust to supply noise, clock jitter and even-order harmonics. The double balanced passive mixer does not introduce significant noise and distortions.

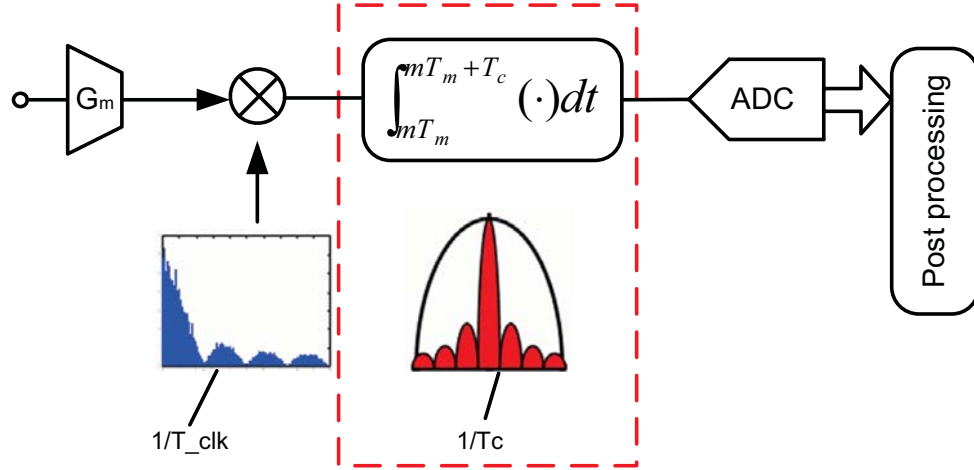


Fig. 33. Macro model of one parallel path.

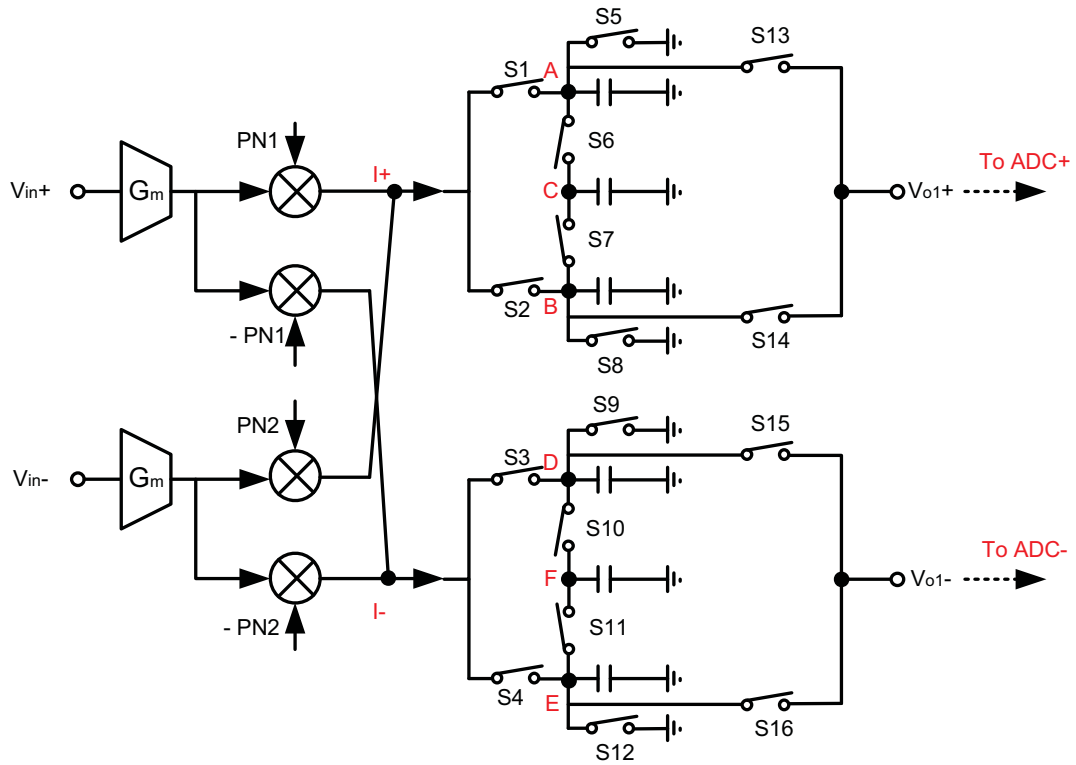


Fig. 34. Circuit implementation of one parallel path.

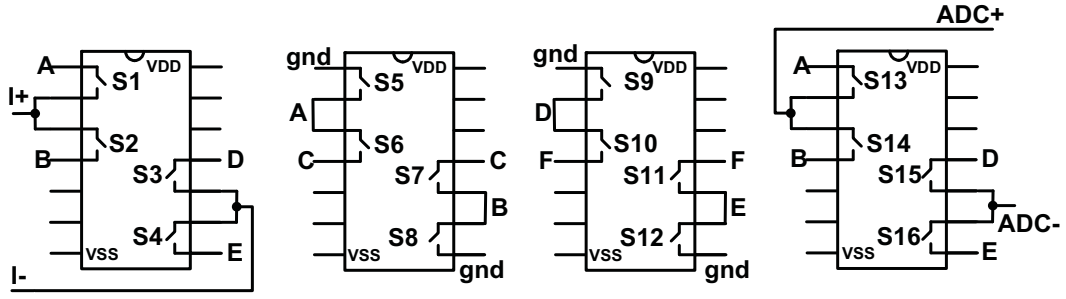


Fig. 35. Pin connection of the integrator in one parallel path.

At each path, the mixer consists of transmission-gate switches controlled by PN sequences. The PN sequence is implemented with a linear feedback shift register (LFSR). In our prototype, the clock frequency is chosen to be 1MHz, which is higher than the Nyquist sampling rate. Because the PN sequences are repeated every $500\mu s$ and there are 4 parallel paths, we need 4 independent PN sequences with a length of 500. An 11-bit LFSR is used to generate a PN sequence with a length of 2047 and then divided into 4 segments. As a check, the autocorrelation function of the PN sequences are calculated to make sure that the four PN sequences are incoherent. The generation of PN sequences and the system clocks is controlled by the micro-controller. Fig. 36 gives an example of generated clocks, where

An overlapped time-interleaving charge-domain sampling integrator is chosen for the analog path. The integrator schematic is shown in Fig. 37. ϕ_1 and $\bar{\phi}_1$ are two integration switches for the left and right branches, respectively. ϕ_{o1} and ϕ_{o2} are readout switches; ϕ_{r1} and ϕ_{r2} are reset switches. By utilizing these six switches combined with the two integration capacitors C_1 and C_2 , according to the clock diagram shown in Fig. 38, we can realize a conventional time-interleaving charge-domain integrator without overlapping. Time interleaving means when the left branch is integrating while the right is reading out, and vice versa. By doing this, a complete sampling of the signal is achieved. In addition

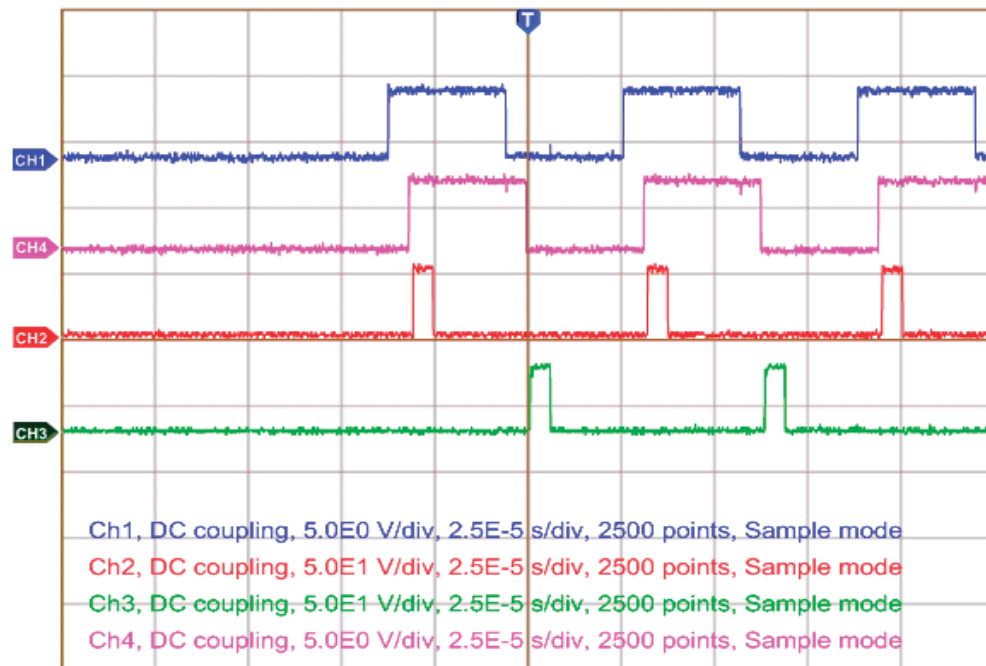


Fig. 36. Example of clock signals.

to time interleaving, a small overlapping time is introduced by one more capacitor C_{ov} and two control switches ϕ_2 and $\bar{\phi}_2$.

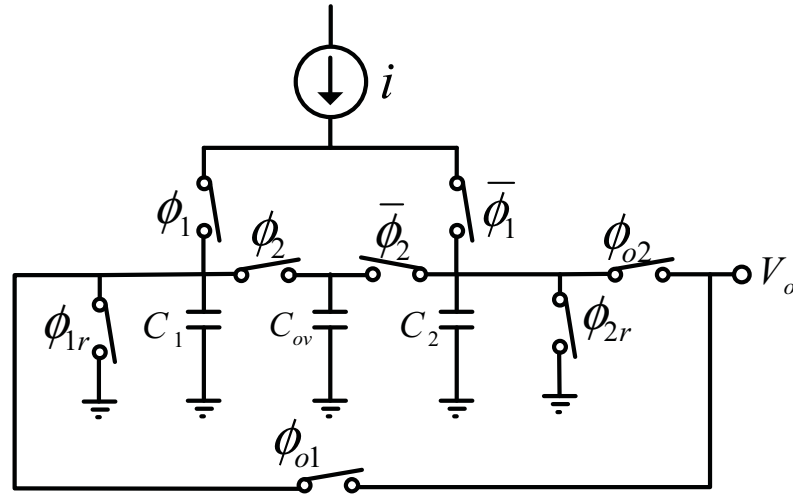


Fig. 37. Schematic of the integrator with overlapping.

As shown in Fig. 38, phase 1 and phase 3 are to realize the overlapping through charge redistribution and sharing, and phase 2 and phase 4 are the readout times for the right and the left branches, respectively. During phase 1, the input current charges both C_1 and C_{ov} while C_2 is idle. Since all capacitors have the same value, the current splits equally by half into both capacitors. In the succeeding phase, C_{ov} is switch-connected to C_2 and readout together, so that C_{ov} is integrating for the right branch during phase 1. Equivalently, as shown in the timing window diagram, the window splits by half during the overlapping time. The key point here is that both branches are integrating and no data is readout during window overlapping times.

Note that the overlapping windowing realized using the circuit in Fig. 37 is somewhat

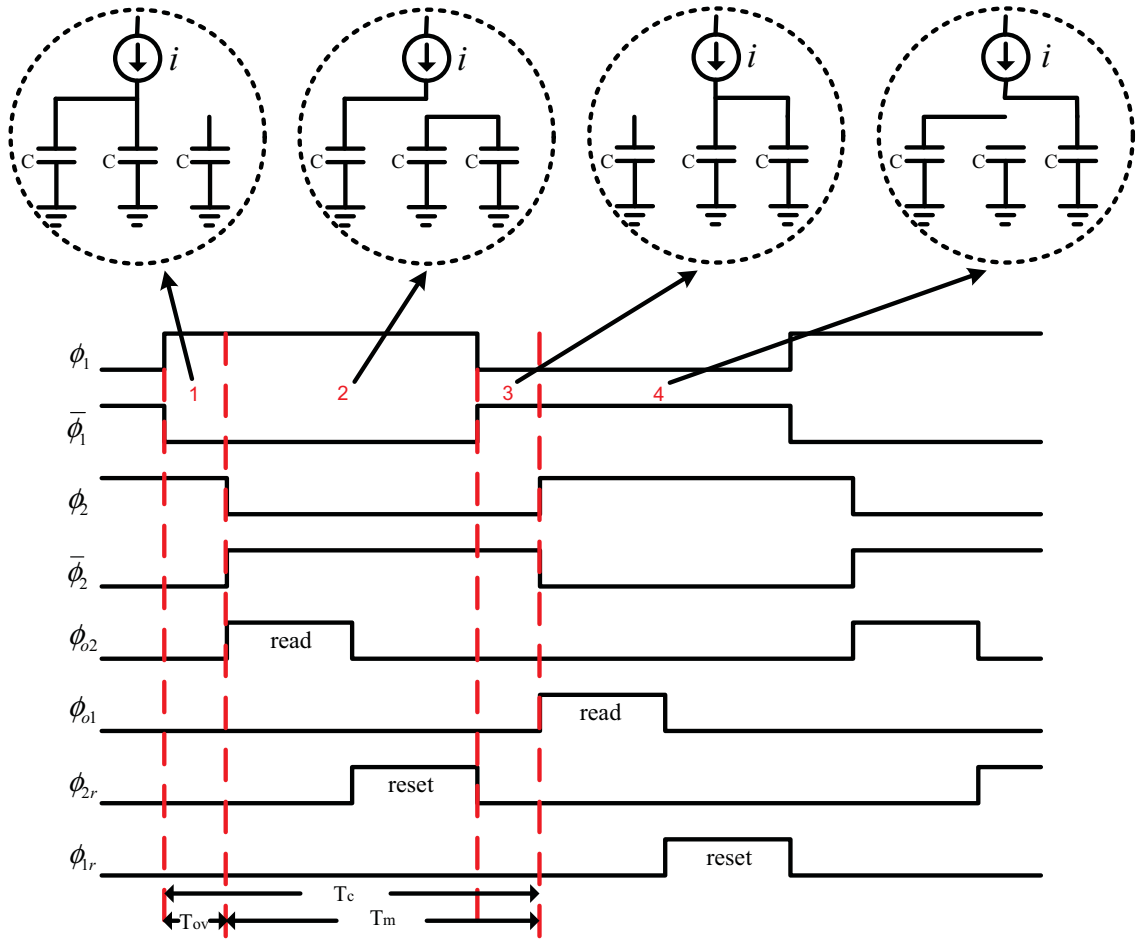


Fig. 38. Operation of the interleaved overlapping windowed integration and the related clocks.

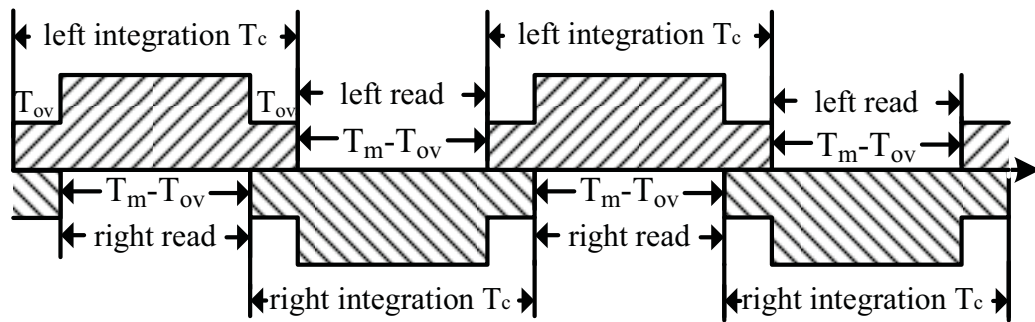


Fig. 39. Illustration of the overlapping windowing in the prototype.

different from the overlapping windowing in Fig. 9, as shown in Fig. 39. In Fig. 9, the charges accumulated during the current window period includes 100% of the charges from the last T_{ov} seconds of the previous windowing period but no charges from the next windowing period. In Fig. 37, the charges accumulated during the current windowing period includes 50% of the charges from both the last T_{ov} seconds of the previous windowing period and the first T_{ov} seconds of the next windowing period, which is more realistic from the implementation perspective.

E. Data Collection and Signal Reconstruction

For simplicity, we use the inherent ADC of the oscilloscope (Tectronix TDS 3054 500MHz, 5Gs/s) to sample the output of the integrators. The sampled data is transferred to the PC via the GBIP port. With the collected samples, the signal is reconstructed using the OMP as described in Chapter III.

F. Dealing with Circuit Nonidealities

While implementing the prototype, it is inevitable that the system has some non-idealities such as the delay caused by each component, the gain variation, the mismatch among parallel paths and so on.

In Chapter V, we discussed the impact of some circuit imperfections, such as the finite settling time of the PN sequences, and the timing uncertainty, and a background calibration algorithm based on LMS was proposed to compensate for the error due to these circuit nonideal factors. Because of the complexity of the background calibration, here we use a

more simple approach based on direct training to deal with the circuit nonidealities. The direct training approach is illustrated in Fig. 40. During the training stage, we inject a single-tone signal one at a time to the prototype and collect the samples from the 4 parallel paths, so that these samples will fill one column of the reconstruction matrix $\tilde{\mathbf{V}}$. After sending 100 single-tone signals, we obtain a complete matrix which will be used for signal reconstruction.

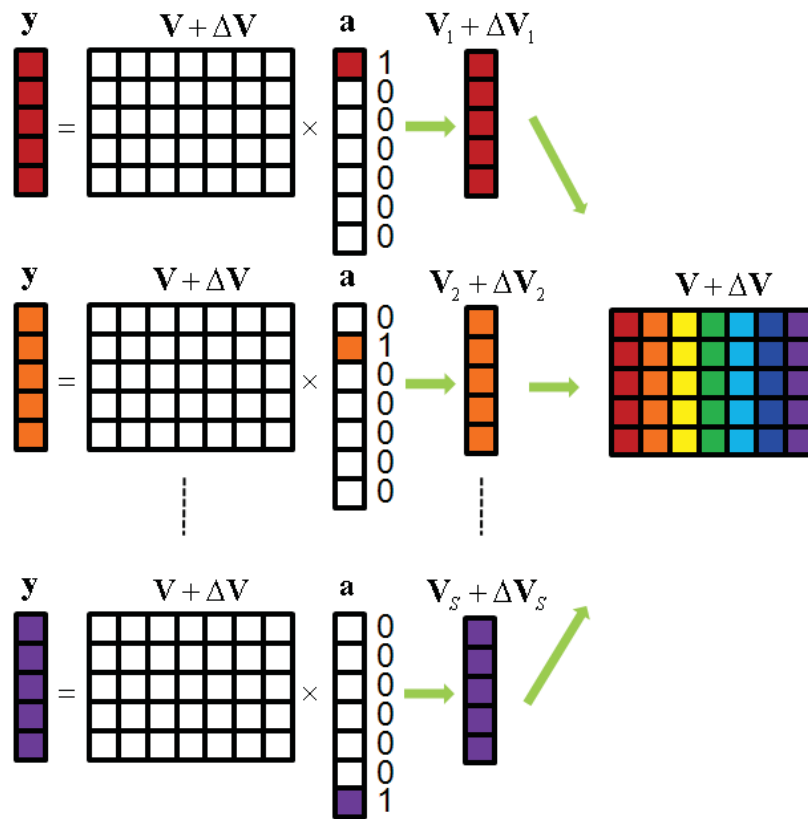


Fig. 40. Illustration of the direct training approach to deal with the circuit imperfections.

This pilot-based method is based on the assumption that the system is linear and time-

invariant. Fortunately, our circuit level design ensures that the input signal swing is within the linear range of the system, and the microcontroller ensures that the system has the same initial condition for every run. Therefore, the linear time-variant assumption is reasonable. Implementing the background calibration for circuit imperfection compensation is part of our future work.

G. Testing Results

The testing setup for the prototype is shown in Fig. 41. A photo of the analog and the control parts is shown in Fig. 42. An example of the integrator output waveform is shown in Fig. 43. A series of experiments are done to test the functionality of the system. Table IV summarizes the testing results, where $+$ and $-$ stands for the polarity of the BPSK modulation. Note that we scale the amplitude of each sub-carrier according to the number of tones such that the amplitude of the multi-carrier signal is within the dynamic range of the system. From the testing results, the prototype achieves the design specification.

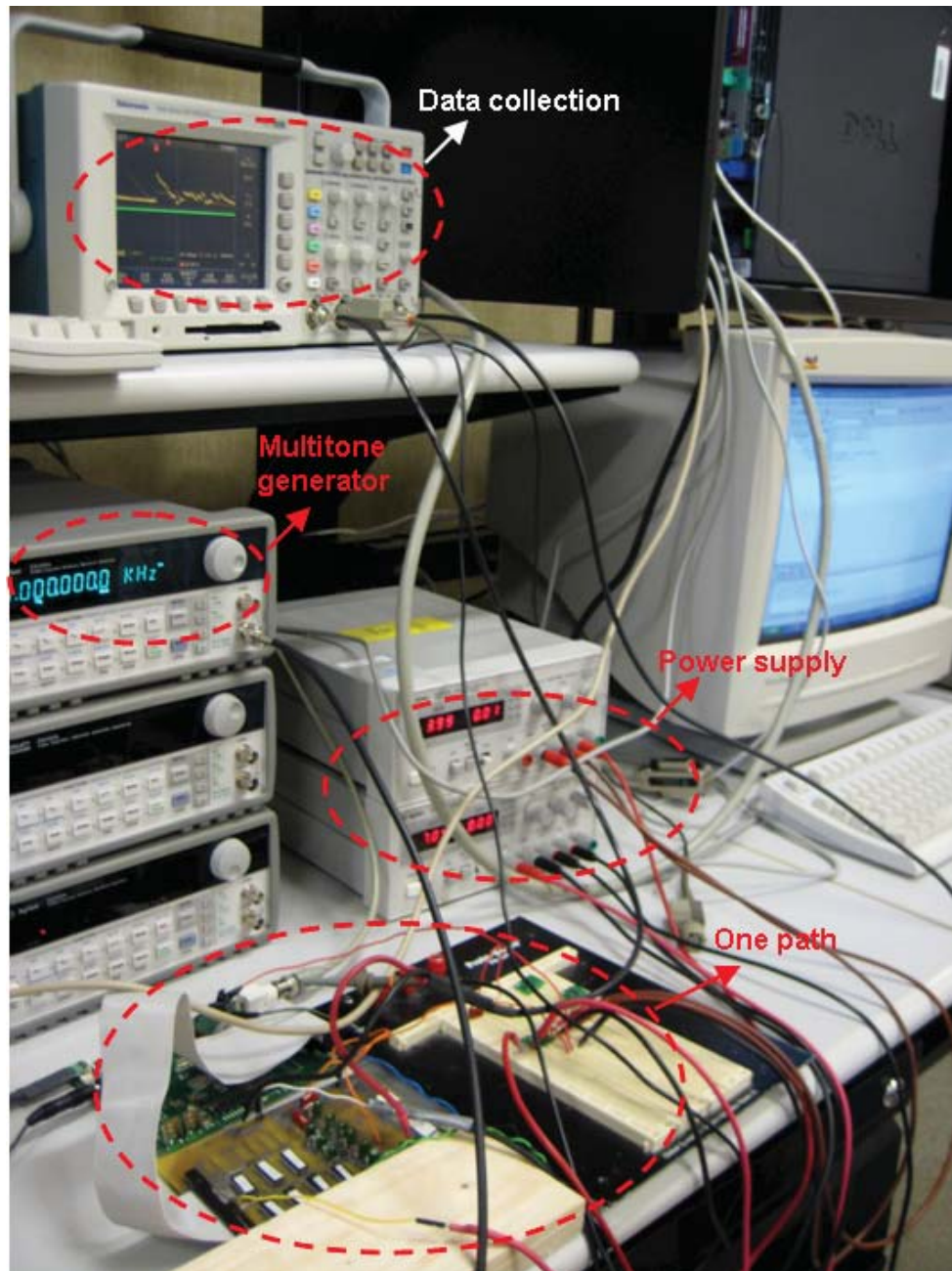


Fig. 41. Testing setup of the prototype.

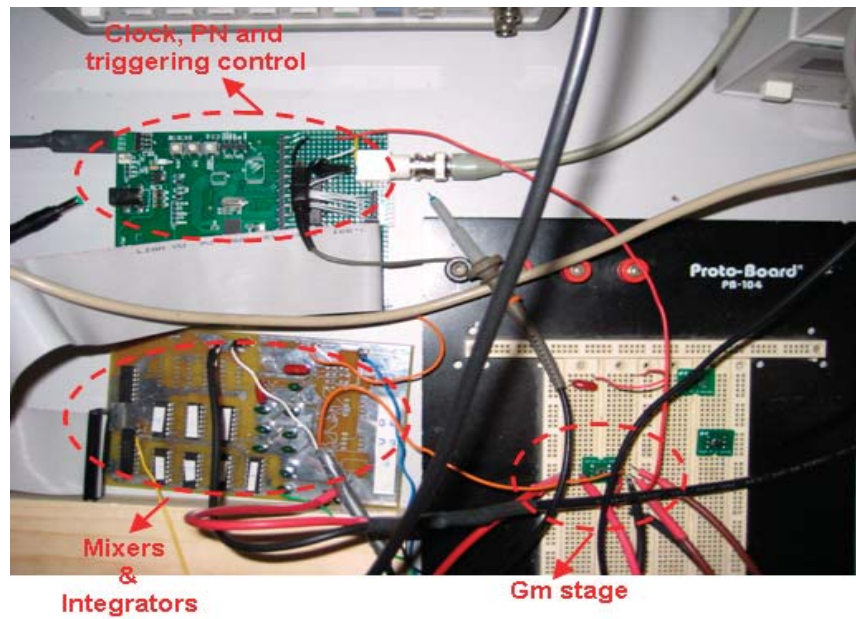


Fig. 42. Photo of the analog and the control part of the prototype.

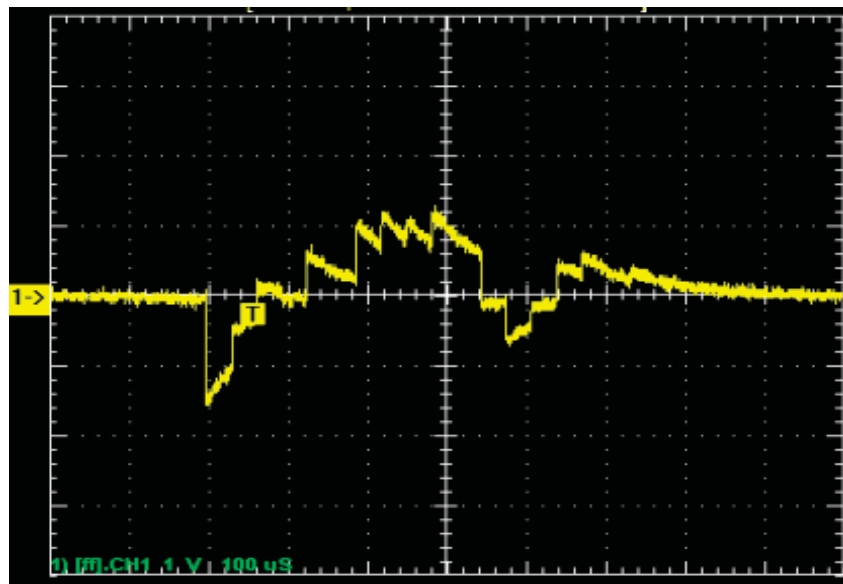


Fig. 43. Example of the integrator output waveform.

Table IV. Testing results of the prototype.

Subcarrier's amplitude (mV)	Subcarrier frequencies of the input testing signal (kHz)	Subcarrier frequencies of the reconstructed signal (kHz)
0.3	[+61, +121]	[+61, +121]
0.3	[+41, +131]	[+41, +131]
0.3	[+61, -131]	[+61, -131]
0.3	[-51, +63, +111]	[-51, +63, +111]
0.2	[+71, -85, +91, -101]	[+71, -85, +91, -101]

CHAPTER VII

HIGH-FREQUENCY INTEGRATED PROTOTYPE[†]

A. Overview

As a further step from building the low-speed prototype with off-the-shelf components, a high frequency prototype of the PSCS system was taped out with the IBM90nm CMOS technology. Recall that in Fig. 11, we showed that for a signal with a sparsity of 4%, the minimum compressive sampling rate for perfect signal reconstruction is about 26% of the Nyquist rate. The designed PSCS prototype system is targeted to sample wideband signals of a sparsity of 4% over 10 MHz \sim 1.5 GHz bandwidth with an overall sub-Nyquist sampling rate of 880MHz, although the actual built system is adaptable to varying levels of sparsity. The whole PSCS front-end consists of 8 parallel paths (equivalently 4 complex I-Q paths) and each path works at a sampling rate of 110MHz. The input signal is a frequency-domain sparse multi-carrier signal as modeled in equation (3.3) and the signal power is assumed to be -20 dBm referred to 50 ohm. The SNDR of the reconstructed signal in our proposed system is targeted at 44 dB (7 bits). The error energy individually induced

[†] Part of this chapter is reprinted with permission from "A Sub-Nyquist Rate Sampling Receiver Exploiting Compressive Sensing" by X. Chen, Z. Yu, S. Hoyos, B. M. Sadler and J. Silva-Martinez, IEEE Trans. on Circuits and Systems I: Regular Papers, vol. 58, Issue 3, pp 507-520, Mar. 2010. ©[2010] IEEE. This material is posted here with permission of the IEEE. Such permission of the IEEE does not in any way imply IEEE endorsement of any of Texas A&M University's products or services. Internal or personal use of this material is permitted. However, permission to reprint/republish this material for advertising or promotional purposes or for creating new collective works for resale or redistribution must be obtained from the IEEE by writing to pubs-permissions@ieee.org. By choosing to view this material, you agree to all provisions of the copyright laws protecting it.

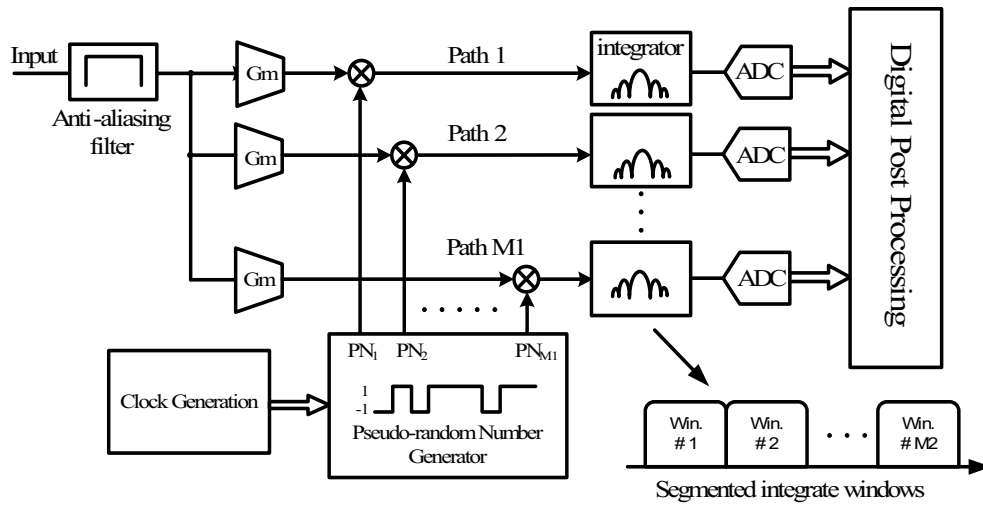


Fig. 44. Circuit implementation of the PSCS front-end.

by jitter, circuit noise, distortion and the quantization noise is designed to be less than -50 dB as referred to the signal power in order to achieve an overall SNDR of 44 dB.

B. Circuit Level Implementation Approach

1. PSCS Front-end Circuit Architecture

The circuit block diagram of the current mode parallel-path front-end is shown in Fig. 44. The current mode architecture has the benefit of allowing convenient design of mixers and reconfigurable integrators. It is assumed that an out-of-chip high-order anti-aliasing filter is present at the input of the receiver and selects the signal bandwidth 10 MHz 1.5 GHz. The input wideband signal feeds the low noise amplifier followed by 4 identical I-Q paths, as shown in Fig. 45. The low noise amplifier should be able to provide excellent input impedance matching over the entire signal bandwidth so that the signal integrity is not degraded. The circuit is built up differentially so that the system is more

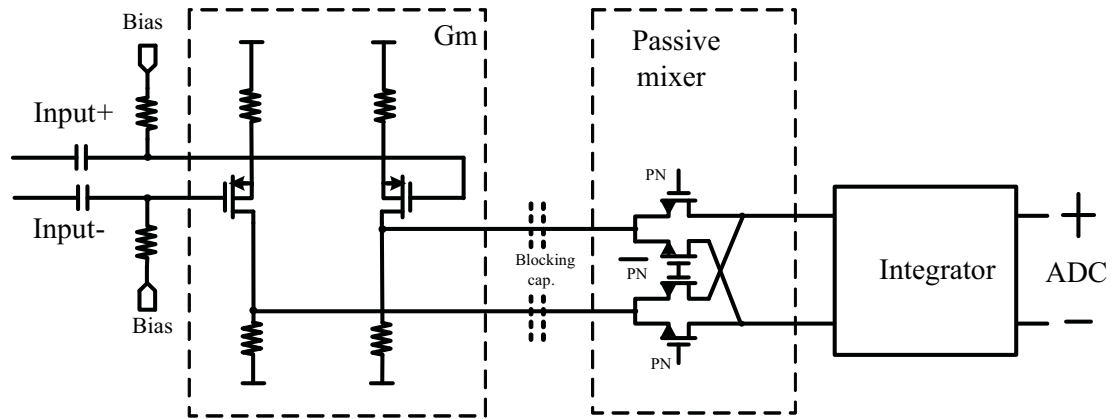


Fig. 45. Detailed circuitry of one complex (I-Q) path.

robust to supply noise, clock jitter and even-order harmonics. The double balanced passive mixer does not introduce too much noise and distortions. In each path the transconductance amplifier translates the signal voltage into current, which can be easily mixed with the Pseudo-random Numbers (1/-1) by the following passive switch mixer. The mixer output current is integrated over segmented integration windows. The integrators' outputs are then digitized and post-processed digitally. The Pseudo-random Numbers (PN) are generated and controlled by the digital logic circuit, and an applicable PN generator can be found in [81]. The PN generator operates at the Nyquist rate. A screen shot of the PN sequence obtained through Cadence is shown in Fig. 46.

The integrator consists of two time-interleaved branches that provide successive integration windows. A simplified schematic of the integrator is shown in Fig. 47. The capacitors are first reset, and then the mixer output current is injected into one of the capacitors CS during the integration time T_c . After that the charge is transfer to the ADC. The

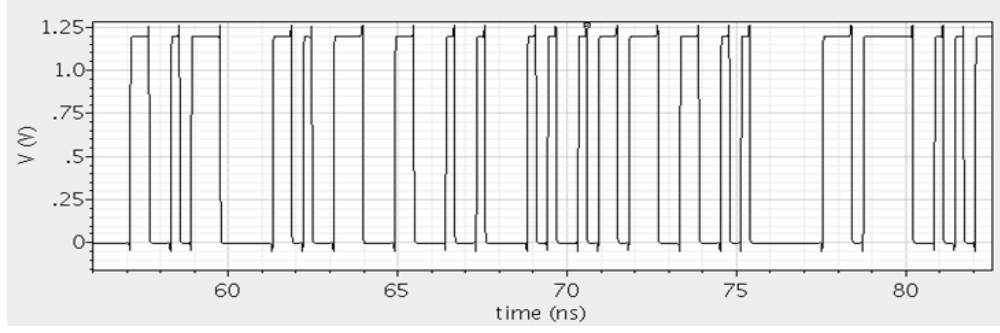


Fig. 46. An example of PN sequences.

integrator also serves as the sample and hold (S&H) circuit before the ADC. The sampling rate is reconfigurable, depending on the frequency of the controlling clocking scheme and is set according to the signal sparsity. It can also operate up to Nyquist rate if the signal does not exhibit enough sparsity to be processed using the CS theory. The sinc type frequency response of the windowed integrator is shown in Fig. 48, where T_c is the duration of a single segmented integration time window. The -3 dB bandwidth of the transfer function is $1/2T_c$, which is also controlled by the clock frequency.

2. Parallel Path ADCs

Each path employs a low speed ADC that samples the randomized signal at the output of the integrator. The sampling rate is around 110MS/s and the effective number of bits (ENOB) of the ADC needs to be 8 bits to achieve 50dB SNR. Pipeline ADCs or SAR ADCs can meet this specification with low power consumption. In [82], a pipeline ADC achieves 7.9 ENOB and 50MS/s with power consumption of 1.44mW. In [83], a SAR ADC achieves 8.53 ENOB and 100MS/s sampling rate with power consumption of 1.46

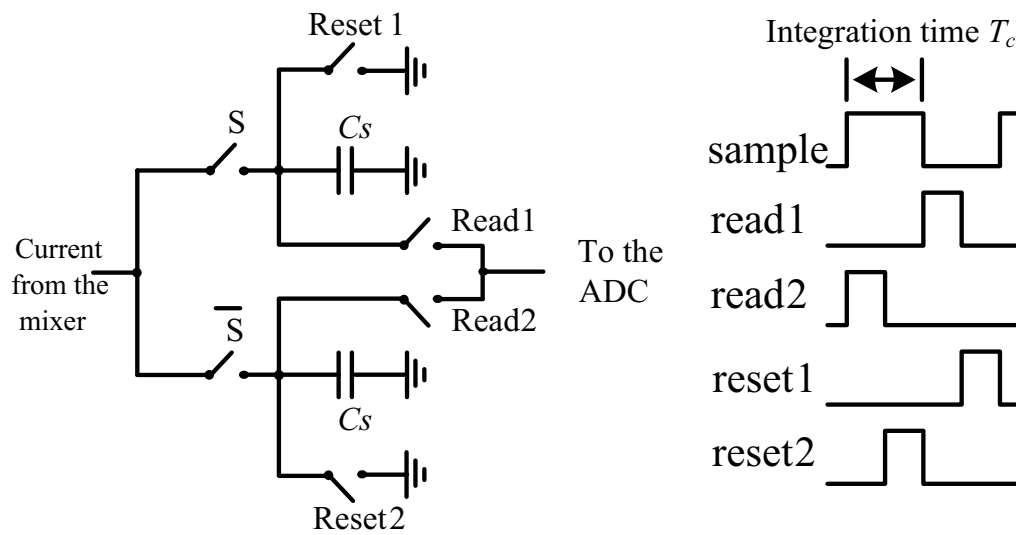


Fig. 47. Simplified schematic of the integrator.

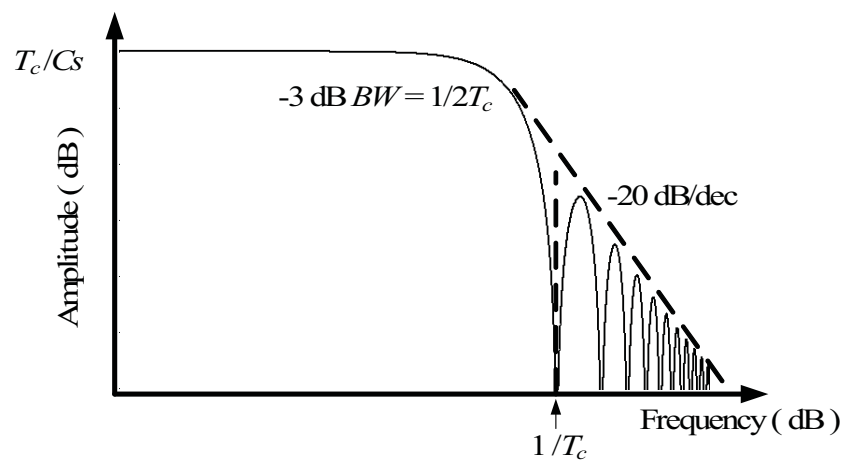


Fig. 48. Frequency response of the windowed integration.

mW. Performance, non-idealities, and the design procedure of traditional Nyquist ADCs have been extensively discussed in existing literature. Rather than designing an ADC, we estimate the power consumption of the system with ADCs incorporated based on the published state-of-the-art ADCs. According to the technology trend [21], [84], a 110MHz/8 ENOB ADC consumes approximately 3.5mW power. It is then expected that the 8 ADCs should consume an overall power around 28 mW.

C. Design Specification

The PSCS front-end circuit was designed in the IBM 90nm CMOS technology. Performance of key circuit blocks and the power consumption were estimated by post-layout simulations. Parasitic extractions and simulations were done with Calibre and Cadence Spectre. The outputs of the front-end are connected to buffers that drive the external ADCs' loading capacitance. The external ADCs' may be implemented on the PCB. In the simulations, a capacitor is inserted at the output of the integrator to emulate the ADCs' loading. The power consumption of the testing-purpose buffers is not included. System level design specs are listed in Table V.

For 50 ohms input impedance matching, the input noise power $V_{N,input}^2$ is equivalent to $-174dBm/Hz \times BW$, which corresponds to -82.24 dBm when integrated over a BW of 1.5 GHz. In the proposed prototype, the input signal power $V_{sig,input}^2$ is expected to be -20 dBm and the SNR at the input is around 62 dB. The noise figure of the front-end is 12 dB to achieve 50 dB output SNR. The front-end is around 20 dB to amplify the input signal up to the range of 0 dBm. Detailed analysis on the front-end signal gain, front-end

bandwidth, noise, distortion, and clock jitter can be found in [85].

Table V. Design specifications of the CS front-end.

Input Signal Bandwidth	10 MHz \sim 1.5 GHz
Number of Parallel Paths	8
Single Path sampling rate (4% sparsity)	110 Ms/s
Overall System Sampling rate	880 MS/s
SNDR with 0.5 ps jitter	44 dB
Max. signal gain at the front-end	around 20 dB
Fullscale input / output	-20 dBm / -2 dBm (referred to 50 ohms) 0.06 / 0.5Vpp

D. Power Consumption and Area

The power consumption of the proposed PSCS front-end is summarized in Table VI, with power of ADCs included, as estimated in Section B.2. The layout of a single path is shown in Fig. 49. The overall chip area for 8 paths is estimated to be $1000\mu m \times 1400\mu m$.

E. Figure of Merit

The proposed receiver can be compared to a stand alone 3 GS/s and 44 dB SNDR ADC. Such a high speed and medium resolution ADC can be implemented employing a time-interleaved ADC architecture. Some recently published high speed time-interleaved ADCs are listed in Table VII. A flash ADC [86] is also included in the table. The Figure

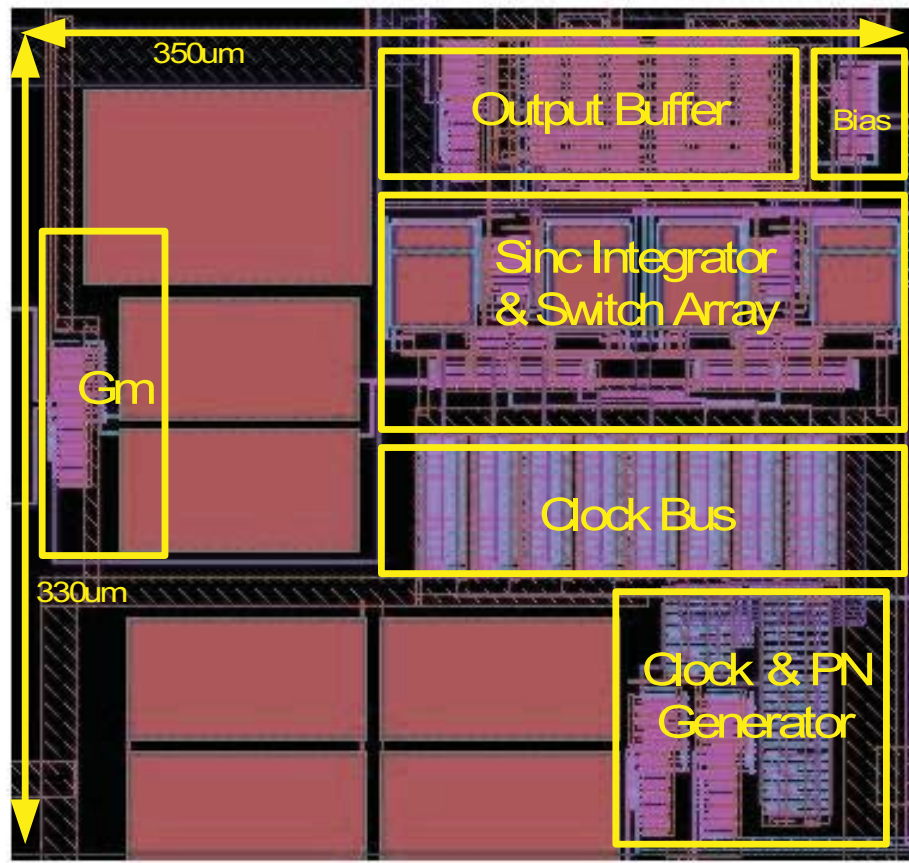


Fig. 49. Layout of a single path of the PSCS front-end in IBM 90 nm CMOS.

Table VI. Summary of the power consumption.

Power consumption @800MS/s	Gm stages	16mW
	Integrators	19.2mW
	Clocks	57.6mW
	PN sequences	
	ADCs	28mW
	Overall	120.8mW

F. Reconfigurability

The sampling rate of the integrator and the sampler only depend on the clocking scheme, leading to a flexible reconfigurability that enables the system to accommodate input signals with different sparsity levels. Although the system designed in section VI targets a signal sparsity of around 4%, by over-designing the OTAs and ADCs, the sampling rate of the system can be increased up to the Nyquist rate to sample non-sparse signals. When an input signal exhibits a high degree of sparsity, the required system sampling rate is low and signals are readily reconstructed with a CS algorithm. When the signal sparsity is 25% or larger, the required sampling rate approximates the Nyquist rate and the Least Square (LS) algorithm may be used to reconstruct the signal [63]. The LS algorithm is able to reconstruct signals with arbitrary sparsity when the system works at Nyquist rate. The OTA needs a GBW of 600MHz to settle within 7 bits resolution. Furthermore, the sampling rate of the following ADCs needs to be tunable up to 380Ms/s.

G. Test Results

The evaluation board for the fabricated front-end is shown in Fig. 50. The on chip system contains one single path including the Gm stage, the differential mixer, the active integrator, the sampling clock generator and the PN generators. Some auxiliary circuit blocks such as the biasing current generator, the clock buffers and the output testing buffers are also included. The complete 8 paths CS system may be implemented on a single print circuit board incorporated with 8 individual fabricated chips. On the PCB, RF transformers cx2156 with bandwidth 2.3MHz 2700MHz turn the single-ended arbitrary input signal as

well as the clock signals into differential signals that enters the single path chip. Common mode noises and the mismatches between the board GND and the chip GND are rejected. Biasing voltages and currents are controlled by potentiometers.

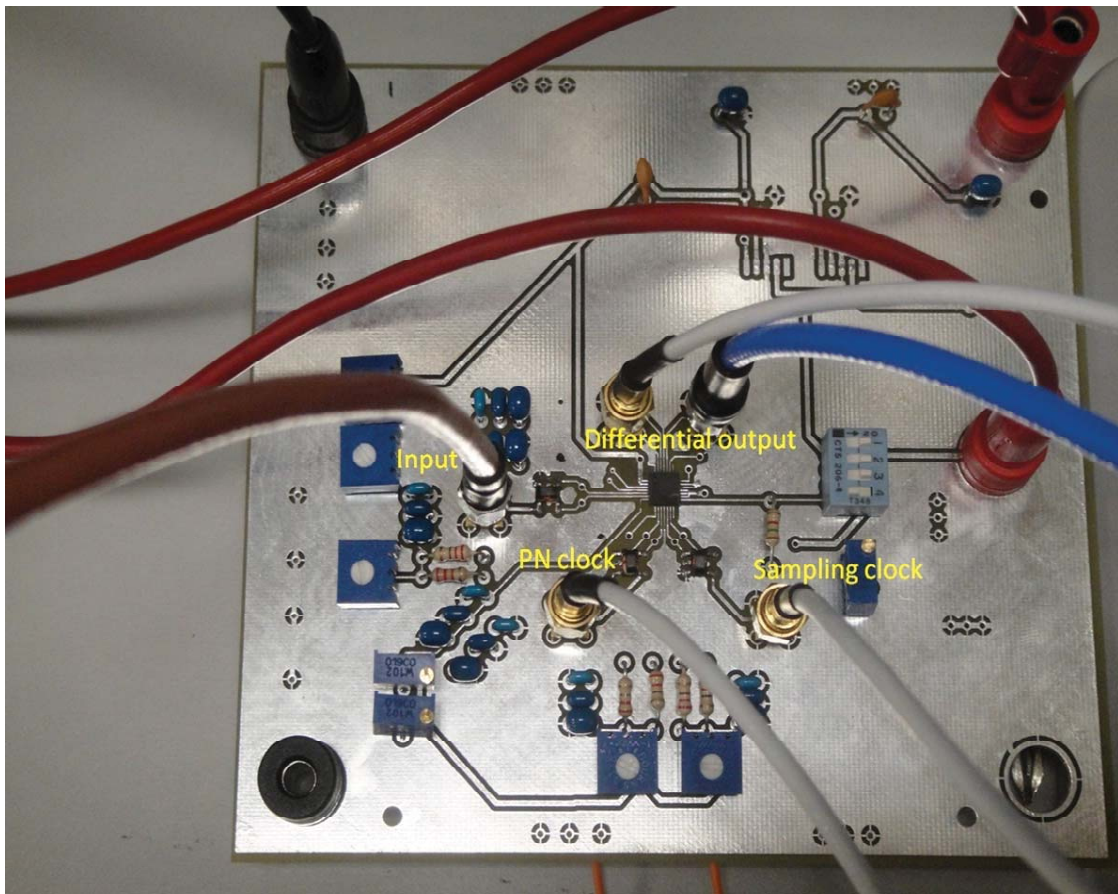


Fig. 50. Evaluation board of the high-frequency PSCS front-end prototype test.

The diagram of the test bench is given in Fig. 51 and a photo of the test bench is shown in Fig. 52. In the test setup, the Agilent N8241A Arbitrary Waveform Generator is responsible for generating the wideband multi-carrier signal and providing the clocks

for the PN generators and the sampling circuits. The differential output of the chip is monitored by the Agilent DSA91304A Oscilloscope with the 1169A differential probe. The inherent ADCs of the oscilloscope is also used to digitize the sampled data, which are post-processed at the host PC to reconstruct the signal. In order to synchronizing the sampling, PN generators and the data capturing at the oscilloscope, a trigger signal is provided by the arbitrary waveform generator and used to synchronize and phase lock the clocks at the chip and the data capture at the oscilloscope.

Note that based on the design specification in Section C, the system is originally designed for accommodating wide band input signal from $10\text{MHz} \sim 1.5\text{GHz}$ and the PN clock needs to run at 3GHz . However, the best waveform generator in the lab is only able to generate signals up to 1.25GHz , so in the actual testing the signal bandwidth can only be 0.625MHz . In reality, the arbitrary wave generator, which employs a DAC, needs to apply a low pass filter at its output in order to remove energy at frequencies higher than 625MHz . This low pas filter has finite roll-offs so can not clip the edge of the bandwidth sharply at 625MHz , which further limits the available generated bandwidth. Therefore, we adjust the system parameters for the testing accordingly, as shown in Table VIII.

Fig. 53 gives an example of the differential output of the front-end. As mentioned in Section B, the integrator consists of two time-interleaved branches that provide successive integration windows. When one branch is integrating, the other branch is reading and then resetting after the data is read out, as illustrated in Fig. 54.

The approach of Direct Training, as introduced in Chapter VI, is used to get an initial estimation of the reconstruction matrix. A series of tests were done to measure the per-

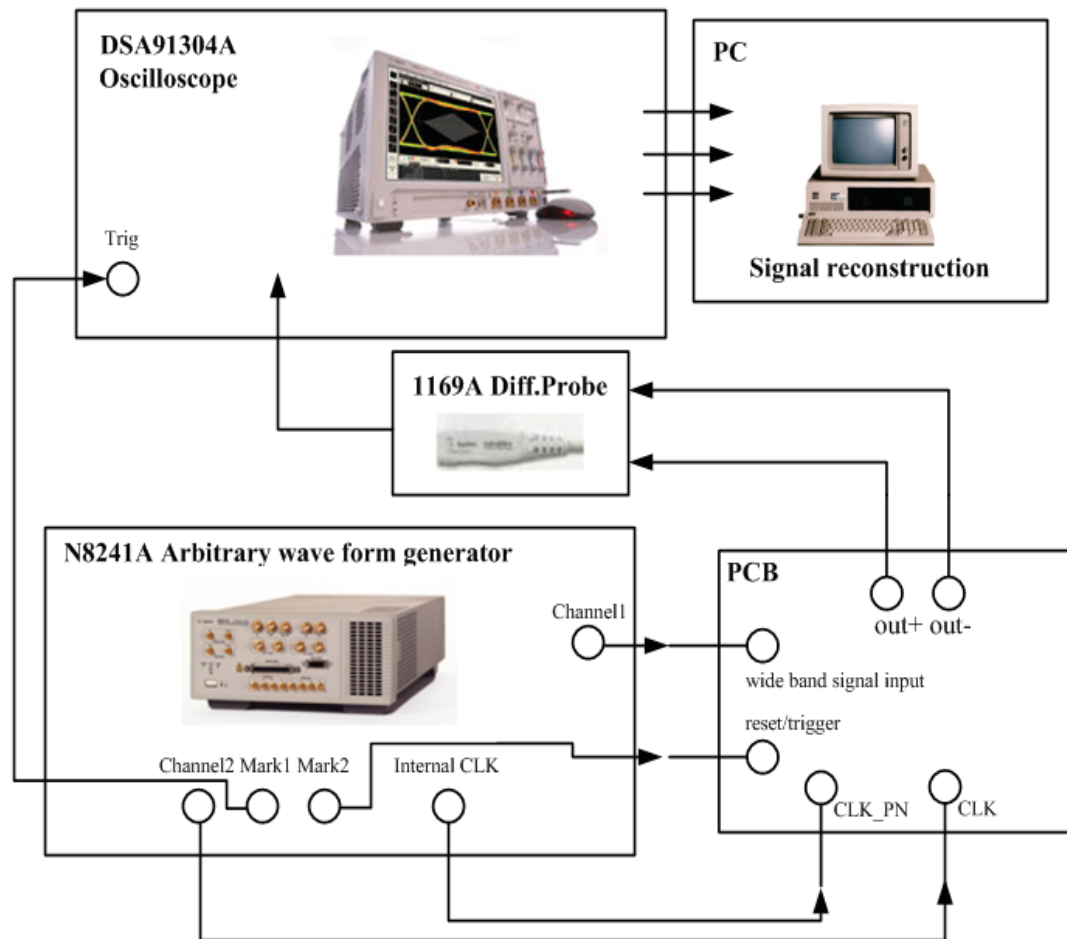


Fig. 51. Diagram of the test bench.

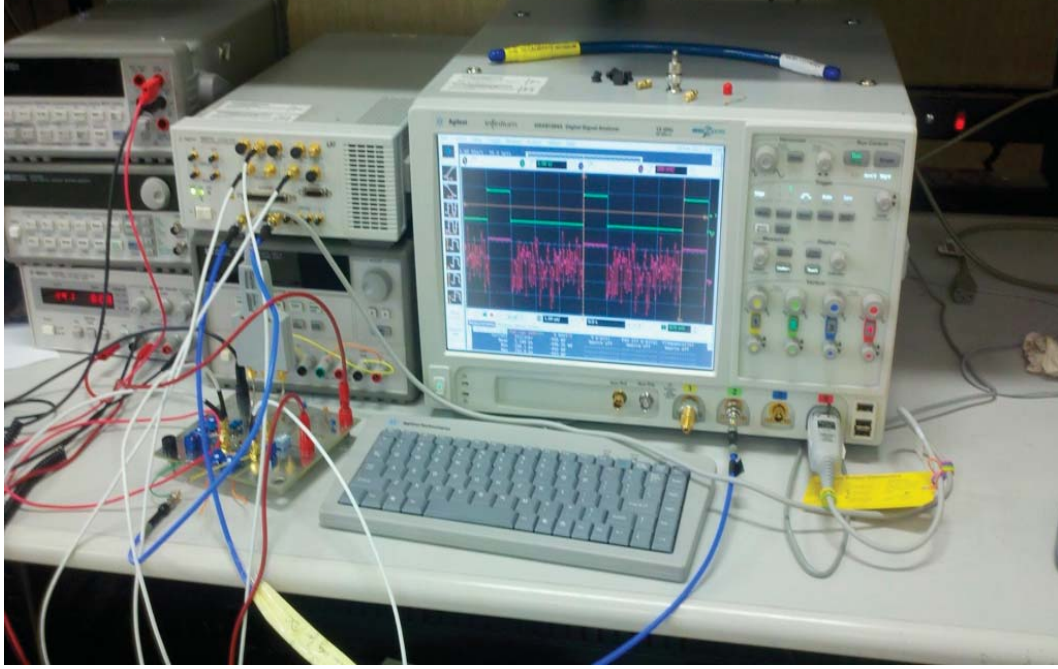


Fig. 52. Photo of the test bench.

formance of the system, where multi-carrier signals with a sparsity no more than 4% were generated by the Agilent N8241A Arbitrary Waveform Generator and sent to the evaluation board, the resulted compressed samples were collected and digitized at the DSA91304A Oscilloscope and sent to the host PC for reconstruction. The SNR of the reconstructed signal were calculated. Table IX summarizes the test results and the spectrum of the reconstructed signals are shown in Fig. 55 - Fig. 60.

Note that for test cases where the carriers have different initial phases, we can observe strong DC component in the reconstructed signal spectrum, this is due to the DC offset and can easily be canceled out. Also note that in the reconstructed signal spectrum, higher frequency carriers are with higher amplitude. This is because of the pre-distortion operation (applying an internal equalizer) inside the arbitrary waveform generator N8241A, which



Fig. 53. Example output of the tested chip.

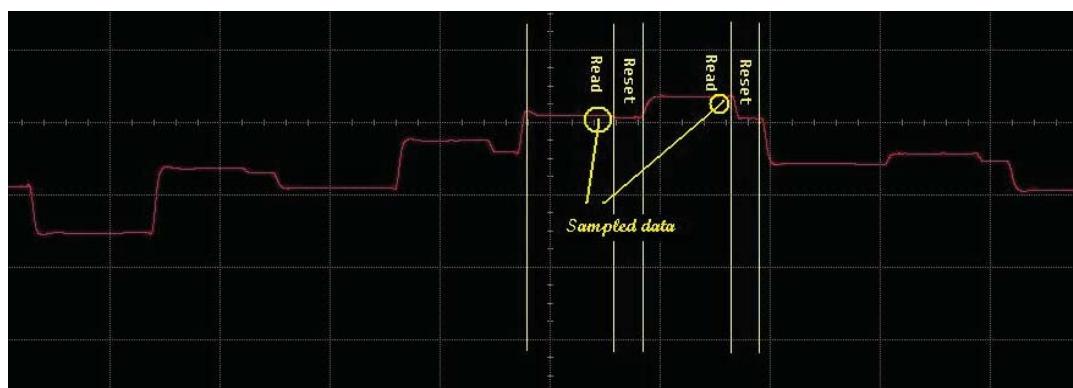


Fig. 54. Illustration of the reading and resetting phase.

Table VIII. System parameters for the test.

Input Signal Bandwidth (4% sparsity)	5 MHz ~ 500 MHz
Number of Parallel Paths	8
Single Path sampling rate	45 Ms/s
Overall System Sampling rate	360 MS/s
Fullscale input / output	-20 dBm / -2 dBm (referred to 50 ohms)

Table IX. Summary of the test results.

Input carrier frequencies (MHz)	Measured SNR (dB)
[+50, +150, +250, +490]*	29.42
[+20, +70, +450]	30.04
[+20, +70, +250, +450]	27.74
[+50, +250, -490]	24.35
[-20, -70, +250, +450]	24.53
[+50, -150, +250, -490]	23.58

provides higher gain on the higher frequency components. We get a rough estimation of the pre-distortion transfer function by observing the spectrum of the waveform generator N8241A output with a 10-tone signal, which is analyzed by the FFT function of the oscilloscope DSA91304A and shown in Fig. 61.

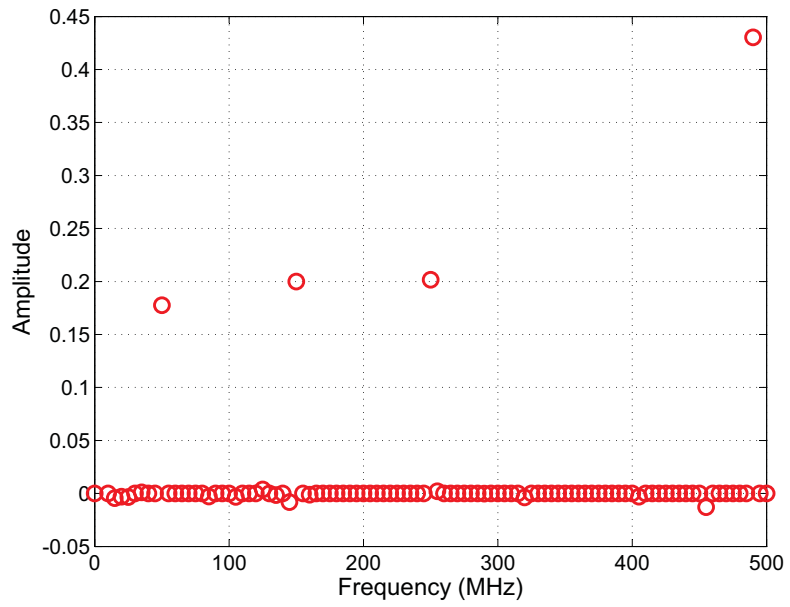


Fig. 55. Spectrum of the reconstructed signal ([+50, +150, +250, +490]MHz).

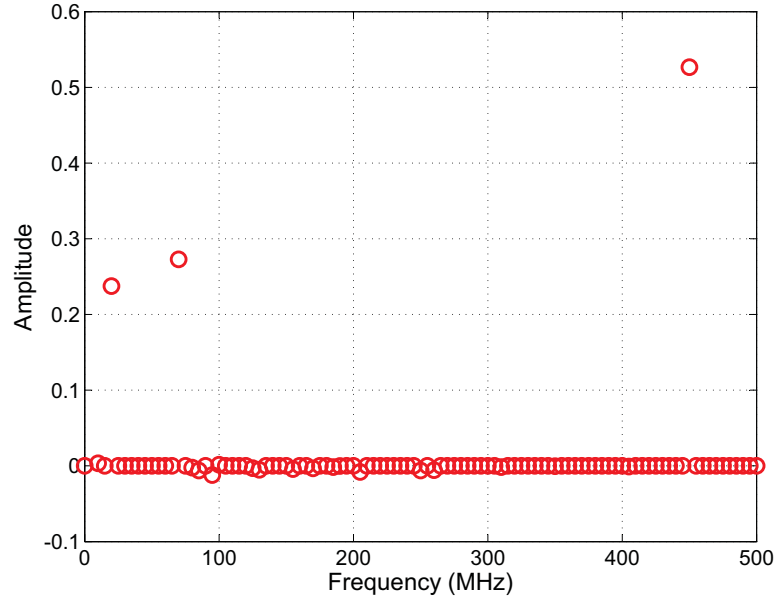


Fig. 56. Spectrum of the reconstructed signal ([+20, +70, +450]MHz).

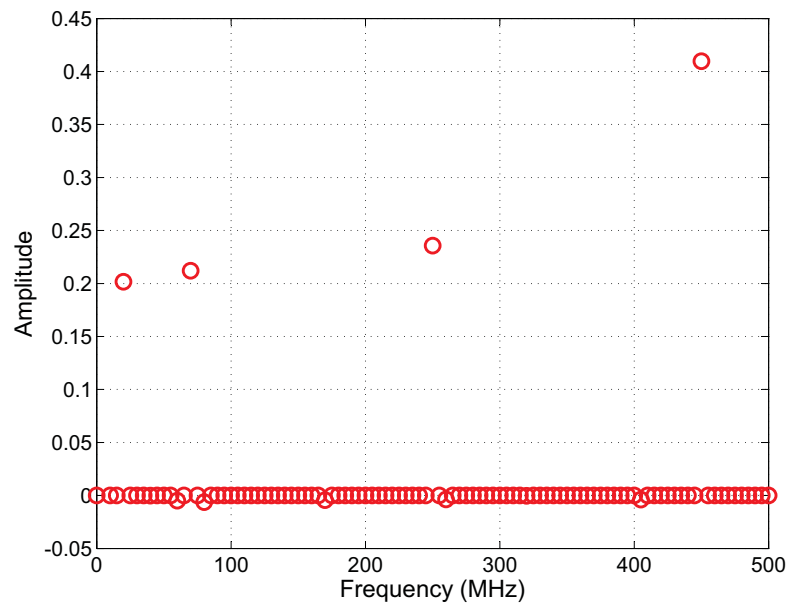


Fig. 57. Spectrum of the reconstructed signal ([+20, +70, +250, +450]MHz).

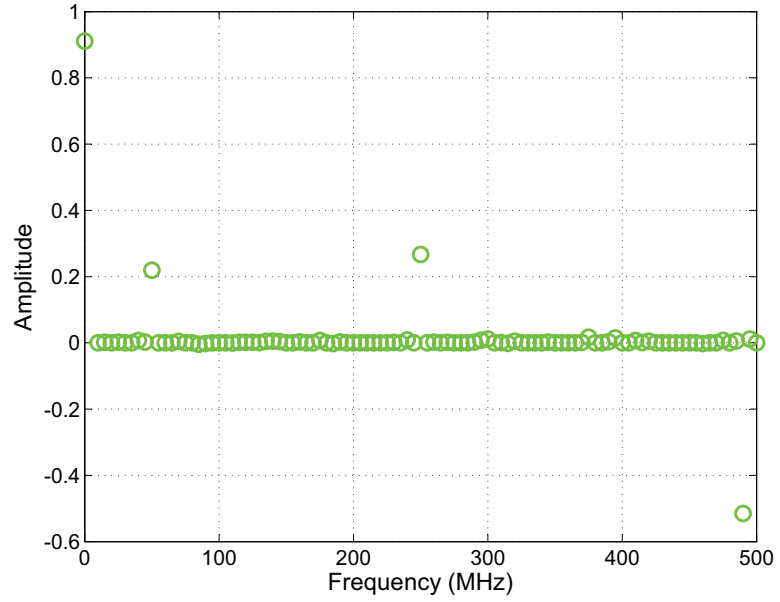


Fig. 58. Spectrum of the reconstructed signal ([+50, +250, -490]MHz).

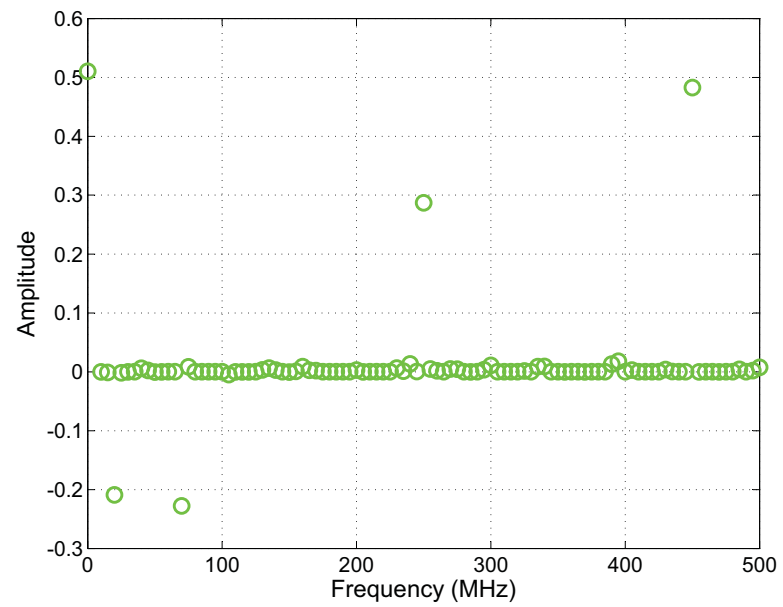


Fig. 59. Spectrum of the reconstructed signal ($[-20, -70, +250, +450]$ MHz).

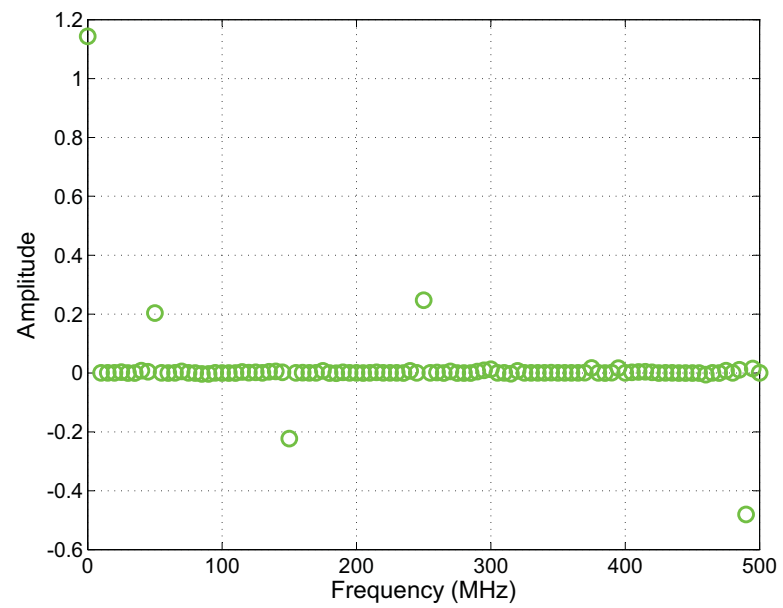


Fig. 60. Spectrum of the reconstructed signal ($[+50, -150, +250, -490]$ MHz).

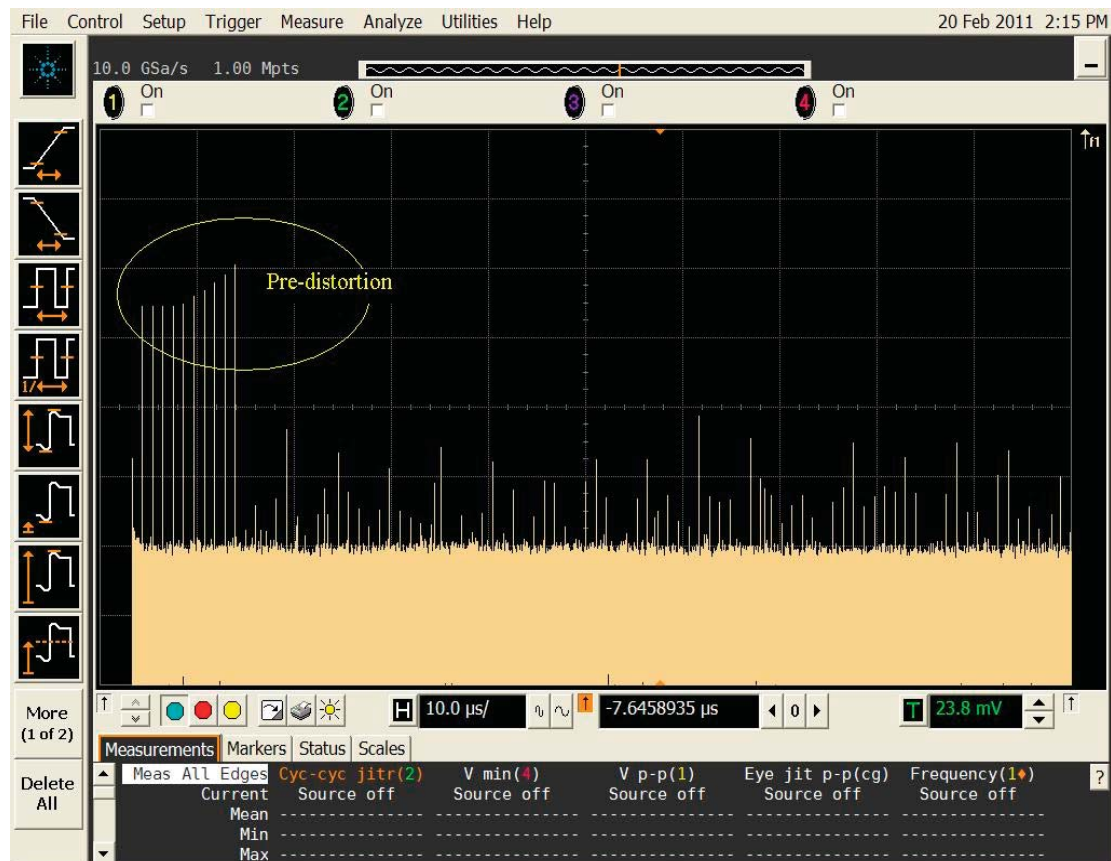


Fig. 61. Transfer function of the pre-distortion filter in the arbitrary waveform generator the N8241A.

CHAPTER VIII

APPLICATIONS ON SPECTRUM SENSING

The capability of sampling and reconstructing sparse signal at sub-Nyquist rate of mixed-signal compressive sensing motivates different applications in various fields, such as imaging [87], [88], [89], medical imaging [90], [91], communications [92], [93], [94], statistical signal processing [95], machine learning [96], geophysics [97], [98], error correction and decoding [99], [100], among which an important application is spectrum sensing or estimation of wideband frequency-domain sparse signals. In this chapter, we show how the mixed-signal PSCS system is applied on the spectrum sensing for cognitive radios and the spectrum analysis in RF tests.

A. Cognitive Radio

Cognitive radio holds the promise of relieving the scarcity of frequency resources by allowing dynamic spectrum sharing. In Cognitive Radios, spectrum holes that are unoccupied by primary users can be assigned to appropriate secondary users so that the spectrum is dynamically shared and the spectrum efficiency is enhanced [70], [73], [101], [102]. However, due to the wide frequency bandwidth, potentially up to several giga-hertz, spectrum sensing in CR can be a very challenging task. Fortunately, much of today's spectrum usage is such that only a small portion of frequency bands are heavily loaded while others are partially or rarely occupied [27]. This sparsity on spectrum usage makes it possible to apply CS to do the wideband spectrum sensing at sub-Nyquist rate. This idea of apply-

ing compressive sensing on the spectrum sensing of cognitive radios was first introduced in [69], however, that's a digital approach. Digital approaches generally require full-rate sampling before spectrum estimation, and the issue is then to reduce the complexity of the spectrum estimation. In [59], we first proposed the idea of using the mixed-signal PSCS front-end to do the spectrum sensing of cognitive radios. With this mixed-signal approach, the needs on the high-speed Nyquist-rate ADCs can be avoided.

The detection of the spectrum holes consists of several crucial steps: first, spectrum estimation; second, calculate the sufficient statistics, during which digital signal processing is needed to improve the front-end sensitivity by processing gain and identification of the primary users based on knowledge of the signal characteristics [70]; last, to decide whether there exist primary users based on the sufficient statistics. Among these steps, the first step is very challenging, since it involves the analog-to-digital conversion of wideband signals. The sub-Nyquist rate sampling capability of our mixed-signal PSCS front-end naturally fits this scenario. While doing spectrum sensing in cognitive radios, the wideband spectrum to be sensed can be represented with the multi-band model as shown in Fig. 7 and expressed mathematically with equation (3.3). Then, the mixed-signal PSCS front-end can be used to obtain compressed information about the sensed spectrum at sub-Nyquist rate, from which we can do spectrum estimation. Because of the nonuniform distribution of the signal power over the frequency band, two types of SNR can be defined: $SNR_{overall}$ and $SNR_{carrier}$, where $SNR_{overall}$ is the total signal power over the whole signal bandwidth divided by the total noise power over the whole signal bandwidth, and $SNR_{carrier}$ defined as the average SNR for one carrier. Because the noise is distributed uniformly

over the whole signal bandwidth but the active carriers only occupy a portion of the whole signal bandwidth, the relationship between $SNR_{overall}$ and $SNR_{carrier}$ is approximately $SNR_{overall} = SNR_{carrier} * \frac{K}{S}$.

We carried out a simulation to show the effectiveness of the mixed-signal PSCS front-end on the wideband spectrum sensing for cognitive radios, where the input signal is approximated as a frequency-domain sparse multi-carrier signals with $S = 128$, $K = 17$, and $SNR_{overall} = -10\text{dB}$. Note how noisy the received signal is in this example, Fig. 62. There are 5 primary bands with a band expansion up to 528MHz. Using $\Delta f = 4.125\text{MHz}$, the primary user's frequencies are $[17, 18, 43, 44, 45, 63, 64, 65, 66, 67, 76, 77, 118, 119, 120, 121, 122] \times 4.125 \text{ MHz}$. The input power dynamic range of the primary users is 15dB, and no prior knowledge is assumed available at the sensing radio. In Fig. 62 and Fig. 63, from top to bottom, the four plots represent the transmitted signal by the primary users, the received primary users' signal at the sensing radio, the reconstructed signal from the time-domain samples via the Nyquist rate ADC, and the reconstructed signal from the transform-domain samples via mixed-CS at a NSR of 0.32. The measured MSE for the two reconstructed signals is -5 dB and -14dB, respectively. Note that even with a lower sampling rate, the sensing radio based on mixed-signal PSCS is more robust against noise than the traditional digital approach based on the DFT, because CS takes advantage of the knowledge of the signal structure and its sparsity.

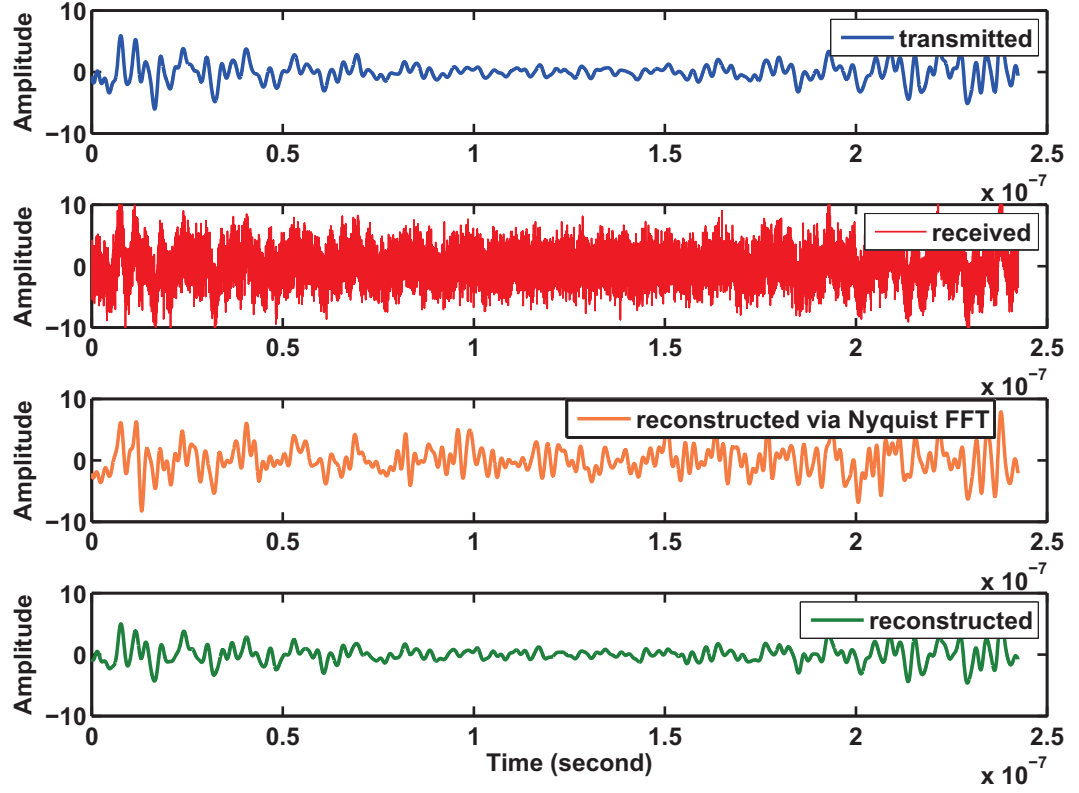


Fig. 62. Time-domain signals of a simulated multi-band signal. From top to bottom, the four plots represent the transmitted signal by primary users, the received primary users' signal at the sensing radio, the reconstructed signal from the time-domain samples via the Nyquist rate ADC and the reconstructed signal from the transform-domain samples via mixed-CS at a NSR of 0.32.

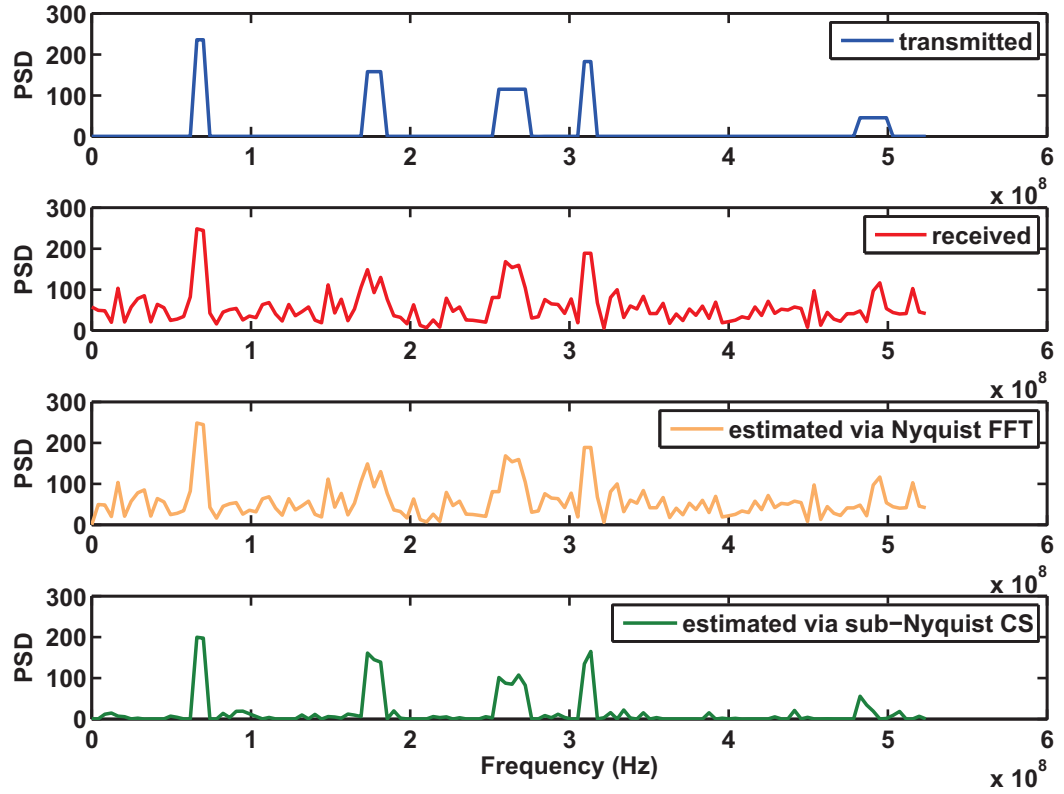


Fig. 63. Frequency-domain signals of a simulated multi-band signal. From top to bottom, the four plots represent the transmitted signal by primary users, the received primary users' signal at the sensing radio, the reconstructed signal from the time-domain samples via the Nyquist rate ADC and the reconstructed signal from the transform-domain samples via mixed-CS at a NSR of 0.32.

B. Spectrum Analysis and Circuit Testing

Spectrum analyzers are widely used in industry, research and education, including digital and analog technologies. Analog spectrum analyzers, also called swept spectrum analyzers, are typically based on the superheterodyne architecture, where the LO frequency is tuned by the VCO such that the desired frequency falls in the passband of the IF filter. In a digital spectrum analyzer the input analog signal is first sampled at Nyquist rate and then analyzed via a DFT. As a measurement instrument, the ADC in a spectrum analyzer needs to have a high resolution, which limits the maximum achievable sampling rate. The idea of parallel compressive sensing proposed in this paper can be useful to provide both high sampling rate and high resolution simultaneously when the input signal to the spectrum analyzer is sparse. For example, circuit linearity measurements are often carried out with a one or two-tone test (excite the RF component with one or two sinusoidal signals and observe the generated harmonics and intermodulation products). The resulting frequency span may be quite large, but the test signal and response are generally very sparse. Define NBW as the whole signal bandwidth to be analyzed, with the multi-tone model as given in equation (3.3), the whole signal bandwidth can be approximated with $S = NBW/\Delta f$ discrete tones, where Δf is the frequency resolution. Assuming that there are $K \ll S$ possible harmonic and intermodulation components within the NBW , obviously, this is a problem of wideband sensing of sparse signals, for which our proposed PSCS front-end can be utilized to achieve sub-Nyquist rate sensing. Recall that the minimum number of measurements needed for perfect signal reconstruction of a K -sparse vector with a dimensionality of S with convex optimization is on the order of $K \log(1 + S/K)$ [29], [30] and

define the Normalized Sparsity $NSP = K/S$, [75], we have

$$NSR = \frac{F_{CS}}{F_{Nq}} = c \cdot \frac{K \Delta f \log(1 + \frac{NBW}{K \Delta f})}{2NBW} = \frac{c}{2} \cdot NSP \log(1 + 1/NSP), \quad (8.1)$$

where, c is a scalar.

To provide a numerical example, suppose we would like to test the THD (Total Harmonic Distortion) of a digital TV (DTV) receiver. A single tone at 400MHz is applied and the output is sent to the spectrum analyzer. Consider observing the harmonic distortion up to the 5th order. Assuming that the mixed-signal PSCS front-end consists of 4 parallel paths each of which employs a sampling rate of 100MHz, the CS spectrum analyzer can function as follows:

Step 1: $f_l = 400\text{MHz}$, $f_h = 2000\text{MHz}$. Assuming that the signal is downconverted to baseband before Nyquist sampling, we find that $NBW = f_h - f_l = 1600\text{MHz}$ and $F_{Nq} = 3200\text{MHz}$.

Step 2: Because the designed mixed-signal PSCS front-end consists of 4 parallel paths at a sampling rate of 100MHz per path, the overall compressive sampling rate $F_{CS} = 400\text{MHz}$. Therefore, $NSR = \frac{F_{CS}}{F_{Nq}} = 0.125$.

Step 3: Assuming $c/2 = 2$ in the equation (3.3), which is conservative based on previous simulation results such as in Fig. 12, we can infer the required $NSP = 0.02$ from equation (8.1) since $NSR = 0.125$.

Step 4: With $K = 5$, $NSP = \frac{K}{S} = 0.025$, we get $S = 200$, which corresponds to a

frequency resolution of $\Delta f = \frac{NBW}{S} = 10MHz$.

Step 5: The DSP provides a spectral estimate by solving the CS reconstruction problem, where the signal is modeled as a frequency-domain sparse multi-carrier signal as given by equation (3.3), with $f_l = 400MHz$, and $\Delta f = 10MHz$. If direct modeling is used, $S = 200$; if compact modeling is used, S can be further reduced.

Fig. 64 shows the required NSR when we use the CS spectrum analyzer to do the above harmonic testing, where Δf is the frequency resolution in the signal modeling. With direct modeling, the signal basis includes carrier frequencies at $[400 : \Delta f : 2000]MHz$. Referring to the figure, we make two observations. First, with $\Delta f = 10MHz$, then $NSR < 0.125$, which meets the design specifications and means that the designed CS spectrum analyzer working at a compressive sampling rate of 400MHz can achieve harmonic spectrum analysis up to the 5th order which is located at 2 GHz. Second, because the testing tones are narrowband signal, the smaller the Δf , the lower the NSR . However, this requires a longer processing time $T = 1/\Delta f$ and high digital complexity because S gets larger.

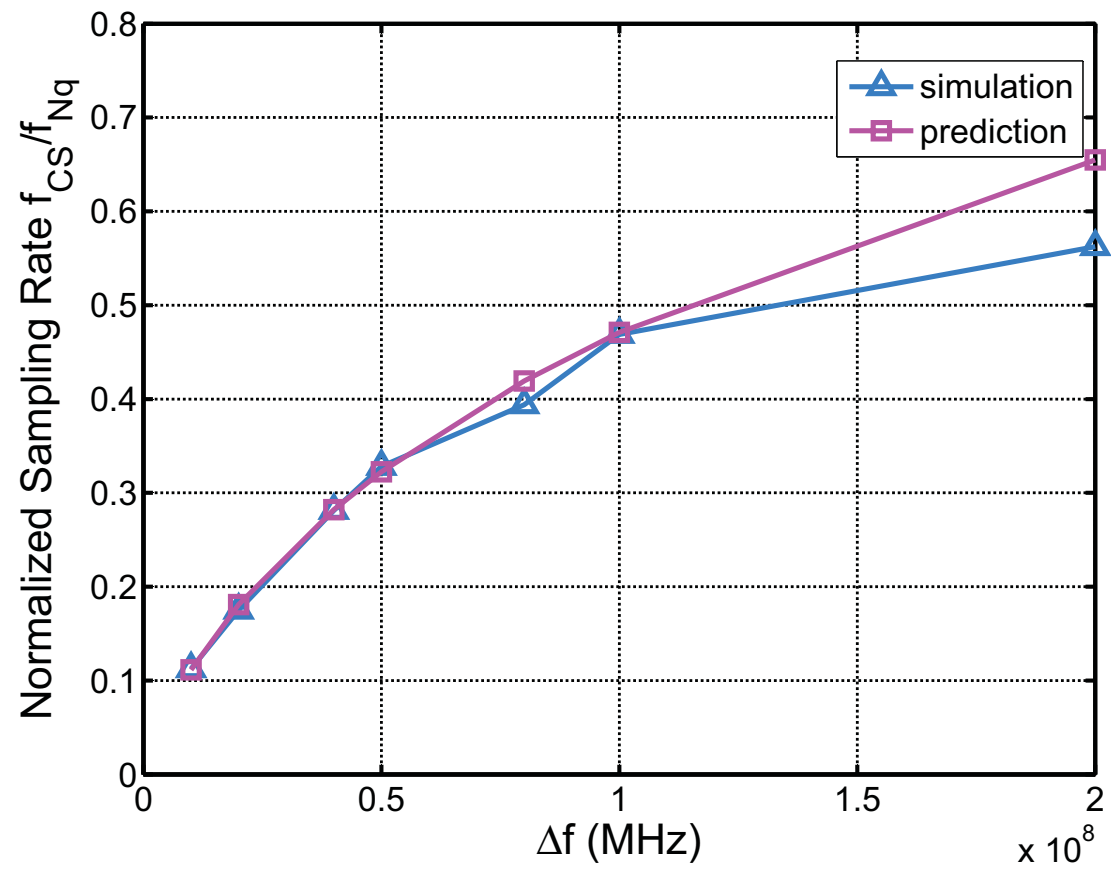


Fig. 64. Normalized sampling rate (NSR) vs Δf when using the CS spectrum analyzer to do the harmonic testing.

CHAPTER IX

CONCLUSIONS

Conventional radio architectures are severely stressed as bandwidths progress from hundreds of MHz to several GHz. However, there are many applications where the input signal shows some sparsity, and the proposed mixed-signal parallel compressive sensing architecture can then be used to reduce the sampling rate by exploiting the signal sparsity. The sub-Nyquist rate sampling is achieved through compressive sensing and parallelization. The mixed-signal CS avoids the necessity of a high-speed, high-resolution Nyquist rate ADC. The parallel structure brings flexibility and scalability in design, and practical wideband spectrum sensing can be realized by carefully balancing the complexity and the sampling rate. The overlapping windowed integration in the PSCS front-end provides a spurious frequency rejection scheme by setting the lowpass filter nulls on the spurious frequencies without sacrificing the sampling rate requirement.

In CS receivers, the input signal is randomized before going through sampling and reconstruction. Therefore, the ADC nonlinearity does not affect directly the original signal but the randomized signal. As a result, when processing frequency-domain sparse signals, the spurious energy due to the ADC nonlinearity spreads along the signal bandwidth rather than get concentrated on a few frequencies, which provides improvement on the ADC SFDR. Simulation results show that for sparsity signals with a sparsity of 2%, the CS receiver ADC SFDR improvement compared to a conventional Nyquist sampling architecture can be up to 14 dB.

The accuracy of analog circuit components is critical to the overall performance of the compressive systems, because the circuit imperfection such as the finite settling time, jitter, frequency offsets, gain and phase mismatches, will introduces an error on the reconstruction matrix if not treated properly. The proposed background calibration algorithms based on LMS are shown to be able to correct the error due to circuit nonidealities for the PSCS system effectively, which can be conveniently extended to other compressive sensing systems.

A low-speed prototype was built with off-the-shelf components, A high-speed integrated prototype was designed and fabricated with the IBM90nm CMOS technology. Both prototypes are able to sense sparse analog signals at sub-Nyquist rate and significantly reduce the power consumption. The high-frequency prototype also has a reconfigurable structure and can operate up to Nyquist rate and sample non-sparse signals as well.

The proposed RF frontend can be used for wideband spectrum sensing in cognitive radio thanks to the widely observed sparsity in frequency usage. Analysis and simulation show that the proposed architecture can process the analog signal with only 10%-40% of the Nyquist sampling rate depending on the sparsity of the input analog signal. The proposed scheme can also be used to expand the frequency range of digital spectrum analyzers while doing RF tests.

REFERENCES

- [1] *Wireless LAN Medium Access Control (MAC) and Physical Layer (PHY) Specifications Amendment 1: Enhancements for Higher Throughput*, IEEE Std. 802.11n, 2007.
- [2] *Wireless Medium Access control (MAC) and Physical Layer (PHY) Specifications for High Rate Wireless Personal Area Networks (WPANs)*, IEEE Std. 802.15.3, 2003.
- [3] R. B. Staszewski, K. Muhammad, D. Leipold, C. M. Hung, Y. C. Ho, J. L. Wallberg, C. Fern, K. Maggio, R. Staszewski, T. Jung, J. Koh, S. John, I. Y. Deng, V. Sarda, O. Moreira-Tamayo, V. Mayega, R. Katz, O. Friedman, O. E. Eliezer, E. De-Obaldia, and P. T. Balsara, "All-digital TX frequency synthesizer and discrete-time receiver for bluetooth radio in 130-nm CMOS," *IEEE J. Solid-State Circuits*, vol. 39, no. 12, pp. 2278–2291, Dec. 2004.
- [4] A. A. Abidi, "The path to the software-defined radio receiver," *IEEE J. Solid-State Circuits*, vol. 42, no. 5, pp. 954–966, May 2007.
- [5] J. Mitola III, "Cognitive radio: An integrated agent architecture for software defined radio," Ph.D. dissertation, Royal Institute of Technology (KTH), May 2000.
- [6] C. E. Shannon, "Communication in the presence of noise," *Proceedings of IRE*, vol. 37, pp. 10–21, Apr. 1949.
- [7] F. Maloberti, *Data Converters*. Dordrecht, The Netherlands: Springer, 2007.

- [8] S. Gupta, M. Choi, M. Inerfield, and J. Wang, "A 1GS/s 11b time-interleaved ADC in 0.13 μm CMOS," in *Digest of Technical Papers of IEEE Int. Solid State Circuit Conference (ISSCC)*, Feb. 2006, pp. 264–265.
- [9] M. V. S. M. Louwsma, A. J. M. van Tuijl and B. Nauta, "A 1.35GS/s, 10b, 175 mw time-interleaved AD converter in 0.13 μm CMOS," *IEEE J. Solid-State Circuits*, vol. 48, no. 4, pp. 778–786, Apr. 2008.
- [10] C.-C. Hsu, F.-C. Huang, C.-Y. Shih, C.-C. Huang, Y.-H. Lin, C.-C. Lee, B. Razavi, and H. Realtek, "An 11b 800MS/s time-interleaved ADC with digital background calibration," in *Digest of Technical Papers of IEEE Int. Solid State Circuit Conference (ISSCC)*, Feb. 2007, pp. 464–465.
- [11] Y. C. Lim, Y.-X. Zou, and J. W. L. and Shing Chow Chan, "Time-interleaved analog-to-digital-converter compensation using multichannel filters," *IEEE Trans. Circuits Syst. I*, vol. 56, no. 10, pp. 2234–2247, Oct. 2009.
- [12] D. Marelli, K. Mahata, and M. Fu, "Linear LMS compensation for timing mismatch in time-interleaved ADCs," *IEEE Trans. Circuits Syst. I*, vol. 56, no. 11, pp. 2476–2486, Nov. 2009.
- [13] A. Papoulis, "Generalized sampling expansion," *IEEE Trans. Circuits Syst. I*, vol. 24, no. 11, pp. 652–654, Nov. 1977.
- [14] S. R. Velazquez, T. Q. Nguyen, and S. R. Broadstone, "Design of hybrid filter banks for analog/digital conversion," *IEEE Trans. Signal Process.*, vol. 4, pp. 956–967,

Apr. 1998.

- [15] S. Mazlouman and S. Mirabbasi, "A frequency-translating hybrid architecture for wideband analog-to-digital converters," *IEEE Trans. Circuits Syst. II*, vol. 54, no. 7, pp. 576–580, Jul. 2007.
- [16] P. Lowenborg, H. Johansson, and L. Wanhammar, "Two-channel digital and hybrid analog digital multirate filter banks with very low-complexity analysis or synthesis filters," *IEEE Trans. Circuits Syst. II*, vol. 50, no. 7, pp. 355–367, Jul. 2003.
- [17] C. Lelandais-Perrault, T. Petrescu, D. Poulton, P. Duhamel, and J. Oksman, "Wide-band, bandpass, and versatile hybrid filter bank A/D conversion for software radio," *IEEE Trans. Circuits Syst. I*, vol. 56, no. 8, pp. 1772–1782, Aug. 2009.
- [18] P. Lowenborg, H. Johansson, and L. Wanhammar, "Quantization noise in filter bank analog-to-digital converters," in *Proc. of IEEE Int. Symp. Circuits Syst*, vol. 2, May 2001, pp. 601–604.
- [19] D. Asemani, J. Oksman, and P. Duhamel, "Subband architecture for hybrid filter bank A/D converters," *IEEE J. Sel. Topics Signal Process*, vol. 2, no. 2, pp. 191–201, Apr. 2008.
- [20] P. Lowenborg, H. Johansson, and L. Wanhammar, "Analysis of gain and timeskew errors in filter bank based A/D converters," in *Proc. of IEEE Midwest Symp. Circuits Syst*, Aug. 2001, pp. 263–266.

- [21] B. Murmann, “ADC performance survey 1997-2010,” Jun. 2010. [Online]. Available: <http://www.stanford.edu/~murmman/adcsurvey.html>
- [22] R. H. Walden, “Analog-to-digital converter survey and analysis,” *IEEE J. Sel. Areas Commun.*, vol. 17, pp. 535–550, Apr. 1999.
- [23] B. Murmann, “Limits on ADC power dissipation,” *Analog Circuit Design*, pp. 351–367, 2006.
- [24] M.-G. D. B. Huseyin Arslan, Zhi Ning Chen, *Ultra Wideband Wireless Communication*. Hoboken, NJ: John Wiley & Sons Inc., 2006.
- [25] G. Giannakis and L. Yang, *Ultra Wideband Wireless Communication*. Cambridge, United Kingdom: Cambridge University Press, 2008.
- [26] X. Shen, *Ultra-wideband Wireless Communications: Theory and Applications*, ser. IEEE J. Sel. Areas Commun. IEEE, 2006. [Online]. Available: <http://books.google.com/books?id=yqMJPwAACAAJ>
- [27] FCC, “Spectrum policy task force report,” ET Docket, Tech. Rep. 02-135, Nov. 2002.
- [28] S. Mallat, *A Wavelet Tour of Signal Processing*, 2nd ed. San Diego: Academic Press, 1993.
- [29] D. L. Donoho, “Compressed sensing,” *IEEE Trans. Inf. Theory*, vol. 52, no. 4, pp. 1289–1306, Apr. 2006.

- [30] E. J. Candès, J. Romberg, and T. Tao, “Robust uncertainty principles: Exact signal reconstruction from highly incomplete frequency information,” *IEEE Trans. Inf. Theory*, vol. 52, pp. 489–509, Feb. 2006.
- [31] E. J. Candès and M. B. Wakin, “An introduction to compressive sampling,” *IEEE Signal Process. Mag.*, vol. 25, no. 2, pp. 21–30, Mar. 2008.
- [32] E. J. Candès, “The restricted isometry property and its implications for compressed sensing,” *Compte Rendus Mathématique*, vol. 346, pp. 589–592, May 2008.
- [33] S. Mendelson, A. Pajor, and N. Tomczak-Jaegermann, “Uniform uncertainty principle for Bernoulli and subgaussian ensembles,” *Constructive Approximation*, vol. 28, no. 3, pp. 277–289, Feb. 2008.
- [34] S. G. Mallat and Z. Zhang, “Matching pursuits with time-frequency dictionaries,” *IEEE Trans. Signal Process.*, vol. 41, no. 12, pp. 3397 – 3415, Dec. 1993.
- [35] B. K. Natarajan, “Sparse approximate solutions to linear systems,” *SIAM Journal on Computing*, vol. 24, no. 2, pp. 227–234, Jul. 2006.
- [36] R. G. Baraniuk, V. Cevher, M. F. Duarte, and C. Hegde, “Model-based compressive sensing,” *IEEE Trans. Inf. Theory*, vol. 56, no. 4, pp. 1982–2001, 2010.
- [37] S. Boyd and L. Vandenberghe, *Convex Optimization*. Cambridge, United Kingdom: Cambridge University Press,, 2004.
- [38] S. S. Chen, D. L. Donoho, and M. A. Saunders, “Atomic decomposition by basis pursuit,” *SIAM Journal on Scientific Computing*, vol. 20, no. 1, pp. 33–61, Jul. 1998.

- [39] J. Haupt and R. Nowak, "Signal reconstruction from noisy random projections," *IEEE Trans. Inf. Theory*, vol. 52, pp. 4036–4048, Sep. 2006.
- [40] E. J. Candès and T. Tao, "The Dantzig selector: statistical estimation when p is much larger than n ," *Annals of Statistics*, vol. 35, pp. 2313–2351, Dec. 2007.
- [41] J. Tropp and A. C. Gilbert, "Signal recovery from partial information via orthogonal matching pursuit," *IEEE Trans. Inf. Theory*, vol. 53, pp. 4655–4666, Dec. 2007.
- [42] D. L. Donoho, Y. Tsaig, I. Drori, and J. L. Starck, "Sparse solution of underdetermined linear equations by stagewise orthogonal matching pursuit," Stanford University, Tech. Rep. 2006-02, 2006.
- [43] T. Blumensath and M. E. Davies, "Iterative hard thresholding for compressed sensing," *Applied and Computational Harmonic Analysis*, vol. 27, no. 3, pp. 265–274, Nov. 2009.
- [44] D. Needell and J. Tropp, "CoSaMP: Iterative signal recovery from incomplete and inaccurate samples," *Applied and Computational Harmonic Analysis*, vol. 26, no. 3, pp. 301–321, May 2009.
- [45] T. Blumensath and M. E. Davies, "Normalized iterative hard thresholding: guaranteed stability and performance," *IEEE J. Sel. Topics Signal Process.*, vol. 4, no. 2, pp. 298–309, Apr. 2010.
- [46] W. Dai and O. Milenkovic, "Subspace pursuit for compressive sensing signal reconstruction," *IEEE Trans. Inf. Theory*, vol. 55, no. 5, pp. 2230–2249.

- [47] M. Fornasier and H. Rauhut. (2011) Compressive sensing. [Online]. Available: <http://www.ricam.oeaw.ac.at/people/page/fornasier/CSFornasierRauhut.pdf>
- [48] E. J. Candès, “Compressive sampling,” in *Proc. of International Congress of Mathematicians*, vol. 3, 2006, pp. 1433–1452.
- [49] T. Ragheb, S. Kirolos, J. Laska, A. Gilbert, M. Strauss, R. Baraniuk, and Y. Massoud, “Implementation models for analog-to-information conversion via random sampling,” in *Proc. of Midwest Symposium on Circuits and Systems*, Aug. 2007, pp. 325–328.
- [50] J. Laska, S. Kirolos, Y. Massoud, R. Baraniuk, A. Gilbert, M. Iwen, and M. Strauss, “Random sampling for analog-to-information conversion of wideband signals,” in *Proc. of IEEE Dallas Circuits and Systems Workshop (DCAS)*, Oct. 2006, pp. 119–122.
- [51] J. Elbornsson, F. Gustafsson, and J.-E. Eklund, “Blind equalization of time errors in a time-interleaved ADC system,” *IEEE Trans. Signal Process.*, vol. 53, no. 4, pp. 1413–1424, 2005.
- [52] C. Herley and P. W. Wong, “Minimum rate sampling and reconstruction of signals with arbitrary frequency support,” *IEEE Trans. Inf. Theory*, vol. 45, no. 5, pp. 1555–1564, Jul. 1999.
- [53] R. Venkataramani and Y. Bresler, “Perfect reconstruction formulas and bounds on aliasing error in sub-Nyquist nonuniform sampling of multiband signals,” *IEEE*

Trans. Inf. Theory, vol. 46, no. 6, pp. 2173–2183, Sep. 2000.

- [54] M. Mishali and Y. C. Eldar, “Blind multi-band signal reconstruction: compressed sensing for analog signals,” *IEEE Trans. Signal Process.*, vol. 57, no. 3, pp. 993–1009, Mar. 2009.
- [55] Y. C. Eldar and A. V. Oppenheim, “Filter bank reconstruction of bandlimited signals from nonuniform and generalized samples,” *IEEE Trans. Signal Process.*, vol. 48, no. 10, pp. 2864–2875, Oct. 2000.
- [56] H. Johansson and P. Lowenborg, “Reconstruction of nonuniformly sampled bandlimited signals by means of digital fractional delay filters,” *IEEE Trans. Signal Process.*, vol. 50, no. 11, pp. 2757–2767, 2002.
- [57] J. N. Laska, S. Kirolos, M. F. Duarte, T. S. Ragheb, R. G. Baraniuk, and Y. Massoud, “Theory and implementation of an analog-to-information converter using random demodulation,” in *Proc. of IEEE Int. Symp. on Circuits and Systems (ISCAS)*, May 2007, pp. 1959–1962.
- [58] S. Kirolos, J. N. Laska, M. B. Wakin, M. F. Duarte, D. Baron, T. Ragheb, Y. Massoud, and R. G. Baraniuk, “Analog-to-information conversion via random demodulation,” in *Proc. of IEEE Dallas Circuits and Systems Workshop (DCAS)*, Oct. 2006, pp. 71–74.
- [59] Z. Yu, S. Hoyos, and B. M. Sadler, “Mixed-signal parallel compressed sensing and reception for cognitive radio,” in *Proc. of IEEE Int. Conf. on Acoustics, Speech and*

Signal Processing (ICASSP), Mar. 2008, pp. 3861–3864.

- [60] M. Mishali and Y. C. Eldar, “From theory to practice: Sub-Nyquist sampling of sparse wideband analog signals,” *IEEE J. Sel. Topics Signal Process.*, vol. 4, no. 2, pp. 375–391, Apr. 2010.
- [61] M. Mishali, Y. C. Eldar, and A. Elron, “Xampling. Part I: Practice,” Elect. Eng. Dept., Technion, CCIT, Tech. Rep. 747, Oct. 2009.
- [62] S. Hoyos and B. M. Sadler, “Ultra-wideband analog to digital conversion via signal expansion,” *IEEE Trans. Veh. Technol.*, vol. 54, no. 5, pp. 1609–1622, Sep. 2005.
- [63] S. Hoyos, B. M. Sadler, and G. R. Arce, “Broadband multicarrier communications receiver based on analog to digital conversion in the frequency domain,” *IEEE Trans. Wireless Commun.*, vol. 5, no. 3, pp. 652–661, Mar. 2006.
- [64] G. L. Fudge, R. E. Bland, M. A. Chivers, S. Ravindran, J. Haupt, and P. E. Pace, “A Nyquist folding analog-to-information receiver,” in *Proc. of the 42nd Asilomar Conf. on Signals, Systems and Computers*, Oct. 2008, pp. 541–545.
- [65] A. Kohlenberg, “Exact interpolation of band-limited functions,” *J. Appl. Phys.*, vol. 24, pp. 1432–1435, Dec. 1953.
- [66] Y.-P. Lin and P. P. Vaidyanathan, “Periodically nonuniform sampling of bandpass signals,” *IEEE Trans. Circuits Syst. II*, vol. 45, no. 3, pp. 340–351, Mar. 1998.
- [67] M. Mishali and Y. C. Eldar, “Blind multi-band signal reconstruction: Compressed

sensing for analog signals,” *IEEE Trans. Signal Process.*, vol. 57, no. 3, pp. 993–1009, Mar. 2009.

- [68] Y. C. Eldar, “Compressed sensing of analog signals in shift-invariant spaces,” *IEEE Trans. Signal Process.*, vol. 57, no. 8, pp. 2986–2997, Aug. 2009.
- [69] Z. Tian and G. B. Giannakis, “Compressed sensing for wideband cognitive radio,” in *Proc. of IEEE Int. Conf. on Acoustics, Speech and Signal Processing (ICASSP)*, vol. 4, Apr. 2007, pp. 1357–1360.
- [70] D. B. Cabric, “Cognitive radios: System design perspective,” Ph.D. dissertation, Univ. of California at Berkeley, Dec. 2007. [Online]. Available: <http://www.eecs.berkeley.edu/~danijela/DanijelaPhDthesis.pdf>
- [71] F. Digham, M. Alouini, and M. Simon, “On the energy detection of unknown signals over fading channels,” *IEEE Trans. Commun.*, vol. 55, no. 1, pp. 21–24, Jan. 2007.
- [72] D. Cabric, S. Mishra, and R. Brodersen, “Implementation issues in spectrum sensing for cognitive radios,” in *Proc. of the 38th Asilomar Conference on Signals, Systems and Computers*, Nov. 2004, pp. 772–776.
- [73] Q. Zhao and B. M. Sadler, “A survey of dynamic spectrum access,” *IEEE Signal Process. Mag.*, vol. 24, no. 3, pp. 79–89, 2007.
- [74] T. Blumensath and M. E. Davies, “Sampling theorems for signals from the union of finite-dimensional linear subspaces,” *IEEE Trans. Inf. Theory*, vol. 55, no. 4, pp. 1872–1882, Apr. 2009.

- [75] S. Sarvotham, D. Baron, and R. Baraniuk, “Compressed sensing reconstruction via belief propagation,” *Rice ECE Department Technical Report TREE 0601*, 2006.
- [76] J. G. Proakis and D. K. Manolakis, *Digital Signal Processing: Principles, Algorithms and Applications*, 3rd ed. Upper Saddle River, NJ: Prentice Hall, 1995.
- [77] B. Razavi, *RF Microelectronics*. Upper Saddle River, NJ: Prentice Hall, 1998.
- [78] T. H. Lee, *The Design of CMOS Radio-Frequency Integrated Circuits*, 2nd ed. Cambridge, United Kingdom: Cambridge University Press, 2004.
- [79] Z. Yu, X. Chen, S. Hoyos, B. M. Sadler, J. Gong, and C. Qian, “Mixed-signal parallel compressive spectrum sensing for cognitive radios,” *International Journal of Digital Multimedia Broadcasting*, vol. 2010, article ID 730509, 10 pages, Mar. 2010. doi:10.1155/2010/730509.
- [80] S. Haykin, *Adaptive Filter Theory*, 4th ed. Upper Saddle River, NJ: Prentice Hall, 2001.
- [81] R. L. Pickholtz, D. L. Schilling, and L. B. Milstein, “Theory of spread-spectrum communications—a tutorial,” *IEEE Trans. Commun.*, vol. 30, no. 5, pp. 855–884, May 1982.
- [82] J. Hu, N. Dolev, and B. Murmann, “A 9.4-bit, 50-MS/s, 1.44-mW pipelined ADC using dynamic source follower residue amplification,” *IEEE J. Solid-State Circuits*, vol. 44, no. 4, pp. 1057–1066, Apr. 2009.

- [83] Y. Chen, S. Tsukamoto, and T. Kuroda, "A 9b 100MS/s 1.46mW SAR ADC in 65nm CMOS," in *Proc. of IEEE Asian Solid-State Circuits Conference*, Nov. 2009, pp. 145–148.
- [84] T. Sundstrom, B. Murmann, and C. Svensson, "Power dissipation bounds for high-speed Nyquist analog-to-digital converters," *IEEE Trans. Circuits Syst. I*, vol. 56, no. 3, pp. 509–518, Mar. 2009.
- [85] X. Chen, Z. Yu, S. Hoyos, B. M. Sadler, and J. Silva-Martinez, "A sub-Nyquist rate sampling receiver exploiting compressive sensing," *IEEE Trans. Circuits Syst. I*, vol. 58, no. 3, pp. 507–520, Mar. 2011.
- [86] K. Deguchi, N. Suwa, M. Ito, T. Kumamoto, and T. Miki, "A 6-bit 3.5-GS/s 0.9-V 98-mW flash ADC in 90-nm CMOS," *IEEE J. Solid-State Circuits*, vol. 43, no. 10, pp. 2303–2310, Oct. 2008.
- [87] M. Duarte, M. Davenport, D. Takhar, J. Laska, T. Sun, K. Kelly, and R. Baraniuk, "Single-pixel imaging via compressive sampling," *IEEE Signal Process. Mag.*, vol. 25, no. 2, pp. 83–91, Mar. 2008.
- [88] J. Haupt and R. Nowak, "Compressive sampling vs conventional imaging," in *Proc. of Int. Conf. on Image Processing (ICIP)*, Oct. 2006, pp. 1269–1272.
- [89] P. Nagesh and B. Li, "Compressive imaging of color images," in *Proc. of IEEE Intl. Conf. on Acoustic, Speech and Signal Processing (ICASSP)*, Apr. 2009, pp. 1261–1264.

- [90] M. Lustig, D. Donoho, and J. M. Pauly, "Sparse mri: The application of compressed sensing for rapid mr imaging," *Magnetic Resonance in Medicine*, vol. 58, no. 6, pp. 1182–1195, Dec. 2007.
- [91] J. Trzasko, A. Manduca, and E. Borisch, "Highly undersampled magnetic resonance image reconstruction via homotopic ell-0-minimization," *IEEE Trans. Medical Imaging*, vol. 28, no. 1, pp. 106–121, Dec. 2009.
- [92] S. Cotter and B. Rao, "Sparse channel estimation via matching pursuit with application to equalization," *IEEE Trans. Commun.*, vol. 50, no. 3, pp. 374–377, Mar. 2002.
- [93] G. Taubock and F. Hlawatsch, "A compressed sensing technique for OFDM channel estimation in mobile environments: Exploiting channel sparsity for reducing pilots," in *Proc. of IEEE Int. Conf. on Acoustics, Speech, and Signal Processing (ICASSP)*, Apr. 2008, pp. 2885–2888.
- [94] A. Oka and L. Lampe, "Compressed sensing reception of bursty UWB impulse radio is robust to narrow-band interference," in *Proc. of IEEE Global Communications Conference (GLOBECOM)*, Nov. 2009, pp. 1–7.
- [95] M. D. adn Petros Boufounos, M. Wakin, and R. Baraniuk, "Signal processing with compressive measurements," *IEEE J. Sel. Topics Signal Process.*, vol. 4, no. 2, pp. 445–460, Apr. 2010.
- [96] J. Wright, A. Yang, A. Ganesh, S. Shastry, and Y. Ma, "Robust face recognition via

- sparse representation,” *IEEE Trans. on Pattern Analysis and Machine Intelligence*, vol. 31, no. 2, pp. 210–227, Feb. 2009.
- [97] B. Jafarpour, V. K. Goyal, W. T. Freeman, and D. B. McLaughlin, “Compressed history matching: Exploiting transform-domain sparsity for regularization of non-linear dynamic data integration problems,” *Mathematical Geosciences. Geophysics*, vol. 42, no. 1, pp. 1–27, Oct. 2009.
- [98] S. Hu, M. Lustig, A. P. Chen, J. Crane, A. Kerr, D. A. Kelley, R. Hurd, J. Kurhanewicz, S. J. Nelsona, J. M. Pauly, and D. B. Vigneron, “Compressed sensing for resolution enhancement of hyperpolarized ^{13}C flyback 3D-MRSI,” *Journal of Magnetic Resonance*, vol. 192, no. 2, pp. 258–264, Jun. 2008.
- [99] E. Candès and T. Tao, “Error correction via linear programming,” in *Proc. of 46th Annual IEEE Symposium on Foundations of Computer Science (FOCS)*, May 2005, pp. 668–681.
- [100] E. Candès and P. Randall, “Highly robust error correction by convex programming,” *IEEE Trans. on Information Theory*, vol. 54, no. 7, pp. 2829–2840, Jul. 2008.
- [101] I. F. Akyildiz, W. Lee, M. C. Vuran, and S. Mohanty, “NeXt generation/dynamic spectrum access/cognitive radio wireless networks: A survey,” *Computer Networks*, vol. 50, pp. 2127–2159, 2006.
- [102] S. Haykin, “Cognitive radio: Brain-empowered wireless communications,” *IEEE J. Sel. Areas Commun.*, vol. 23, no. 2, pp. 201–220, Feb. 2005.

VITA

Zhuizhuan Yu received her B.S. and M.S. degrees in electrical engineering from Beijing University of Posts and Telecommunications, China, in 2000 and 2003, respectively. From 2003 to 2005, she was a system engineer at Siemens Ltd. China. She started her doctoral program at Texas A&M University in Fall 2006 and received her Ph.D degree in May 2011. In the Summer and Fall of 2010, she was an intern at Texas Instrument, where she worked on the high-speed solutions for wireless transceivers. Zhuizhuan Yu can be reached through z-yu@ti.com.

The typist for this thesis was Zhuizhuan Yu.